

PROBING COSMOLOGICAL REIONIZATION
THROUGH
RADIO-INTERFEROMETRIC OBSERVATIONS
OF NEUTRAL HYDROGEN

*Thesis submitted to
Indian Institute of Technology, Kharagpur
for the award of the degree*

of
Doctor of Philosophy

by
Kanan Kumar Datta

under the guidance of
Dr. Somnath Bharadwaj



DEPARTMENT OF PHYSICS & METEOROLOGY
INDIAN INSTITUTE OF TECHNOLOGY, KHARAGPUR
MAY 2009

© 2009, Kanan Kumar Datta. All rights reserved.

CERTIFICATE OF APPROVAL

Date: 14/05/09

Certified that the thesis entitled **PROBING COSMOLOGICAL REIONIZATION THROUGH RADIO-INTERFEROMETRIC OBSERVATIONS OF NEUTRAL HYDROGEN** submitted by **KANAN KUMAR DATTA** to Indian Institute of Technology, Kharagpur, for the award of the degree of Doctor of Philosophy has been accepted by the external examiners and that the student has successfully defended the thesis in the viva-voce examination held today.

Signature

Signature

Signature

Name

Name

Name

(Member of the DSC)

(Member of the DSC)

(Member of the DSC)

Signature

Signature

Signature

Name

Name

Name

(Supervisor)

(External Examiner)

(Chairman)

DECLARATION

I certify that

- a. the work contained in this thesis is original and has been done by me under the guidance of my supervisor(s).
- b. the work has not been submitted to any other Institute for any degree or diploma.
- c. I have followed the guidelines provided by the Institute in preparing the thesis.
- d. I have conformed to the norms and guidelines given in the Ethical Code of Conduct of the Institute.
- e. whenever I have used materials (data, theoretical analysis, figures, and text) from other sources, I have given due credit to them by citing them in the text of the thesis and giving their details in the references. Further, I have taken permission from the copyright owners of the sources, whenever necessary.

Signature of the Student

CERTIFICATE

This is to certify that the thesis entitled **Probing Cosmological Reionization through Radio-Interferometric Observations of Neutral Hydrogen**, submitted by **Kanan Kumar Datta** to Indian Institute of Technology, Kharagpur, is a record of bona fide research work under my supervision and is worthy of consideration for the award of the degree of Doctor of Philosophy of the Institute.

Date:

Supervisor

Acknowledgment

This thesis is the end of my long journey in obtaining my PhD degree. There are many people who made this journey easier with their proper guidance, words of encouragement, generous help. It is a pleasant aspect that I have now the opportunity to convey my gratitude to all of them.

First I bow down before the Almighty who has made everything possible. I express my heart-felt gratitude to my parents and other family members (uncle, aunty, sisters and brothers), for their love, support and encouragement. I dedicate my thesis to them. Special thanks to Rituparna Ghosal for her constant inspiration and support. She never let me down.

It is great pleasure and proud privilege to express my sincere thanks and gratitude to my supervisor, Prof. S. Bharadwaj, for all the guidance and encouragement he has offered me throughout the period of this research. I feel that I have been extremely lucky to get an adviser like him. I am grateful to him for his numerous ideas, suggestions, criticism of my research work. His style of thinking and his scientific interests has always been a source of inspiration for me. He always had enough patience to clarify all my various stupid doubts. Working with him has been sheer joy and I hope to do more fruitful work with him in future. I honestly thank God that He gave you as my adviser.

It is a pleasure to pay tribute also to my collaborators. I gratefully acknowledge Dr. Tirthankar Roychoudhury for his crucial contribution, advice, and supervision. He was always there when I needed him. I would also acknowledge Suman Majumdar who generated HI 21-cm maps. I am grateful for Tapomoy Guha Sarkar from whom I learned a lot. It was a pleasure to work with them. I hope to keep up our collaboration in the future.

I express my deep respectful thanks to Prof. S. Kar. I was taught relativity course by him. I learnt many things from his excellent teaching. He also has read the synopsis of my thesis and provided me valuable comments. I wish to thank Dr. S. Konar for her teaching on “Introduction to Astrophysics” course during my course work. I would like to thank Prof. A. Dasgupta, Prof. A. Taraphdar, Prof. S. P. Khastgir for useful discussion. It was nice experience to discuss scientific problems with them.

My friends at the Centre for Theoretical studies (CTS) gave me the feeling of being at home at work. I would like to thank Prasun Dutta, Dr Saiyad Ali, Prakash Sarkar, Abhik Ghosh, Dr Biswajit Pandey for scientific discussions that helped me a lot in staying at the right track. I would like to thank Anupam Das, Sanjit Das, Suman Ghosh, Partha Dutta, Soma Dey, Biswambhar Raksit, Dr Hemwati Nandan, Somnath Maity, Subhasis Panda, Tatan Ghosh with whom I share many exciting memorable moments of laughter and pure joy. I wish to thank Ujal Halder, Gopal, Subhabrata, Venu for helping me various ways.

I am also grateful to all the staff members of our department and Centre for Theoretical Studies and the authorities of Indian Institute of Technology (IIT), Kharagpur, with whom I had to interact many times during my period of work. I would like to thank the CSIR, Govt. of India for financial support through a Research Fellowship. Finally I would like to acknowledge the anonymous referee of the thesis for useful comments and suggestions which have certainly improved the quality of the thesis.

List of Symbols

Symbols	Definition (unit)
A	Amplitude for foreground power spectrum (mK^2)
A_{eff}	Effective antenna collecting area (m^2)
$A(\vec{\theta})$	Antenna beam pattern (unit less)
a_{lm}	Spherical Harmonics coefficient
B	Frequency bandwidth (MHz)
b_c	bias of the ionized sphere centers with the dark matter (unit less)
$C_l(\Delta\nu)$	Multifrequency angular power spectrum (mK^2)
$C_l^{flat}(\Delta\nu)$	$C_l(\Delta\nu)$ calculated using the flat sky (mK^2) approximation
$D(z)$	Growth rate of dark matter density contrast δ (unit less)
\vec{d}	Antenna separation vector projected in the plane perpendicular to the line of sight (m)
$(dB/dT)_\nu$	Conversion factor from temperature to specific intensity (mJy/mK)
\hat{E}	Estimator for bubble detection (mJy^2)
E_o	Observed value of the estimator (mJy^2)

Symbols	Definition (unit)
$F_l(\Delta\nu)$	Ratio of decrements of the 21-cm signal to the foreground (unit less)
$F(\vec{U}, \nu)$	Total foreground contribution (mJy)
$HF(\vec{U}, \nu)$	Contribution from fluctuating HI (mJy)
H_0	Hubble parameter at present (Km/s/Mpc)
$H(z)$	Hubble parameter at redshift z (Km/s/Mpc)
h	$H_0/100$ km/s/Mpc (unit less)
$I_l(\Delta\nu)$	Foreground frequency decorrelation function (unit less)
\bar{I}_ν	Average specific intensity of the redshifted HI 21-cm from the EoR (mJy)
$I_\nu(\vec{\theta})$	Sky specific intensity pattern at position $\vec{\theta}$ (Jy)
$J_1(x)$	First order Bessel function
j_l	Spherical Bessel function
j_l''	$\frac{d^2}{dx^2} j_l(x)$
\mathbf{k}	Fourier mode (Mpc^{-1})
\hat{k}	Unit vector of \mathbf{k}
k_B	Boltzmann constant (Joule/K)
k_{\parallel}	Component of \mathbf{k} along θ (Mpc^{-1})
ℓ	Angular mutipole (unit less)
\mathbf{m}	Component of \hat{n} along θ
N	Total number of antennae of a radio experiment
N_b	Total number of independent baselines

Symbols	Definition (unit)
$N(\vec{U}, \nu)$	System noise (mJy)
n	Power law index describes scaling relation of SNR with redshift
\hat{n}	Unit vector along line of sight
\tilde{n}_{HI}	Mean comoving number density of ionized spheres (Mpc^{-3})
n_s	spectral index in the matter power spectrum
$P_{HI}(k)$	HI 21-cm power spectrum in redshift space (Mpc^{-3})
$P_{\Delta_{HI}}(z, k)$	Cross-correlation power spectrum between the above two (Mpc^{-3})
$P_{\Delta_{HI}^2}(z, k)$	HI density power spectrum (Mpc^{-3})
$P(z, k)$	Dark matter power spectrum (Mpc^{-3})
R	Comoving radius of the ionized sphere (Mpc, in the Chapter 2 only)
\mathcal{R}	$\bar{x}_{HII}/\bar{x}_{HI}$ (unit less)
R_b	Comoving radius of ionized bubble (Mpc)
R_f	Comoving filter size (Mpc)
R_ν	Comoving radius of the planar section the bubble at a frequency ν (Mpc)
r_ν	Comoving distance from present to the redshift $z = 1420/\nu - 1$ (Mpc)
r'_ν	$dr_\nu/d\nu$ (Mpc/MHz)
$S_{center}(\vec{U}, \nu)$	HI signal from ionized bubble when it is at the center of FoV (mJy)

Symbols	Definition (unit)
S_{cut}	A flux level in the image above which all points sources can be identified and removed (mJy)
$S_f(\vec{U}, \nu)$	Filter to detect individual ionized bubbles (mJy)
$S(\vec{U}, \nu)$	HI signal from ionized bubble (mJy)
t_{obs}	Total observation time (sec)
T_s	Spin temperature of hydrogen gas (mK)
T_{sky}	Sky brightness temperature (Kelvin)
T_γ	CMB temperature (K)
$T(\nu, \hat{n})$	Excess 21-cm brightness temperature observed at a frequency ν along a direction \hat{n} (mK)
$\bar{T}(z)$	Spatially averaged Excess 21-cm brightness temperature at redshift z (mK)
\vec{U}	Baseline vector (unit less)
u, v	Two components of \vec{U} (unit less)
$V(\vec{U}, \nu)$	Total Visibility measured at baseline \vec{U} and frequency ν (Jy)
$v(z, \hat{r}_\nu)$	peculiar velocity of HI gas (km/sec)
$W(y)$	Spherical top hat window function
x_{HI}	Neutral hydrogen fraction (unit less)
\bar{x}_{HII}	Average ionized hydrogen fraction (unit less)

Symbols	Definition (unit)
$\bar{x}_{HI}(z)$	Spatially averaged HI fraction (unit less)
Y	Helium mass fraction (unit less)
Y_{lm}	Spherical Harmonics
z	Redshift (unit less)
z_c	Redshift of ionized bubble center (unit less)
$\bar{\alpha}$	Mean spectral index (unit less)
α_{eff}	Effective spectral index (unit less)
β	power law index for foreground power spectrum (unit less)
$\Delta_{HI}(z, \mathbf{k})$	3D Fourier transform of the fluctuations in the HI densities (Mpc^{-3})
Δ_p	Poisson fluctuations (Mpc^{-3})
Δt	Integration time for a radio experiments (sec)
$\Delta\nu$	Frequency separation between two channels ν_1 and ν_2 (MHz, for chapter 2) $\nu_c - \nu$ (for other chapters)
$\Delta\nu_b$	Bubble size in frequency (MHz)
$\Delta\nu_c$	Frequency channel width (MHz)
$\Delta\nu_{1/2}$	Frequency separation $\Delta\nu$ at which the frequency decorrelation function $\kappa_l(\Delta\nu)$ becomes 1/2 (MHz)
$\Delta(z, \mathbf{k})$	3D Fourier transform of the fluctuations in the dark matter densities (Mpc^{-3})

Symbols	Definition (unit)
$\langle(\Delta E)^2\rangle$	Variance of the estimator (mJy^2)
$\langle(\Delta E)^2\rangle_i$	Contribution to the variance $\langle(\Delta E)^2\rangle$ from i^{th} component (mJy^2)
δ	Dark matter density contrast (unit less)
$\delta_D^2(\vec{U})$	Two dimensional Dirac delta function
$\delta_{HI}(z, \hat{n}r_\nu)$	Fluctuations in HI density field (unit less)
δ_{ij}	Kronekar delta
$\eta_{HI}(z, \hat{n}r_\nu)$	21-cm radiation efficiency in redshift space (unit less)
$\bar{\eta}_{HI}(\mathbf{k})$	Fourier transform of $\eta_{HI}(\hat{n}r_\nu)$ (Mpc^{-3})
$\Theta(x)$	Heaviside step function
θ	Two dimensional vector in the sky plane (unit less)
$\vec{\theta}_c$	Ionized bubble center (rad)
θ_x, θ_y	Two perpendicular components of θ (rad)
θ_ν	Angular radius of circular disk of radius R_ν (rad)
θ_{ν_c}	Angular size of ionized bubble (rad)
θ_0	$0.6\theta_{FWHM}$ (FWHM of the antenna beam pattern)
$\kappa_l(\Delta\nu)$	Dimensionless frequency decorrelation function (unit less)
λ	Observing wavelength (m)

Symbols	Definition (unit)
λ_c	Wavelength corresponding to frequency ν_c (m)
λ_J	Comoving Jeans Length (Mpc)
μ	Angle between the line of sight and the wave vector ($\hat{k} \cdot \hat{n}$)
ν_c	Redshifted frequency corresponding to the redshift z_c (MHz)
ν_f	Filter position along frequency axis (MHz)
ξ	Foreground frequency decorrelation length (MHz)
$\rho_N(\vec{U}, \nu)$	Normalized baseline distribution function(MHz ⁻¹)
$\rho_{ante}(r)$	Antenna distribution function
σ	Noise rms in image (mJy)
σ_p	One dimensional pair velocity dispersion in relative galaxy velocity (km/s)
σ_8	RMS mass fluctuations on $8h^{-1}$ Mpc scale (unit less)
τ_e	CMB electron scattering optical depth (unit less)
Ω	Solid angle (rad^2)
Ω_b	Baryon density parameter (unit less)
Ω_m	Matter density parameter (unit less)
$\langle .. \rangle$	Ensemble average

List of Tables

3.1	Parameters values used for characterizing different foreground contributions	53
-----	--	----

List of Tables

List of Figures

2.1	The shows the HI power spectrum $P_{\text{HI}}(\mathbf{k})$ for the different models of the HI distribution considered here. Other than the one labeled DM, the curves are all for the PR model with different values of R and b_c as indicated in the figure. Here the μ dependence has been incorporated by using the average value $\langle \mu^2 \rangle = 1/3$	26
2.2	The angular power spectrum of HI brightness temperature fluctuations for different models of the HI distribution assuming $b_c = 1$ and $\sigma_p = 0$	29
2.3	The frequency decorrelation function $\kappa_l(\Delta\nu)$ [defined in equation (2.13)] at $l = 10^2, 10^3, 10^4, 10^5$. Results are shown for the DM model and the PR model with $b_c = 1$ and the R values shown in the figure. For the DM model, we show results incorporating the FoG effect using $\sigma_P = 20$ and 40 km/s. For each l value $\kappa_l(\Delta\nu)$ decreases faster for $\sigma_P = 0$ and slowest for $\sigma_P = 40$ km/s. There is a significant change due to the FoG effect only at $l \geq 10^4$	31
2.4	This shows the b_c dependence of the frequency decorrelation function $\kappa_l(\Delta\nu)$ for the PR model with $R = 2$ Mpc.	33

List of Figures

2.5	This shows $\Delta\nu_{1/2}$ vs. l for the DM model and the PR model with $b_c = 1$ for the R values shown in the figure.	34
2.6	Angular power spectrum $C_l(0)$ at $\nu = 129$ MHz for the two most dominant foreground components, the diffuse galactic synchrotron radiation (GS) and the extragalactic point sources (PS) assuming $S_{cut} = 0.1$ mJy. The expected signal is also shown for the DM model and the PR model with $R = 16$ Mpc.	36
2.7	This shows $F_l(\Delta\nu)$ (defined in equation 2.34) for the $\Delta\nu$ values shown in the figure. We consider both the DM model(left panel) and the PR model(right panel).	38
3.1	Signal from a spherical ionized bubble of comoving radius 10 Mpc as a function of baseline U for different frequency channels.	46
3.2	Signal from a spherical ionized bubble of comoving radius 10 Mpc as a function of $\Delta\nu = \nu - \nu_c$ for different baselines.	47
3.3	The magnitude of the different contributions to the visibility $V(\vec{U}, \nu)$ at $\nu = 153$ MHz as a function of U . The signal, foregrounds (FG), noise (NS) and HI fluctuations (HF) contributions are shown for the GMRT (left) and MWA (right). The expected signal is shown for bubbles with radius $R = 10$ Mpc and $R = 50$ Mpc. The noise is estimated for a single baseline assuming an observation time $t_{obs} = 100$ hrs and channel width $\Delta\nu_c = 50$ KHz.	54
3.4	This shows the baseline coverage for 14 hrs of GMRT 153 MHz observation at 45° declination.	58

3.5	This shows the normalized baseline distribution $\rho_N(U, \nu)$ for the GMRT and the MWA at 153 MHz. The wiggly curve shows the actual values for the GMRT observation shown in Figure 3.4 and the smooth curve is the analytic fit.	59
3.6	The signal quantified through the expectation value of the estimator $\langle \hat{E} \rangle$ for Filter I. The other components (NS - Noise, FG - Foregrounds, HF - HI Fluctuations) are quantified through their contribution to the 3-sigma fluctuation $3 \times \sqrt{\langle (\Delta \hat{E})^2 \rangle}$	64
3.7	Same as Figure 3.6 except that Filter II is used instead of Filter I.	65
3.8	The observing time t_{obs} that would be required for a 3σ detection of a bubble of radius R_b provided it is at the center of the field of view. The vertical lines shows the lower limit (due to HI fluctuations) where a detection will be possible ($R_b = 8$ Mpc for GMRT and $R_b = 16$ Mpc for MWA).	67
3.9	The Overlap between the signal and the filter when there is a mismatch $\Delta\theta$ between the centers of the bubble and the filter for GMRT (left) and MWA (right). The results are shown for different bubble sizes.	68
3.10	Same as the Figure 3.8 considering three different antenna distributions $\rho_{ant}(r) \propto 1/r, 1/r^2, 1/r^3$ for the MWA.	69

List of Figures

- 4.1 This shows HI images on slices through the center of the bubble for the four different scenarios SB, PR1, PR2 and SM (from left to right). In first three panels the central, circular dark region of radius $R_b = 20$ Mpc shows the HII bubble that we are trying to detect. The HI outside this bubble traces the dark matter distribution. In the SB scenario(left) the hydrogen neutral fraction is $x_{\text{HI}} = 1$ outside the bubble. In the PR1 scenario (2nd from left) the extra bubbles are all of a fixed comoving radius 6 Mpc. In the PR2 scenario (3rd from left) the extra bubbles have the same comoving radius as the bubble that we are trying to detect. In both the PR1 and PR2 reionization scenarios the centers of the extra bubbles trace the dark matter distribution and $x_{\text{HI}} = 0.62$. In the SM scenario (right) the central region up to radius 27 Mpc is fully ionized (marked with solid circle) and beyond that region up to radius 42 Mpc the region is partially filled with HI patches (dashed circle). The mean neutral fraction is $x_{\text{HI}} = 0.5$. These simulations are all for the GMRT. 78
- 4.2 This shows the visibility signal (real part) from a frequency slice through the center of a spherical ionized bubble of comoving radius 20 Mpc embedded in HI. The solid curves show the expected signal assuming that the bubble is embedded in uniformly distributed HI. The data points show the visibilities for a few randomly chosen baselines from our simulation of the SB scenario. The difference between the data points and the solid curve is due to the fluctuations in the HI outside the bubble. Each panel corresponds to a different realization of the simulation. 81
- 4.3 Same as the previous figure except that U is fixed at 110 while the frequency varies, and $\Delta\nu = \nu - \nu_c$ 82

4.4	The estimator \hat{E} (defined in equation 4.4) for bubble size R_b ranging from 4 Mpc to 50 Mpc for the GMRT in the SB scenario. It is assumed that the filter is exactly matched to the bubble. The left panel shows the analytic predictions for the mean estimator $\langle \hat{E} \rangle$ and the $3 - \sigma$ error-bars due to the HI fluctuations. The solid and the dashed lines in the right panel respectively show the $\langle \hat{E} \rangle$ and the $3 - \sigma$ envelope determined from the simulations. The data points in the right panel show \hat{E} in the individual realizations.	87
4.5	Same as the Figure 4.4 for the MWA.	87
4.6	The $\text{SNR} = \langle \hat{E} \rangle / \sqrt{\langle (\Delta \hat{E})^2 \rangle_{\text{NS}}}$ for 1000 hrs observation with the GMRT as a function of the filter size R_f for the case where the actual bubble size is $R_b = 10$ Mpc . The left panel shows 4 different realizations of the simulation. The right panel shows the mean SNR and $3 - \sigma$ error-bars calculated using 24 realizations. The solid line shows the analytical predictions.	91
4.7	Same as the Figure 4.6 for $R_b = 20$ Mpc for the GMRT.	93
4.8	Same as the Figure 4.6 for $R_b = 20$ Mpc for the MWA.	94
4.9	The SNR for 1000 hrs GMRT observations for a bubble of size $R_b = 10$ Mpc located at the center of the field of view. The filter scans along $\theta_x, \theta_Y, \nu_f$ (top, middle, bottom) to determine the bubble's position. The left panel shows results for 4 realizations of the SB simulation, the right panels show the mean (dashed curve) and $3 - \sigma$ error-bars determined from 24 realizations of the simulation and the analytic prediction for the mean (solid curve).	95
4.10	Same as the Figure 4.9 for $R_b = 20$ Mpc for the GMRT.	97
4.11	Same as the Figure 4.9 for $R_b = 20$ Mpc for the MWA.	98

List of Figures

4.12 The mean $\langle \hat{E} \rangle$ and $3-\sigma$ error-bars of the estimator as a function of R_f for the GMRT estimated from 24 different realizations of the PR1 scenario. In all cases the filter is exactly matched to the bubble. 99

4.13 Same as the Figure 4.12 for the MWA. 100

4.14 Same as Figure 4.6 for the SM scenario for the GMRT. The dotted, dashed dotted and dashed lines show results for three different realizations. To show the effect of non-sphericity, we compare these results with predictions for a spherical bubble of sized $R_b = 42$ Mpc embedded in uniform HI with neutral fraction $x_{\text{HI}} = 0.5$ (solid line). The vertical line at $R_f = 28$ Mpc shows the radius up to which the bubble is fully ionized and the SNR follows the spherical predictions. The SNR peaks at $R_f = 42$ Mpc marked by another vertical line. 101

4.15 Same as Figure 4.9 for the SM scenario for the GMRT. The x-axis shows the comoving distance of the filter position from the center of the box. The three curves respectively show results for a search along three θ_x , θ_y and ν axes. 103

5.1 This shows the evolution of the mean neutral fraction x_{HI} with redshift for the two different reionization models discussed in the text. 117

5.2 This shows the SNR contours for 1000 hrs observations with the GMRT. The left panel shows results for a constant neutral fraction $x_{\text{HI}} = 1$. Middle and right panel show results for the Model I and the Model II respectively. The HI fluctuations dominate over the signal in the shaded region and bubble detection is not possible. 119

5.3 Same as the figure 5.2 for the MWA. 119

5.4	This shows the SNR contours for a fixed value of bubble size with the GMRT. Left panel shows results for a $R_b = 20$ Mpc bubble and 4000 hrs of observations. Right panel shows results for $R_b = 50$ Mpc bubble size and 1000 hrs of observations	120
5.5	Same as the figure 5.4 for the MWA.	121

Abstract

One of the major challenges in modern cosmology is to understand the reionization history of the Universe. This is directly related to galaxy formation and the formation of the first luminous objects. Observations of redshifted 21-cm radiation from neutral hydrogen (HI) is probably the most promising future probe of reionization. Several approaches have been proposed to extract information about the epoch of reionization from the data which is expected to come in near future.

The most discussed approach has been to study the global statistical properties of the reionization HI 21-cm. We develop the formalism to calculate the Multi-frequency Angular Power Spectrum (MAPS) and quantify the statistics of the HI signal as a joint function of the angular multipole l and frequency separation $\Delta\nu$. We adopt a simple model for the HI distribution which incorporates patchy reionization and use it to study the signatures of ionized bubbles on MAPS. We also study the implications of the foreground subtraction.

This thesis also investigates the possibility of detecting ionized bubbles around individual sources through radio interferometric observations of redshifted HI 21-cm radiation. We present a visibility based matched filter technique to optimally combine the signal from an ionized bubble and minimize the noise and foreground contributions. The formalism makes definite predictions on the ability to detect an ionized bubble or conclusively rule out its presence within a radio map. Results are presented for the GMRT and the MWA. Using simulated HI maps we analyzed the impact of HI fluctuations outside the bubble on its detectability. Various other issues such as (i) bubble size determination (ii) blind search for bubbles, (iii) optimum redshift for bubble detection are also discussed.

Key words: cosmology: theory, cosmology: diffuse radiation, cosmology: large-scale structure of universe, Methods: data analysis

0

xxx

Contents

Title page	i
Certificate of approval	iii
Declaration	v
Certificate by the Supervisor	vii
Acknowledgement	ix
List of Symbols	x
List of Tables	xvii
List of Figures	xix
Abstract	xxix
Contents	xxx
Chapter 1 Introduction	1
1.1 The Epoch of Reionization	2

Contents

1.2	21-cm Tomography	4
1.2.1	Statistical analysis of the 21-cm signal	6
1.2.2	Detecting individual ionized bubbles in 21-cm maps	7
1.3	The Radio- Interferometric Experiments	8
1.4	Challenges to Overcome	9
1.5	Outline of the Thesis	11
Chapter 2 Multi-frequency Angular Power Spectrum of 21 cm Signal		13
2.1	Introduction	13
2.2	Theoretical Formalism	15
2.2.1	The HI power spectrum	15
2.2.2	The multi-frequency angular power spectrum (MAPS)	18
2.2.3	Flat-sky approximation	19
2.2.4	Modeling the HI distribution	23
2.3	Results	29
2.4	Implications for Separating Signal from Foregrounds	35
Chapter 3 Detecting Ionized Bubbles in Redshifted 21 cm Maps		41
3.1	Introduction	41
3.2	Different Sources that Contribute to Low Frequency Radio Observations	42
3.2.1	The HI signal from ionized bubbles	44
3.2.2	HI fluctuations	48
3.2.3	Noise and foregrounds	49
3.3	Formalism for Detecting the Ionized Bubble	54
3.3.1	Baseline distribution	57
3.3.2	Filter	61
3.4	Results and Discussions	63

Chapter 4	Simulating Matched Filter Search for Ionized Bubbles	73
4.1	Introduction	73
4.2	Method of Simulation	75
4.2.1	Simulating visibilities	80
4.2.2	Simulating signal detection	83
4.3	Results	86
4.3.1	Restriction on bubble detection	86
4.3.2	Size determination	89
4.3.3	Determining the position	93
4.3.4	Bubble detection in patchy reionization	96
4.4	Redshift Dependence	102
4.5	Summary	104
Chapter 5	Optimum Redshift for Detecting Ionized Bubbles	107
5.1	Introduction	107
5.2	Ionized Bubbles in Redshifted 21-cm Observations	109
5.3	Matched Filtering Technique to Detect Ionized Bubbles	111
5.4	Redshift Dependence: Scaling Relations	112
5.4.1	Uniform and frequency independent baseline distribution	112
5.4.2	Non uniform and frequency dependent baseline distribution	115
5.4.3	Evolution of neutral fraction with redshift	117
5.5	Optimum Redshift to Detect Ionized Bubbles	118
5.6	Conclusions	121
References		122
Appendix		133

Contents

A Calculation of the angular power spectrum $C_l(\nu_1, \nu_2)$ 133

B Correspondence between all-sky and flat-sky power spectra 135

C Relation between visibility-visibility correlation and MAPS 138

List of Publications **141**

1 Introduction

Understanding the evolutionary history of the Universe is one of the major goals in modern cosmology. Cosmic Microwave Background Radiation (CMBR) observations (COBE*, WMAP†) give a picture of the early Universe (only $\sim 370,000$ years after the Big Bang). During the first $\sim 100,000$ years, the universe was a fully ionized plasma with a strong coupling caused by the Thomson scattering between photons and electrons. Because of adiabatic expansion, the temperature of the Universe dropped down to few thousand Kelvin (~ 3000 K) at redshift $z \sim 1100$ and the protons and electrons combined for the first time to form neutral Hydrogen (HI) atoms. The scattering of photons reduced and they decoupled from baryonic matter. After this the photons were mostly undisturbed except that the expansion of the Universe redshifted them into the microwave at present. This relic background radiation is known as the CMBR. After the recombination, the Universe became almost neutral with 75% and 25% in weight of total baryonic matter was in the form of HI and neutral Helium respectively (neutral Helium formed earlier than the HI). On the other hand observations of Ly alpha forest in quasar (QSO) absorption spectra show the diffuse Hydrogen gas in the Universe to be completely ionized at redshifts $z \leq 5$ (Fan et al. (2002))

*<http://lambda.gsfc.nasa.gov/product/cobe/>

†<http://map.gsfc.nasa.gov/>

1.1 The Epoch of Reionization

The above two observations suggest that the HI of the Universe was ionized sometime in the redshift range $z = 1000$ to 5. The period when the HI was ionized is called the Epoch of Reionization (EoR). The EoR is one of the least known chapters in the evolutionary history of the Universe. Its exact timing, duration, nature of the reionizing sources, their relative contribution to the reionization, large scale distribution and evolution of HI are highly unknown. Again, once the first reionizing sources were formed, their various feedback mechanisms such as mass deposition, energy injection and emitted radiation deeply affect subsequent galaxy formation and influence the evolution of the Intergalactic Medium (IGM). The epoch of reionization, therefore, can be considered as a complicated era which involves a large number of interconnected processes (for a review see Choudhury & Ferrara (2006)). The study reionization has been at the forefront of research over the last few years (Barkana & Loeb (2001); Barkana (2006)).

Though the EoR is yet to be observed in detail, theorists have proposed possible pictures of how the reionization took place. The weak density perturbations which were generated during inflation era grew through gravitational instability and lead to overdense regions. The first generation of galaxies formed at redshift $z \sim 20$ in these overdense regions. The gas in these galaxies cooled by molecular cooling and fragmented. Then the first generation of stars which are believed to be massive ($\sim 100M_{\odot}$) and metal free were created. Enormous amount of radiation produced by these stars ionized the surrounding IGM. Then new generation of galaxies and stars formed. Ionized bubbles thus grow and filled the entire space. In another scenario, black hole were created at the centers of galaxies. Enormous amount of x-ray radiation ionized the IGM.

Currently two types of experiments give information about the EoR. First, the study of Lyman- α line absorption in the high redshift QSO spectra has been used to probe

the ionization state and the HI distribution at high redshifts. The analysis of Gunn-Peterson troughs (Gunn & Peterson (1965)) in the high redshift QSO absorption spectra suggests that reionization finished around redshift $z \sim 6$ (Becker et al. 2001; Fan et al. 2002; White et al. 2003). The study of the dark gap distribution and its evolution in QSO spectra has been shown as an efficient and independent probe of the reionization. This analysis puts an upper limit on the HI fraction $x_{\text{HI}} < 0.36$ at redshift $z = 6.3$ (Gallerani et al., 2008). Measurements of the sizes of HII regions around high redshift QSOs are also consistent with the above results (Fan et al. (2006)). Another independent constraint comes from CMBR observations. The CMBR photons scatter off free electrons (produced during reionization) which results in the suppression of the intrinsic temperature and polarization anisotropies on angular scale below the horizon at EoR. At the same time a polarization signal is generated at large angular scale. The amplitude and the position of the peak in the polarization angular power spectrum depend on the reionization redshift. From recent WMAP measurements of the electron scattering optical depth τ_e from the temperature-polarization and polarization-polarization power spectrum (Page et al. 2007; Dunkley et al. 2008; Komatsu et al. 2008) imply that reionization started before $z \sim 10$. It thus seems from these two experimental results that the EoR is an extended and complex process which occurred over a redshift range $6 - 15$ (Choudhury & Ferrara 2006a; Fan, Carilli & Keating 2006; Alvarez et al. 2006). However, there exist limitations of using these observations to study the details of reionization. The Lyman- α absorption feature (similarly for Lyman- β and Lyman- γ) in QSO spectra is not sensitive to the higher neutral fraction of hydrogen (> 0.1). Therefore, these observations can not be used to probe the reionization at its earlier stages. The CMBR experiments are sensitive only to the integrated history of the EoR and it may not be useful to study the progress of reionization with redshift. In fact, it has been shown that the CMBR polarization power spectrum is weakly dependent on the details of the

1 Introduction

reionization history (Kaplinghat et al. 2003; Hu & Holder 2003; Haiman & Holder 2003; Colombo 2004), though weak constraints could be obtained from upcoming experiments such as PLANCK[‡].

Several other probes have been discussed in the literature to unveil the reionization history of the Universe. According to theory we expect QSOs and massive galaxies to form in highly overdense regions. Moreover first generation stars which are expected to be massive and short lived would produce gamma ray bursts. Observations of high redshift QSOs, galaxies and gamma ray bursts could in principle provide a great deal of information. Though currently available experimental sensitivity is not sufficient enough to detect those, future space based experiments like JWST[§] will have enough sensitivity to detect those objects.

1.2 21-cm Tomography

The interaction between the spins of the proton and the electron in a hydrogen atom in its ground state gives rise to two hyperfine states, i.e., the triplet states of parallel spins and the singlet state of anti-parallel spins. The triplet state has higher energy than the singlet state. When a hydrogen atom jumps from the triplet to the singlet state it emits a photon with the wavelength of 21-cm.

Observations of the redshifted 21 cm line from the EoR is perhaps one of the most promising tools for studying the EoR (for recent review see Furlanetto et al. (2006)). The advantage of this probe lies in the fact that the EoR can be probed at any desired redshift by appropriately tuning the observation frequency. Since HI is distributed all over space these observations have the potential to probe the large scale distribution of

[‡]<http://www.rssd.esa.int/Planck/>

[§]<http://www.jwst.nasa.gov/>

HI. A wealth of information about the EoR can be extracted from these observations. Unlike the observations of QSO absorption spectra the redshifted 21 cm radiation does not suffer from saturation because the optical depth for 21 cm radiation is much less than unity.

The possibility of observing 21 cm emission from the cosmological structure formation was first recognized by Sunyaev and Zeldovich (1972) and later studied by Hogan & Rees (1979), Scott & Rees (1990) and Madau, Meiksin & Rees (, 1997) considering both emission and absorption against the CMBR. More recently, the effect of heating of the HI gas and its reionization on 21 cm signal has drawn great deal of attention and has been studied in detail (Gnedin & Ostriker 1997; Shaver et al. 1999; Tozzi et al. 2000; Iliev et al. 2002, 2003; Ciardi & Madau 2003; Furlanetto, Sokasian & Hernquist 2004; Miralda-Escude 2003; Chen & Miralda-Escude 2004; Cooray & Furlanetto 2005; Cooray 2005; Mcquinn et al. 2006; Sethi 2005; Salvaterra et al. 2005; Carilli 2006).

There could be several approaches in interpreting the data which is expected to come in coming years. Measurements of 21-cm signal in emission averaged over large area of sky would provide a direct probe of the evolution of neutral fraction with redshift(Shaver et al. (1999); Gnedin & Shaver (2004)). Telescopes are being set up to measure this average signal (e.g, Compact Reionization Experiments (CORE) at Australia Telescope National Facility, Experiments to Detect Global EOR Signature (EDGES) at MIT Haystack Observatory). Measurements of the HI power spectrum and individual ionized bubble detection are other two major approaches which are discussed in the following subsections.

1.2.1 Statistical analysis of the 21-cm signal

The most discussed approach has been to study the global statistical properties of the HI distribution through quantities like the power spectrum. The precise measurements of the HI 21-cm fluctuations in terms of their multifrequency angular power spectrum would provide a wealth of information of the size, spatial distribution and evolution of the ionized regions. This would also help us understand the effect of reionization on the structure formation, radiative feedback mechanisms in star-forming zones, the physics of the first generation stars, galaxies etc. This approach has been considered in the context of lower redshifts (Bharadwaj, Nath & Sethi 2001; Bharadwaj & Sethi 2001; Bharadwaj & Pandey 2003; Bharadwaj & Srikant 2004). A similar formalism can also be applied at high redshifts to probe reionization and also the pre-reionization era (Zaldarriaga, Furlanetto & Hernquist 2004; Furlanetto, Zaldarriaga & Hernquist 2004b; Bharadwaj & Ali 2004, 2005; Bharadwaj & Pandey 2005; Ali, Bharadwaj and Pandey 2005, 2006; Loeb & Zaldarriaga 2004; He et al. 2004). It is expected that the radiation from first generation luminous objects changes the character of the 21 cm sky completely. During this epoch, an unique signature of ionized regions will be imprinted on the redshifted 21 cm signal that manifests the processes for the ionizing radiations and that evolves with redshift as reionization proceeds. Chapter 2 presents the multifrequency angular power spectrum (MAPS) of the epoch of reionization 21-cm signal as a joint function of the angular multipole l and frequency separation $\Delta\nu$. This studies the signature of ionized regions (bubbles) on the MAPS and its implication for separating foregrounds from the signal.

1.2.2 Detecting individual ionized bubbles in 21-cm maps

It is believed that the ionizing radiation from QSOs and the stars within galaxies reionize the surrounding neutral IGM. The initial framework for the growth of HII regions around individual galaxies have been developed by Arons & Wingert (1972) and Shapiro & Giroux (1987). Later various types of sophisticated models for the growth of HII regions are prescribed and used to sharpen our understanding about inhomogeneous reionization (Furlanetto, Zaldarriaga & Hernquist 2004a; Cohn & Chang 2007; Kramer et al. 2006). A different, complimentary approach would be to directly observe the individual ionized regions around luminous sources (stars/QSOs). The issue of detecting these bubbles in radio-interferometric observations of redshifted HI 21 cm radiation has been drawing considerable attention. The detection of individual ionized bubbles would be a direct probe of the reionization process. It has also been proposed that such observations will probe the properties of the ionizing sources and the evolution of the surrounding IGM (Wyithe & Loeb, 2004a; Wyithe, Loeb & Barnes, 2005; Kohler et al., 2005; Maselli et al., 2007; Alvarez & Abel, 2007; Geil & Wyithe, 2008; Wyithe, 2008; Geil et al., 2008). Observations of individual ionized bubbles would complement the study of reionization through the power spectrum of HI brightness temperature fluctuations.

Nearly all the above mentioned work on detecting ionized regions consider the contrast between the ionized regions and the neutral IGM in images of redshifted HI 21 cm radiation. The HI signal is expected to be only a small contribution buried deep in the emission from other astrophysical sources (foregrounds) and in the system noise. Chapter 3 introduces a matched filter to optimally combine the entire signal of an ionized bubble while minimizing the noise and foreground contributions. This technique uses the visibilities which are the fundamental quantity measured in radio-interferometric ob-

servations. Using visibilities has an advantage over the image based techniques because the system noise contribution in different visibilities is independent whereas the noise in different pixels of a radio-interferometric images is not. Chapter 4 presents simulation results for bubble detection in 21-cm maps and also studies the size and position determination of ionized bubbles.

1.3 The Radio- Interferometric Experiments

On the experimental side several low frequency radio experiments are either functional or being set up. This motivated us to study the expected redshifted 21 cm background from the EoR and possibility to detect it. Two different observational strategies will be followed. The first approach is to measure the global evolution of mean HI signal with redshift, and second is to measure large scale distribution of HI through the power spectrum measurements and detect the HII regions. In principle both approaches would provide a wealth of information about the reionization. The global signature experiments use a single, small antenna which provides a large field of view (FoV). These will measure the HI 21-cm signal in emission averaged over a large area of the sky. Two main experiments, namely the Cosmological Reionization Experiments (CORE) at the Australian Telescope National Facility, and the Experiment to Detect the Global EoR signature (EDGES), at the MIT Haystack Observatory [¶] are underway in this direction.

The majority of the recent or upcoming radio-interferometric experiments are aimed at measuring the HI 21-cm signal statistically. Individual ionized wholes (bubbles) can also be detected using interferometric observations of HI. The Giant Metre-Wave Radio Telescope (GMRT^{||}; Swarup et al. 1991) is already functioning at several bands

[¶]<http://www.haystack.mit.edu>

^{||}<http://www.gmrt.ncra.tifr.res.in>

in the frequency range 150-1420 MHz and can potentially detect the 21 cm signal at high redshifts. In addition, construction of other low-frequency experiments such as the Murchison Widefield Array (MWA), LOw Frequency ARray (LOFAR**), 21 Centemeter Array (21CMA††), Precision Array to Probe Epoch of Reionization (PAPER), Square Kilometer Array(SKA ‡‡) has raised the possibility to detect 21 cm signal from very high redshifts. The above first generation experiments will probably start their operation at the end of the decade.

1.4 Challenges to Overcome

Although the redshifted 21-cm line can provide enormous amount of information, its detection is going to be a huge challenge. The signal is expected to be highly contaminated by foreground radio emission. Potential sources for these foregrounds include synchrotron and free-free emission from our Galaxy and external galaxies, low-frequency radio point sources and free-free emission from electrons in the IGM (Shaver et al. 1999; DiMatteo. et al. 2002, 2004; Oh & Mack 2003; Gleser et al. 2008; Ali et al. 2008). Contributions from astrophysical foregrounds are expected to be several order of magnitude stronger than the HI signal (Santos, Cooray & Knox (2005)).

However, there have been various proposals for tackling the foregrounds, the most promising being the application of multi-frequency observations. The foregrounds are expected to have a continuum spectra, and the contribution at two different frequencies separated by $\Delta\nu \sim 1$ MHz are expected to be highly correlated. The HI signal, on the other hand, is expected to be uncorrelated at such a frequency separation and this holds the promise of allowing us to separate the signal from the foregrounds. It has been

**<http://www.lofar.org/>

††<http://web.phys.cmu.edu/~past/>

‡‡<http://www.skatelescope.org/>

1 Introduction

proposed that multi-frequency analysis of the radio signal can be useful in separating out the foreground (e.g. Zaldarriaga, Furlanetto & Hernquist 2004; Santos, Cooray & Knox 2005). An alternate approach is to subtract a best fit continuum spectra along each line of sight (Wang et al., 2006) and then determine the power spectrum. This is expected to be an effective foreground subtraction method in data with very low noise levels. Morales et al. (2006) have discussed the complementarity of different foreground removal techniques and the implications for array design and the analysis of reionization data.

The system noise in all low frequency radio experiments relevant for the reionization is dominated by the sky contribution T_{sky} . We also expect T_{sky} to vary depending on whether the source is in the galactic plane or away from it. This is expected to be an independent Gaussian random variable and can be reduced by increasing observation time. The observation time required to detect the HI signal is an important issue.

Man-made radio frequency interference (RFI) is a growing problem in all earth-based radio astronomy. Signal from television, FM radio, satellites, mobile communication, electric spark etc. all fall in the same frequency band as the redshifted 21-cm reionization signal from the reionization. These are expected to be much stronger than the expected 21cm signal, and it is necessary to quantify and characterize the RFI. It has been suggested to construct EoR experiments at remote sites which are expected to have low RFI. Recently Bowman et al. (2007) have characterized the RFI for the MWA site on the frequency range 80 to 300MHz. They find an excellent RFI environment except for a few channels which are dominated by satellite communication signal. There are several methods and techniques being developed to identify, characterize, and ultimately subtract interfering signals (Fridman & Baan 2001; Ellingson 2005). Telescope design also plays a role in mitigating interfering signals (Leshem et al. 2000). The effect of polarization leakage is another issue which needs to be investigated in detail. This could cause polarization structures on the sky to appear as frequency dependent ripples in

the foregrounds intensity . This could be particularly severe for the MWA which has a wide field of view. Radio recombinations lines could be a significant contaminant in the low frequency radio observations. Unfortunately due to lack of observations we have little knowledge of the impact of these lines in the epoch of reionization observation (Morales & Hewitt 2004). Refraction index of Earth’s atmosphere varies significantly in space as well as in time in the frequency band relevant for EoR experiments. This creates significant calibration and imaging problems that must be solved in order to reliably clean the strong foreground contamination (Thompson, Moran & Swenson 1986). This is another important issue related to system noise. The FoV of the individual antenna and the baseline distribution change with observing wavelength and if these are neglected they could cause severe problem in extracting the signal.

1.5 Outline of the Thesis

We give an outline of the rest of the thesis.

Chapter 2 calculates the Multi-frequency Angular Power Spectrum (MAPS) to quantify the statistics of the HI signal as a joint function of the angular multipole l and frequency separation $\Delta\nu$. Assuming a small portion of a spherical sky as a flat-sky we develop formulae for MAPS, including the effect of peculiar velocities (Bharadwaj & Ali (2004)). The flat sky approximation is found to be a good representation over the angular scales of interest. The final expression is very simple to calculate and interpret in comparison to the formulae obtained using full spherical sky. We adopt a simple model for the HI distribution which incorporates patchy reionization and use it to study the signatures of ionized bubbles on MAPS. We also study the implications of the foreground

1 Introduction

subtraction.

Chapter 3 investigates the possibility of detecting individual ionized regions (bubbles) in radio-interferometric observations of HI 21 cm radiation. We develop a visibility based formalism that uses a matched filter to optimally combine the entire signal from a bubble while minimizing the noise and foreground contributions. The method makes definite predictions on the ability to detect an ionized bubble or conclusively rule out its presence within a radio map. We make predictions for the GMRT and the MWA at a frequency of 150 MHz (corresponding to a redshift of 8.5).

Chapter 4 studies the impact of the HI fluctuations outside the bubble that we are trying to detect on the detectability of the bubble in 21-cm maps. We use simulated HI maps which incorporates the patchy reionization scenarios and investigate the restrictions imposed by the HI fluctuations on bubble detection. We validate the matched filter technique presented in Chapter 3 through simulation of bubble detection. We also use the simulations to determine the accuracy to which the GMRT and the MWA will be able to determine the size and position of an ionized bubble, and test if this is limited due to the presence of HI fluctuations.

In **Chapter 5** we estimate the optimum redshift for detecting ionized bubbles in 21-cm maps for different reionization scenarios. We investigate the situations under which bubbles can be detected. Results are also presented in terms of the scaling relations.

2 Multi-frequency Angular Power Spectrum of 21 cm Signal *

2.1 Introduction

In this Chapter, we develop the formalism to calculate the multi-frequency angular power spectrum (hereafter MAPS) which can be used to analyse the 21 cm signal from HI both in emission and absorption against the CMB. We restrict our attention to HI emission which is the situation of interest for the epoch of reionization. In our formalism, we consider the effect of redshift-space distortions which has been ignored in many of earlier works. As noted by Bharadwaj & Ali (2004), this is an important effect and can enhance the mean signal by 50% or more and the effect is expected to be most pronounced in the multi-frequency analysis. We next use the flat sky approximation to develop a much simpler expression of MAPS which is much easier to calculate and interpret than the angular power spectrum written in terms of the spherical Bessel

* *This chapter is adapted from the paper “The multi-frequency angular power spectrum of the epoch of reionization 21 cm signal” by Datta, Choudhury & Bharadwaj (2007).*

2 Multi-frequency Angular Power Spectrum of 21 cm Signal

functions. We adopt a simple model for the HI distribution (Bharadwaj & Ali, 2005) which incorporates patchy reionization and use it to predict the expected signal and study its multi-frequency properties. The model allows us to vary properties like the size of the ionized regions and their bias relative to the dark matter. We use MAPS to analyze the imprint of these features on the HI signal and discuss their implication for future HI observations.

As noted earlier, the HI signal at two different frequencies separated by $\Delta\nu$ is expected to become uncorrelated as $\Delta\nu$ increases. As noted in Bharadwaj & Ali (2005), the value of $\Delta\nu$ beyond which the signal ceases to be correlated depends on the angular scales being observed and it is < 1 MHz in most situations of interest. A prior estimate of the multi-frequency behavior is extremely important when planning HI observations. The width of the individual frequency channels sets the frequency resolution over which the signal is averaged. This should be chosen sufficiently small so that the signal remains correlated over the channel width. Choosing a frequency channel which is too wide would end up averaging uncorrelated HI signal which would wash out various important features in the signal, and also lead to a degradation in the signal to noise ratio. In this context we also note that an earlier work (Santos, Cooray & Knox, 2005) assumed individual frequency channels 1 MHz wide and smoothed the signal with this before performing the multi-frequency analysis. This, as we have already noted and shall study in detail in this Chapter, is considerably larger than the $\Delta\nu$ where the signal is uncorrelated and hence is not the optimal strategy for the analysis. We avoid such a pitfall by not incorporating the finite frequency resolution of any realistic HI observations. It is assumed that the analysis be used to determine the optimal frequency channel width for future HI observations. Further, it is quite straightforward to introduce a finite frequency window into our result through a convolution.

The outline of this Chapter is as follows. In Section 2.2 we present the theoretical

formalism for calculating MAPS of the expected 21 cm signal considering the effect of HI peculiar velocity. The calculation in the full-sky and the flat-sky approximation are both presented with the details being given in separate Appendices. Section 2.2.1 defines various components of the HI power spectrum and Section 2.2.4 presents to models for the HI distribution. We use these models when making predictions for the expected HI signal. We present our results in Section 2.3 and also summarize our findings. In Section 2.4 we discuss the implications for extracting the signal from the foregrounds.

2.2 Theoretical Formalism

2.2.1 The HI power spectrum

The aim of this Section is to set up the notation and calculate the angular correlation C_l for the 21cm brightness temperature fluctuations. It is now well known (e.g.. Bharadwaj & Ali 2005) that the excess brightness temperature observed at a frequency ν along a direction $\hat{\mathbf{n}}$ is given by

$$T(\nu, \hat{\mathbf{n}}) = \bar{T}(z) \eta_{\text{HI}}(z, \hat{\mathbf{n}}r_\nu) \quad (2.1)$$

where the frequency of observation is related to the redshift by $\nu = 1420/(1+z)$ MHz. We consider a flat Universe ($k=0$) in which the comoving distance r_ν can be written as

$$r_\nu = \int_0^z dz' \frac{c}{H(z')}. \quad (2.2)$$

The mean background excess brightness temperature $\bar{T}(z)$ at redshift z is written as

$$\bar{T}(z) \approx 25\text{mK} \sqrt{\frac{0.15}{\Omega_m h^2}} \left(\frac{\Omega_b h^2}{0.022} \right) \left(\frac{1-Y}{0.76} \right) \sqrt{\frac{1+z}{10}} \quad (2.3)$$

2 Multi-frequency Angular Power Spectrum of 21 cm Signal

where $Y \approx 0.24$ is the helium mass fraction and all other symbols have usual meaning. In the above relation, it has been assumed that the Hubble parameter $H(z) \approx H_0 \Omega_m^{1/2} (1+z)^{3/2}$, which is a good approximation for most cosmological models at $z > 3$. The quantity η_{HI} is known as the “21 cm radiation efficiency in redshift space” (Bharadwaj & Ali 2005) and can be written in terms of the mean neutral hydrogen fraction \bar{x}_{HI} and the fluctuation in neutral hydrogen density field δ_{HI} as

$$\begin{aligned} \eta_{\text{HI}}(z, \hat{\mathbf{n}}r_\nu) &= \bar{x}_{\text{HI}}(z)[1 + \delta_{\text{HI}}(z, \hat{\mathbf{n}}r_\nu)] \left(1 - \frac{T_\gamma}{T_s}\right) \\ &\times \left[1 - \frac{(1+z)}{H(z)} \frac{\partial v(z, \hat{\mathbf{n}}r_\nu)}{\partial r_\nu}\right] \end{aligned} \quad (2.4)$$

where T_γ and T_s are the temperature of the CMB and the spin temperature of the gas respectively. The term in the square bracket arises from the coherent components of the HI peculiar velocities. In the above derivation it is assumed that the term $(1+z)\partial v(z, \hat{\mathbf{n}}r_\nu)/\partial r_\nu$ is small compared with $H(z)$ which is a reasonable assumption for the scale of our interest.

At this stage, it is useful to make a set of assumptions which will simplify our analysis: (i) We assume that $T_s \gg T_\gamma$, which corresponds to the scenario where the spin temperature T_s and the gas kinetic temperature are strongly coupled either through strong $Ly\alpha$ scattering or collisional coupling (Madau, Meiksin & Rees, 1997). Though the couplings are expected to be patchy (Higgins & Meiksin 2009) the assumption is reasonable throughout the IGM soon after the formation of first sources of radiation. (ii) We assume that the HI peculiar velocity field is determined by the dark matter fluctuations, which is reasonable as the peculiar velocities mostly trace the dark matter potential wells. This assumption is valid for scales larger than the Jeans length scale

which are the scales of our interest. We then have

$$\eta_{\text{HI}}(z, \hat{\mathbf{n}}r_\nu) = \int \frac{d^3k}{(2\pi)^3} e^{-ikr_\nu(\hat{\mathbf{k}} \cdot \hat{\mathbf{n}})} \tilde{\eta}_{\text{HI}}(z, \mathbf{k}) \quad (2.5)$$

where for $\mathbf{k} \neq 0$

$$\tilde{\eta}_{\text{HI}}(z, \mathbf{k}) = \bar{x}_{\text{HI}}(z) \left[\Delta_{\text{HI}}(z, \mathbf{k}) + (\hat{\mathbf{k}} \cdot \hat{\mathbf{n}})^2 \Delta(z, \mathbf{k}) \right], \quad (2.6)$$

and $\Delta_{\text{HI}}(z, \mathbf{k})$ and $\Delta(z, \mathbf{k})$ are the Fourier transform of the fluctuations in the HI and the dark matter densities respectively. Note that $f(\Omega_m)$, which relates peculiar velocities to the dark matter, has been assumed to have a value $f(\Omega_m) = 1$ which is reasonable at the high z of interest here.

For future use, we define the relevant three dimensional (3D) power spectra

$$\begin{aligned} \langle \Delta(z, \mathbf{k}) \Delta^*(z, \mathbf{k}') \rangle &= (2\pi)^3 \delta_D(\mathbf{k} - \mathbf{k}') P(z, k) \\ \langle \Delta_{\text{HI}}(z, \mathbf{k}) \Delta_{\text{HI}}^*(z, \mathbf{k}') \rangle &= (2\pi)^3 \delta_D(\mathbf{k} - \mathbf{k}') P_{\Delta_{\text{HI}}^2}(z, k) \\ \langle \Delta(z, \mathbf{k}) \Delta_{\text{HI}}^*(z, \mathbf{k}') \rangle &= (2\pi)^3 \delta_D(\mathbf{k} - \mathbf{k}') P_{\Delta_{\text{HI}}}(z, k) \end{aligned} \quad (2.7)$$

where $P(z, k)$ and $P_{\Delta_{\text{HI}}^2}(z, k)$ are the power spectra of the fluctuations in the dark matter and the HI densities respectively, while $P_{\Delta_{\text{HI}}}(z, k)$ is the cross-correlation between the two.

2.2.2 The multi-frequency angular power spectrum (MAPS)

The multi-frequency angular power spectrum of 21 cm brightness temperature fluctuations at two different frequencies ν_1 and ν_2 is defined as

$$C_l(\nu_1, \nu_2) \equiv \langle a_{lm}(\nu_1) a_{lm}^*(\nu_2) \rangle. \quad (2.8)$$

In our entire analysis ν_1 and ν_2 are assumed to differ by only a small amount $\Delta\nu \ll \nu_1$, and it is convenient to introduce the notation

$$C_l(\Delta\nu) \equiv C_l(\nu, \nu + \Delta\nu) \quad (2.9)$$

where we do not explicitly show the frequency ν whose value will be clear from the context. Further, wherever possible, we shall not explicitly show the z dependence of various quantities like \bar{T} , \bar{x}_{HI} , $P(k)$ etc., and it is to be understood that these are to be evaluated at the appropriate redshift determined by ν .

The spherical harmonic moment of $T(\nu, \hat{\mathbf{n}})$ are defined as

$$\begin{aligned} a_{lm}(\nu) &= \int d\Omega Y_{lm}^*(\hat{\mathbf{n}}) T(\nu, \hat{\mathbf{n}}) \\ &= \bar{T} \int d\Omega Y_{lm}^*(\hat{\mathbf{n}}) \int \frac{d^3k}{(2\pi)^3} \tilde{\eta}_{\text{HI}}(\mathbf{k}) e^{-ikr\nu(\hat{\mathbf{k}} \cdot \hat{\mathbf{n}})}. \end{aligned} \quad (2.10)$$

Putting the expression (2.6) for $\tilde{\eta}_{\text{HI}}(\mathbf{k})$ in the above equation, one can explicitly calculate the MAPS in terms of the three dimensional power spectra defined earlier. We give the details of the calculation in Appendix A and present only the final expression for the

angular power spectrum at a frequency ν

$$\begin{aligned}
 C_l(\Delta\nu) = & \frac{2\bar{T}^2 \bar{x}_{\text{HI}}^2}{\pi} \int_0^\infty k^2 dk \left[j_l(kr_\nu) j_l(kr_{\nu_2}) P_{\Delta_{\text{HI}}^2}(k) \right. \\
 & - \{j_l(kr_\nu) j_l''(kr_{\nu_2}) + j_l(kr_{\nu_2}) j_l''(kr_\nu)\} P_{\Delta_{\text{HI}}}(k) \\
 & \left. + j_l''(kr_\nu) j_l''(kr_{\nu_2}) P(k) \right]
 \end{aligned} \tag{2.11}$$

Here $j_l''(x) = \frac{d^2}{dx^2} j_l(x)$ and we have used the notation $r_{\nu_2} = r_\nu + r'_\nu \Delta\nu$ with

$$r'_\nu \equiv \frac{\partial r_\nu}{\partial \nu} = -\frac{c}{\nu_0} \frac{(1+z)^2}{H(z)}. \tag{2.12}$$

Note that equation (2.11) predicts $C_l(\Delta\nu)$ from the cosmological 21 cm HI signal to be real.

With increasing $\Delta\nu$, we expect the two spherical Bessel functions $j_l(kr_{\nu_1})$ and $j_l(kr_{\nu_2})$ to oscillate out of phase. As a consequence the value of $C_l(\Delta\nu)$ is expected to fall increasing $\Delta\nu$. We quantify this through a dimensionless frequency decorrelation function defined as the ratio

$$\kappa_l(\Delta\nu) \equiv \frac{C_l(\Delta\nu)}{C_l(0)}. \tag{2.13}$$

For a fixed multipole l , this fall in this function with increasing $\Delta\nu$ essentially measures how quickly features at the angular scale $\theta \sim \pi/l$ in the 21 cm HI maps at two different frequencies become uncorrelated. Note that $0 \leq |\kappa_l(\Delta\nu)| \leq 1$.

2.2.3 Flat-sky approximation

Radio interferometers have a finite field of view which is determined by the parameters of the individual elements in the array. For example, at 150 MHz this is around 3° for the

2 Multi-frequency Angular Power Spectrum of 21 cm Signal

GMRT. In most cases of interest it suffices to consider only small angular scales which correspond to $l \gg 1$. For the currently favored set of flat Λ CDM models, a comoving length scale R at redshift $z > 5$ would roughly correspond to a multipole

$$l \approx 3 \times 10^4 \left(1 - \frac{1.1}{\sqrt{1+z}}\right) \left(\frac{R}{h^{-1}\text{Mpc}}\right)^{-1} \quad (2.14)$$

Thus, for length scales of $R < 100h^{-1}$ Mpc at $z \approx 10$, one would be interested in multipoles $l > 200$. For such high values of l one can work in the flat-sky approximation.

A small portion of the sky can be well approximated by a plane. The unit vector $\hat{\mathbf{n}}$ towards the direction of observation can be decomposed as

$$\hat{\mathbf{n}} = \mathbf{m} + \boldsymbol{\theta}; \quad \mathbf{m} \cdot \boldsymbol{\theta} = 0; \quad |\boldsymbol{\theta}| \ll 1 \quad (2.15)$$

where \mathbf{m} is a vector towards the center of the field of view and $\boldsymbol{\theta}$ is a two-dimensional vector in the plane of the sky. It is then natural to define the two-dimensional Fourier transform of $T(\nu, \hat{\mathbf{n}})$ in the flat-sky as

$$\tilde{T}(\nu, \mathbf{U}) \equiv \int d^2\theta e^{-2\pi i \mathbf{U} \cdot \boldsymbol{\theta}} T(\nu, \hat{\mathbf{n}}) \quad (2.16)$$

where \mathbf{U} , which corresponds to an inverse angular scale, is the Fourier space counterpart of $\boldsymbol{\theta}$. Using equations (2.1) and (2.5), and the fact that for the flat-sky we can approximate $\mathbf{k} \cdot \hat{\mathbf{n}} \approx \mathbf{k} \cdot \hat{\mathbf{m}} \equiv k_{\parallel}$ we have

$$\tilde{T}(\nu, \mathbf{U}) = \frac{\bar{T}}{2\pi r_{\nu}^2} \int dk_{\parallel} e^{-ik_{\parallel} r_{\nu}} \tilde{\eta}_{\text{HI}}(k_{\parallel} \hat{\mathbf{m}} + 2\pi \mathbf{U}/r_{\nu}). \quad (2.17)$$

It is useful to introduce the $\tilde{\eta}_{\text{HI}}$ power spectrum P_{HI} defined as

$$\langle \tilde{\eta}_{\text{HI}}(\mathbf{k}) \tilde{\eta}_{\text{HI}}(\mathbf{k}') \rangle = (2\pi)^3 \delta_D^3(\mathbf{k} - \mathbf{k}') P_{\text{HI}}(\mathbf{k}). \quad (2.18)$$

This is related to the other three power spectra introduced earlier through

$$P_{\text{HI}}(\mathbf{k}) = \bar{x}_{\text{HI}}^2(z) [P_{\Delta_{\text{HI}}^2}(k) + 2\mu^2 P_{\Delta_{\text{HI}}}(k) + \mu^4 P(k)] \quad (2.19)$$

where $\mu = \hat{\mathbf{m}} \cdot \hat{\mathbf{k}} = k_{\parallel}/k$ (Barkana & Loeb 2005). Note that the anisotropy of $P_{\text{HI}}(\mathbf{k})$ *i.e.*, its μ -dependence arises from the peculiar velocities.

The quantities calculated in the flat-sky approximation can be expressed in terms of their all-sky counterparts. The correspondence between the all-sky angular power spectra and its flat-sky approximation is given by

$$\langle \tilde{T}(\nu_1, \mathbf{U}) \tilde{T}^*(\nu_2, \mathbf{U}') \rangle = C_{2\pi U}(\nu_1, \nu_2) \delta_D^{(2)}(\mathbf{U} - \mathbf{U}') \quad (2.20)$$

where $\delta_D^{(2)}(\mathbf{U} - \mathbf{U}')$ is the two-dimensional Dirac-delta function. The details of the above calculation are presented in Appendix B. Thus allows us to estimate the angular power spectrum C_l under the flat-sky approximation which has a much simpler expression

$$C_l^{\text{flat}}(\Delta\nu) = \frac{\bar{T}^2}{\pi r_\nu^2} \int_0^\infty dk_{\parallel} \cos(k_{\parallel} r'_\nu \Delta\nu) P_{\text{HI}}(\mathbf{k}) \quad (2.21)$$

where the vector \mathbf{k} has magnitude $k = \sqrt{k_{\parallel}^2 + l^2/r_\nu^2}$ *ie.* \mathbf{k} has components k_{\parallel} and l/r_ν along the line of sight and in the plane of the sky respectively. It is clear that the angular power spectrum $C_l(\Delta\nu)$ is calculated by summing over all Fourier modes \mathbf{k} whose projection in the plane of the sky has a magnitude l/r_ν . We also see that C_l is determined by the power spectra only for modes $k \geq l/r_\nu$.

2 Multi-frequency Angular Power Spectrum of 21 cm Signal

The flat-sky angular power spectrum $C_l^{\text{flat}}(0)$ is essentially the 2D power spectrum of the HI distribution on a plane at the distance r_ν from the observer, and for $\Delta\nu = 0$ equation (2.21) is just the relation between the 2D power spectrum and its 3D counterpart (Peacock (1999)). For $\Delta\nu \neq 0$ it is the cross-correlation of the 2D Fourier components of the HI distribution on two different planes, one at r_ν and another at $r_{\nu+\Delta\nu}$. Any 2D Fourier mode is calculated from its full 3D counterparts by projecting the 3D modes onto the plane where the 2D Fourier mode is being evaluated. The same set of 3D modes contribute with different phases when they are projected onto two different planes. This gives rise to $\cos(k_{\parallel} r'_\nu \Delta\nu)$ in equation (2.21) when the same 2D mode on two different planes are cross-correlated and this in turn causes the decorrelation of $C_l^{\text{flat}}(\Delta\nu)$ with increasing $\Delta\nu$.

Testing the range of l over which the flat-sky approximation is valid, we find that for the typical HI power spectra $C_l^{\text{flat}}(\Delta\nu)$ is in agreement with the full-sky $C_l(\Delta\nu)$ calculated using equation (2.11) at a level better than 1 per cent for angular modes $l > 10$. Since the integral in equation (2.21) is much simpler to compute, and more straightforward to interpret, we use the flat-sky approximation of C_l for our calculations in the rest of this Chapter.

Note that equation (2.21) is very similar to the expression for the visibility correlations [equation (16) of Bharadwaj & Ali 2005] expected in radio interferometric observations of redshifted 21 cm HI emission. The two relations differ only in a proportionality factor which incorporates the parameters of the telescope being used for the observation. This reflects the close relation between the visibility correlations, which are the directly measurable quantities in radio interferometry, and the C_l s considered here.

2.2.4 Modeling the HI distribution

The crucial quantities in calculating the angular correlation function are the three dimensional power spectra $P(k)$, $P_{\Delta_{\text{HI}}}(k)$ and $P_{\Delta_{\text{HI}}^2}(k)$. The form of the dark matter power spectrum $P(k)$ is relatively well-established, particularly within the linear theory. We shall be using the standard expression given by (Bunn & White (, 1997)).

The power spectrum of HI density fluctuations $P_{\Delta_{\text{HI}}^2}(k)$ and its cross-correlation with the dark matter fluctuations $P_{\Delta_{\text{HI}}}(k)$ are both largely unknown, and determining these is one of the most important aims of the future redshifted 21 cm observations. A possible approach could be to implement some specific model for reionization, then attempt to predict the expected patchiness in the HI distribution and calculate the power spectra. Such an exercise is somewhat beyond the scope of this paper. The objective here is to quantify the angular power spectrum in terms of the physical attributes characteristic of the HI distribution at the epoch of reionization. To this end we adopt two simple models with a few parameters which capture the salient features of the HI distribution.

The first model, which we shall denote as DM, assumes homogeneous reionization where the HI traces the dark matter, i.e., $\Delta_{\text{HI}} = \Delta$. This model does not introduce a characteristic length-scale in the HI distribution, and hence it serves as the fiducial model against which we can compare the predictions for patchy reionization. Under the standard scenario of reionization by UV sources, this is a valid assumption in very early stages of reionization when most of the IGM is neutral. However, this assumption could have another range of validity. This has to do with the scenarios where the dominant source of reionization are the exotic decaying particles, like neutrinos. In such case, there would be no bubbles associated with individual galaxies, rather the reionization proceeds in a homogeneous manner. In this model we have

$$P_{\Delta_{\text{HI}}^2}(k) = P_{\Delta_{\text{HI}}}(k) = P(k) \quad (2.22)$$

which we use in equation (2.11) to calculate $C_l(\Delta\nu)$. Alternately, we have

$$P_{\text{HI}}(k) = \bar{x}_{\text{HI}}^2 (1 + \mu^2)^2 P(k) \quad (2.23)$$

which we can use in equation (2.21) to calculate $C_l(\Delta\nu)$ in the flat-sky approximation. This model has only one free parameter namely the mean neutral fraction \bar{x}_{HI} .

The second model, denoted as PR, incorporates patchy reionization. It is assumed that reionization occurs through the growth of completely ionized regions (bubbles) in the hydrogen distribution. The bubbles are assumed to be spheres, all with the same comoving radius R , their centers tracing the dark matter distribution with a possible bias b_c . While in reality there will be a spread in the shapes and sizes of the ionized patches, we can consider R as being the characteristic size at any particular epoch. The distribution of the centers of the ionized regions basically incorporates the fact that the ionizing sources are expected to reside at the peaks of the dark matter density distribution and these are expected to be strongly clustered. For non-overlapping spheres the fraction of ionized volume is given by

$$\bar{x}_{\text{HII}} \equiv 1 - \bar{x}_{\text{HI}} = \frac{4\pi R^3}{3} \tilde{n}_{\text{HII}} \quad (2.24)$$

where \tilde{n}_{HII} is the mean comoving number density of ionized spheres and we use \mathcal{R} to denote the ratio $\mathcal{R} = \bar{x}_{\text{HII}}/\bar{x}_{\text{HI}}$. This model has been discussed in detail in Bharadwaj and Ali (2005), and we have

$$\Delta_{\text{HI}}(\mathbf{k}) = [1 - b_c \mathcal{R} W(kR)] \Delta(\mathbf{k}) - \mathcal{R} W(kR) \Delta_P(\mathbf{k}). \quad (2.25)$$

The HI fluctuation is a sum of two parts, one which is correlated with the dark matter distribution and an uncorrelated Poisson fluctuation Δ_P . The latter arises from the discrete nature of the HII regions and has a power spectrum $\tilde{n}_{\text{HII}}^{-1}$. Also, $W(y) = (3/y^3)[\sin y - y \cos y]$ is the spherical top hat window function arising from the Fourier transform of the spherical bubbles. This gives

$$P_{\Delta_{\text{HI}}^2}(k) = [1 - \mathcal{R}b_c W(kR)]^2 P(k) + \frac{[\mathcal{R}W(kR)]^2}{\tilde{n}_{\text{HII}}} \quad (2.26)$$

and

$$P_{\Delta_{\text{HI}}}(k) = [1 - \mathcal{R}b_c W(kR)] P(k) \quad (2.27)$$

which we use in equation (2.11) to calculate $C_l(\Delta\nu)$. Alternately, we have the HI power spectrum (Bharadwaj and Ali, 2005)

$$P_{\text{HI}}(\mathbf{k}) = \bar{x}_{\text{HI}}^2 \left\{ [1 - \mathcal{R}b_c W(kR) + \mu^2]^2 P(k) + \frac{[\mathcal{R}W(kR)]^2}{\tilde{n}_{\text{HII}}} \right\} \quad (2.28)$$

which we can use in equation (2.21) to calculate $C_l(\Delta\nu)$ in the flat-sky approximation.

This model has three independent parameters, namely the average neutral fraction \bar{x}_{HI} , the comoving radius of the ionized bubbles R and the bias of the bubble centers with respect to the dark matter b_c . Our analysis assumes non-overlapping spheres and hence it is valid only when a small fraction of the HI is ionized and the bias is not very large. As a consequence we restrict these parameters to the range $\bar{x}_{\text{HI}} \geq 0.5$ and $b_c \leq 1.5$. We note that in the early stages of reionization (*ie.* $\bar{x}_{\text{HII}} \ll 1$) equation (2.28) matches the HI power spectrum calculated by Wang & Hu (2005), though their method of arriving at the final result is somewhat different and is quite a bit more involved.

Figure 2.1 shows the behaviour of $P_{\text{HI}}(\mathbf{k})$ for the two different models considered here. The cosmological parameters used throughout this paper are those determined as

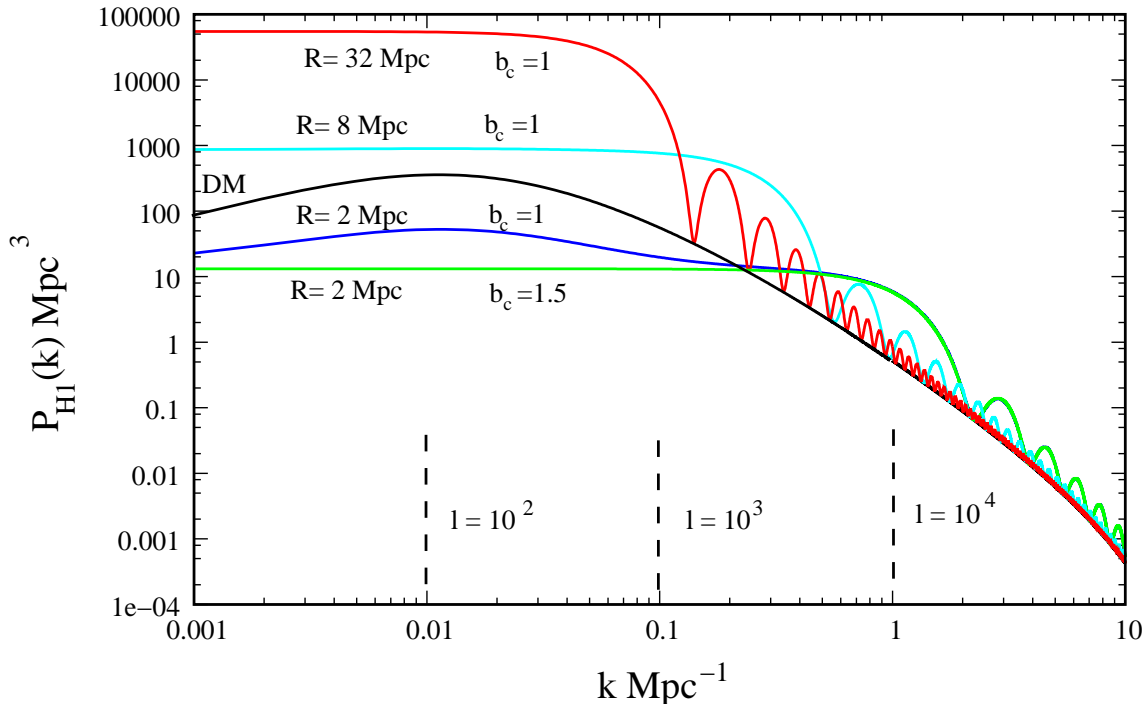


Figure 2.1: The shows the HI power spectrum $P_{\text{HI}}(\mathbf{k})$ for the different models of the HI distribution considered here. Other than the one labeled DM, the curves are all for the PR model with different values of R and b_c as indicated in the figure. Here the μ dependence has been incorporated by using the average value $\langle \mu^2 \rangle = 1/3$.

the best-fit values by WMAP 3-year data release, i.e., $\Omega_m = 0.23$, $\Omega_b h^2 = 0.022$, $n_s = 0.96$, $h = 0.74$, $\sigma_8 = 0.76$ (Spergel et al. 2006). Further, without any loss of generality, we have restricted our analysis to a single redshift $z = 10$ which corresponds to a frequency $\nu = 129$ MHz, and have assumed $\bar{x}_{\text{HI}} = 0.6$ (implying $\mathcal{R} = 2/3$) which is consistent with currently favoured reionization models.

The reason for choosing this particular redshift is that the effects of patchy reionization are expected to be most prominent around $z \approx 10$ in currently favoured reionization models. At higher redshifts, the reionization is in its preliminary stages ($\bar{x}_{\text{HI}} \ll 1$) and the characteristic bubble size R is quite small. This implies that the effects of patchy reionization are not substantial and hence the HI distribution essentially traces the dark matter. Thus our results for the DM model are representative of what is expected at

higher redshifts, just that the overall normalization of $P_{\text{HI}}(\mathbf{k})$ would possibly be z dependent through the values of the growing mode of density perturbations and the neutral fraction. At lower redshifts the HI signal is expected to be drastically diminished because most of the hydrogen would be ionized. Given this, it is optimum to study the HI signal properties at some intermediate redshift where $\bar{x}_{\text{HII}} \sim 0.5$ and R is reasonably large. For the currently favoured reionization scenarios, it seems that these properties are satisfied at $z \approx 10$ (Choudhury & Ferrara 2006a), which we shall be studying in the rest of this paper.

The curve labeled DM in Figure 2.1 shows $P_{\text{HI}}(k)$ when the HI traces the dark matter. The characteristic scale in this power spectrum is set by the Fourier mode entering the horizon at the epoch of matter radiation equality. The imprint of the acoustic oscillations in the dark matter power spectrum holds interesting possibilities for determining cosmological parameters using high- z HI observations, we do not consider this here. The other curves in Figure 2.1 all show the PR model for different values of R and b_c . The point to note is that for large values of the bubble size ($R \geq 8$ Mpc) the power spectrum is essentially determined by the Poisson fluctuation term $P_{\text{HI}}(\mathbf{k}) \approx \bar{x}_{\text{HII}}^2 \mathcal{R}^2 W^2(kR) / \tilde{n}_{\text{HII}} = \bar{x}_{\text{HII}} W^2(kR) (4\pi R^3 / 3)$, which scales as R^3 and is independent of the bias parameter b_c . For length-scales larger than the bubble size ($k < \pi/R$) we have $W^2(kR) \approx 1$, and hence the power spectrum is practically constant $P_{\text{HI}}(\mathbf{k}) \approx \bar{x}_{\text{HII}} (4\pi R^3 / 3)$. Around scales corresponding to the characteristic bubble size $k \approx \pi/R$, the window function $W(kR)$ starts decreasing which introduces a prominent drop in $P_{\text{HI}}(\mathbf{k})$. For smaller length-scales ($k > \pi/R$), the power spectrum shows oscillations arising from the nature of the window function $W(kR)$. At these scales, the amplitude of $W^2(kR)$ decreases as $(kR)^{-4}$ which is more rapid than $P(k)$. Hence, at sufficiently large k the power spectrum $P_{\text{HI}}(\mathbf{k})$ is dominated by the dark matter fluctuations and it approaches the DM model, with the approach being faster for large R . We should

2 Multi-frequency Angular Power Spectrum of 21 cm Signal

mention here that the oscillations in $P_{\text{HI}}(\mathbf{k})$ are a consequence of the fact that we have chosen the ionized bubbles to be spheres, all of the same size. In reality the ionized regions will have a spread in the bubble shapes and sizes, and it is quite likely that such oscillation will be washed out (Wang & Hu 2005) but we expect the other features of the PR model discussed above to hold if the characteristic bubble size is large ($R \geq 8 \text{ Mpc}$).

For smaller values of R , the power spectrum $P_{\text{HI}}(\mathbf{k})$ could be dominated either by the term containing the dark matter power spectrum $P(k)$ or by the Poisson fluctuation term, depending on the value of $\mathcal{R}b_c = 2b_c/3$. For values of $b_c \approx 3/2$, the coefficient of $P(k)$ in equation (2.28) tends to vanish, and hence the Poisson fluctuations dominate. This is obvious from the curve with parameters $\{R, b_c\} = \{2 \text{ Mpc}, 1.5\}$ in Figure 2.1. On the other hand, when the bias parameter is small, say $b_c \leq 1$, the dark matter term dominates over the Poisson fluctuation term at large length-scales ($k < 0.25 \text{ Mpc}^{-1}$), which can be seen from the curve with $\{R, b_c\} = \{2 \text{ Mpc}, 1\}$. There is some difference between this curve and the DM model because of the $\mathcal{R}b_c W(kR)$ factor in equation (2.28). In fact, the PR and DM models exactly coincide at large scales for $\{R, b_c\} = \{2 \text{ Mpc}, 0\}$ which we have not shown separately in Figure 2.1. At small length-scales ($k \gtrsim 0.25 \text{ Mpc}^{-1}$) the amplitude of the dark matter power spectrum becomes less than that of the Poisson fluctuation term, and hence $P_{\text{HI}}(\mathbf{k})$ is independent of b_c (one can see that the curve having $b_c = 1$ overlaps with the one having higher bias factor $b_c = 1.5$). As mentioned earlier, at small length-scales ($kR \gg 1$) we expect the $W^2(kR)$ to decay rapidly as $(kR)^{-4}$, and as a consequence $P_{\text{HI}}(\mathbf{k})$ will basically trace the dark matter. It may be noted that for $R = 2 \text{ Mpc}$ we do not notice this behaviour all the way till $k = 10 \text{ Mpc}^{-1}$ which is shown in the Figure 2.1.

In addition to the effects considered above, the random motions within clusters could significantly modify the signal by elongating the HI clustering pattern along the line of sight [the Finger of God (FoG) effect]. We have incorporated this effect by multiplying

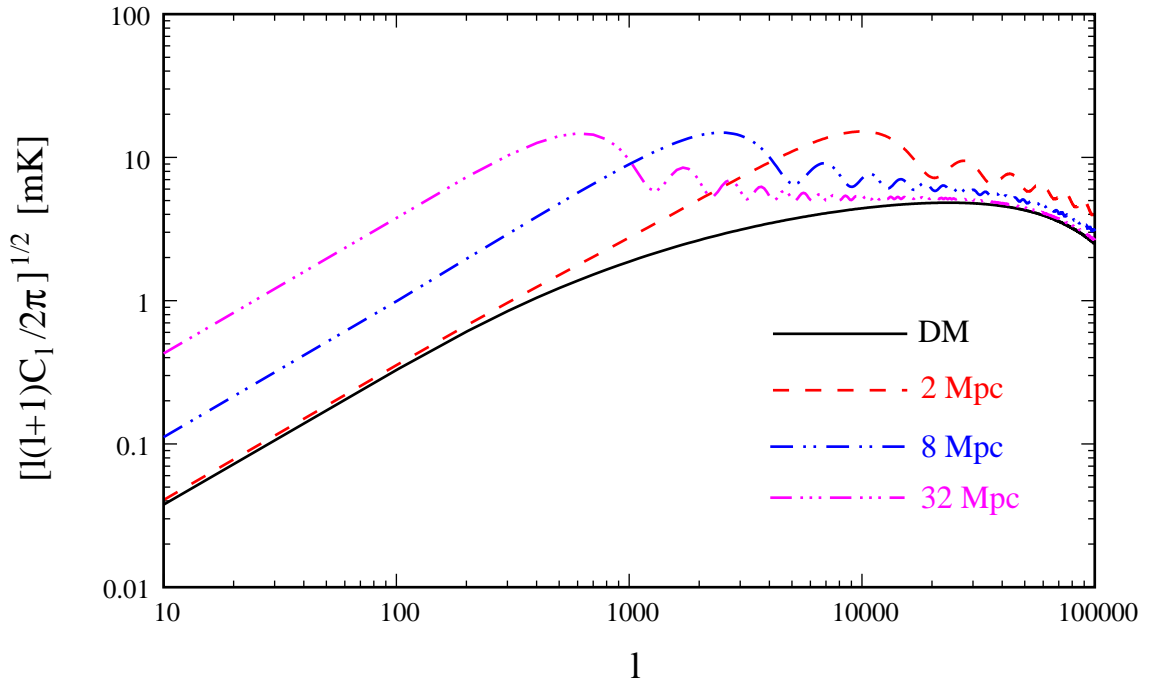


Figure 2.2: The angular power spectrum of HI brightness temperature fluctuations for different models of the HI distribution assuming $b_c = 1$ and $\sigma_p = 0$.

the power spectrum $P_{\text{HI}}(\mathbf{k})$ with an extra Lorentzian term $(1 + k_{\parallel}^2 \sigma_P^2 / a^2 H^2)^{-1}$ (Sheth 1996; Ballinger et al. 1996) where σ_P is the one dimensional pair-velocity dispersion in relative galaxy velocities.

2.3 Results

We first consider the angular power spectrum $C_l(\Delta\nu)$ at $\Delta\nu = 0$ for which the results are shown in Figure 2.2. As discussed earlier, $C_l(0)$ is essentially the 2D power spectrum of HI fluctuations evaluated at the 2D Fourier mode $l/r_\nu \approx l \times 10^{-4} \text{Mpc}^{-1}$. The results for the DM model serve as the fiducial case against which we compare different possibilities for patchy reionization.

For large bubble size ($R \geq 8 \text{ Mpc}$) the HI signal is dominated by Poisson fluctuations

2 Multi-frequency Angular Power Spectrum of 21 cm Signal

and it is well described through

$$\sqrt{l(l+1)}C_l \propto \sqrt{x_{\text{HI}}}\bar{T} \frac{R}{r_\nu} l \quad (2.29)$$

on scales larger than the bubble. At these angular scales the HI signal is substantially enhanced compared to the DM model. For smaller bubble size, the large angle signal is sensitive to the bias b_c . The signal is very similar to the DM model for $b_c = 0$ and it is suppressed for higher bias. In all cases (large or small bubble size), the signal is Poisson fluctuation dominated on scales comparable to the bubble size and it peaks at $l \approx \pi r_\nu / R$, with no dependence on b_c . The HI signal traces the dark matter on scales which are much smaller than the bubble size.

We next consider the behavior of $\kappa_l(\Delta\nu)$, the frequency decorrelation function shown in Figure 2.3. For the DM model (upper left panel) where the HI fluctuations trace the dark matter we find that the frequency difference $\Delta\nu$ over which the HI signal remains correlated reduces monotonically with increasing l . For example, while for $l = 100$ $\kappa_l(\Delta\nu)$ falls to ~ 0.5 at $\Delta\nu \sim 500$ KHz, it occurs much faster ($\Delta\nu \sim 10$ KHz) for $l = 10^5$. Beyond the first zero crossing $\kappa_l(\Delta\nu)$ becomes negative (anti-correlation) and exhibits a few highly damped oscillations very close to zero. These oscillations arise from the cos term in equation (2.21). The change in the behavior of $\kappa_l(\Delta\nu)$ for the DM model arising from the FoG effect is also shown in the same panel. Wang & Hu (2005) have proposed that σ_p is expected to have a value ~ 30 km/s at $z \sim 8$; in view of this, we show results for $\sigma_p = 20$ and 40 km/s. We find that there is a discernible change at $l \geq 10^4$, and the FoG effect causes the signal to remain correlated for a larger value of $\Delta\nu$. For $\sigma_p = 20$ km/s, the change is at most 15% for $l = 10^4$ and around 100% at $l = 10^5$. Though we have not shown it explicitly, we expect similar changes due to FoG effect in the PR model also.

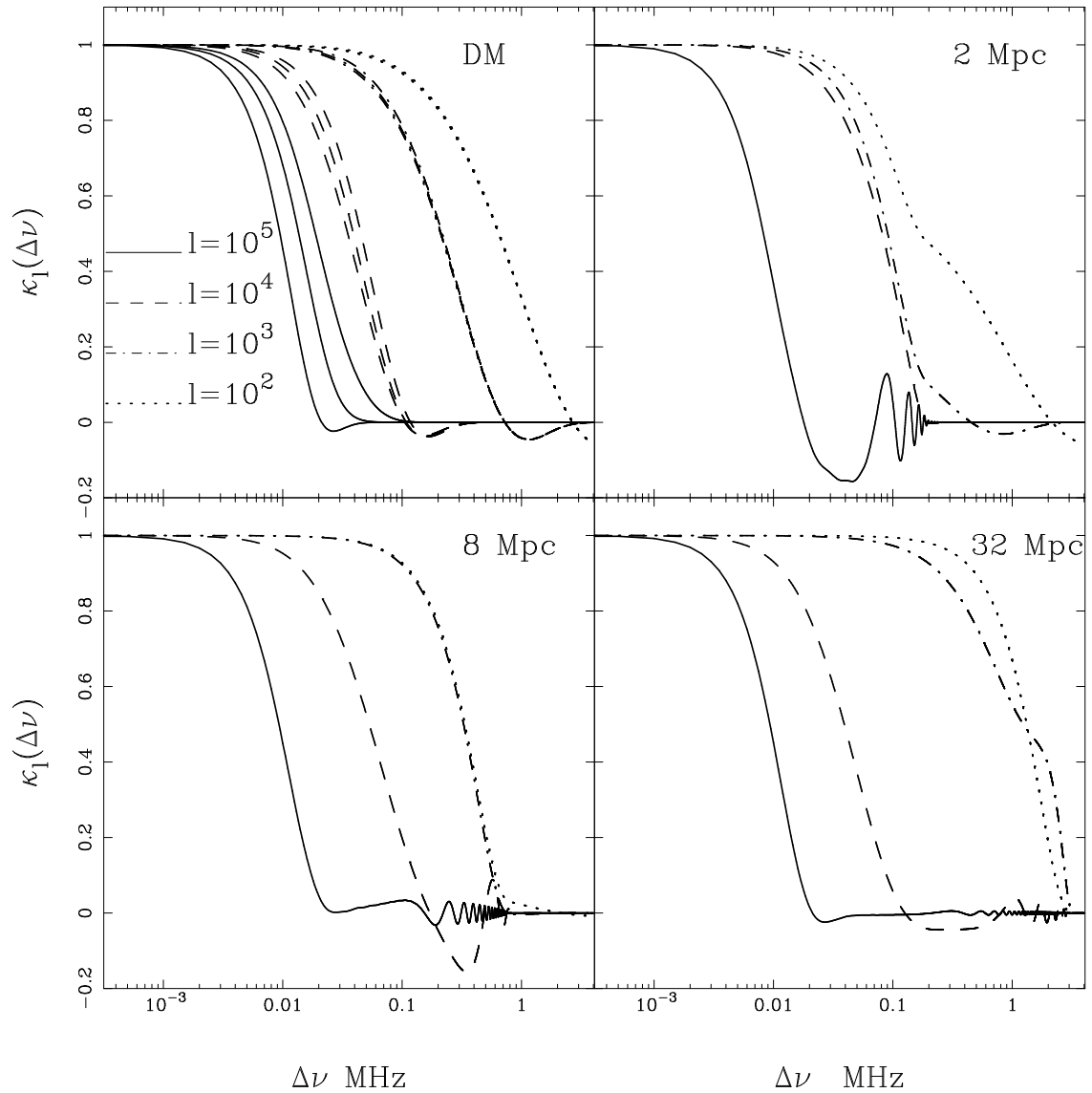


Figure 2.3: The frequency decorrelation function $\kappa_l(\Delta\nu)$ [defined in equation (2.13)] at $l = 10^2, 10^3, 10^4, 10^5$. Results are shown for the DM model and the PR model with $b_c = 1$ and the R values shown in the figure. For the DM model, we show results incorporating the FoG effect using $\sigma_P = 20$ and 40 km/s. For each l value $\kappa_l(\Delta\nu)$ decreases faster for $\sigma_P = 0$ and slowest for $\sigma_P = 40$ km/s. There is a significant change due to the FoG effect only at $l \geq 10^4$.

2 Multi-frequency Angular Power Spectrum of 21 cm Signal

The patchy reionization model shows distinct departures from the DM model in the behavior of $\kappa_l(\Delta\nu)$. This reflects the imprint of the bubble size and the bias on the $\Delta\nu$ dependence. For $R = 2$ Mpc and $b_c = 1$ (upper right panel) the large l ($l > 1000$, comparable to bubble size) behavior is dominated by the Poisson fluctuation of the individual bubbles which makes $\kappa_l(\Delta\nu)$ quite distinct from the DM model. Notice that for $l = 10^3$, $\kappa_l(\Delta\nu)$ falls faster than the DM model whereas for $l = 10^4$ it falls slower than the DM model causing the $l = 10^3$ and 10^4 curves to nearly overlap. The oscillations seen in C_l as a function of l in Figure 2.2 are also seen in the $\Delta\nu$ dependence of $\kappa_l(\Delta\nu)$ at large l (10^5). The behavior at $l = 10^2$ is a combination of the dark matter and the ionized bubbles, and is sensitive to b_c . For $b_c = 1$, the initial decrease in $\kappa_l(\Delta\nu)$ is much steeper than the DM model with a sudden break after which the curve flattens. Figure 2.4 shows the b_c dependence for $l = 10^2$ and 10^3 . The bias dependence is weak for $l = 10^3$ where the Poisson fluctuations begin to dominate. For $l = 10^2$, changing b_c has a significant affect only near the break in $\kappa_l(\Delta\nu)$ leaving much of the curve unaffected. For a smaller bubble size we expect a behavior similar to $R = 2$ Mpc, with the b_c dependence being somewhat more pronounced and the Poisson dominated regime starting from a larger value of l .

For large bubble size ($R \geq 8$ Mpc) the large angle HI signal ($l < \pi r_\nu/R$) is entirely determined by the Poisson fluctuations where the signal is independent of l . This is most clearly seen for $R = 8$ Mpc where the $\kappa_l(\Delta\nu)$ curves for $l = 10^2$ and $l = 10^3$ are identical. For both $R = 8$ Mpc and 32 Mpc the large l behavior of $\kappa_l(\Delta\nu)$ approaches that of the DM model.

In the final part we quantify the frequency difference $\Delta\nu$ across which the HI signal at two different frequencies remain correlated. To be more precise, we study the behavior of $\Delta\nu_{1/2}$ which is defined such that $\kappa_l(\Delta\nu_{1/2}) = 1/2$ *ie.* the correlation falls to 50% of its peak value at $\Delta\nu = 0$. We study this for different angular scales (different l) for the

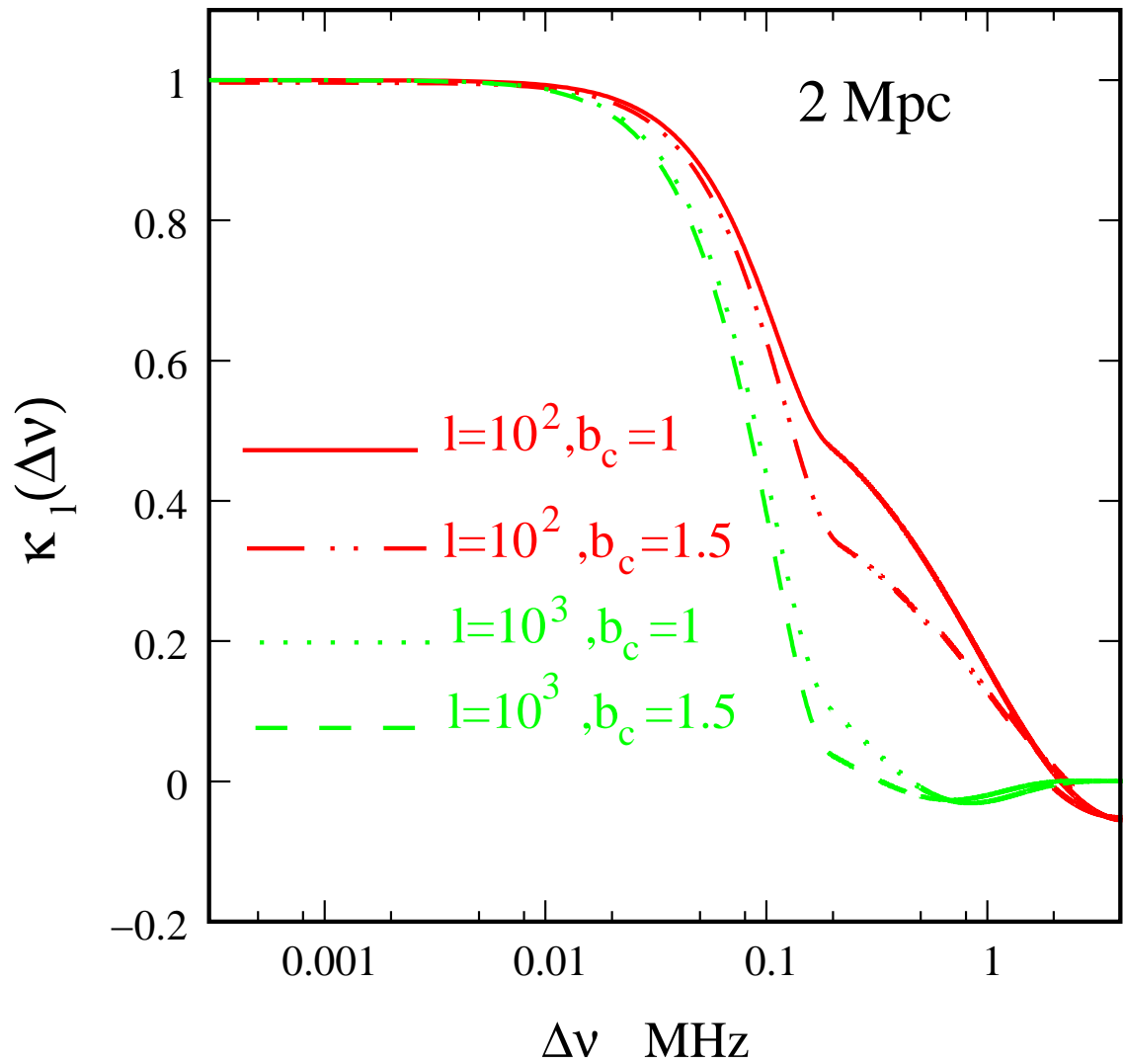


Figure 2.4: This shows the b_c dependence of the frequency decorrelation function $\kappa_l(\Delta\nu)$ for the PR model with $R = 2$ Mpc.

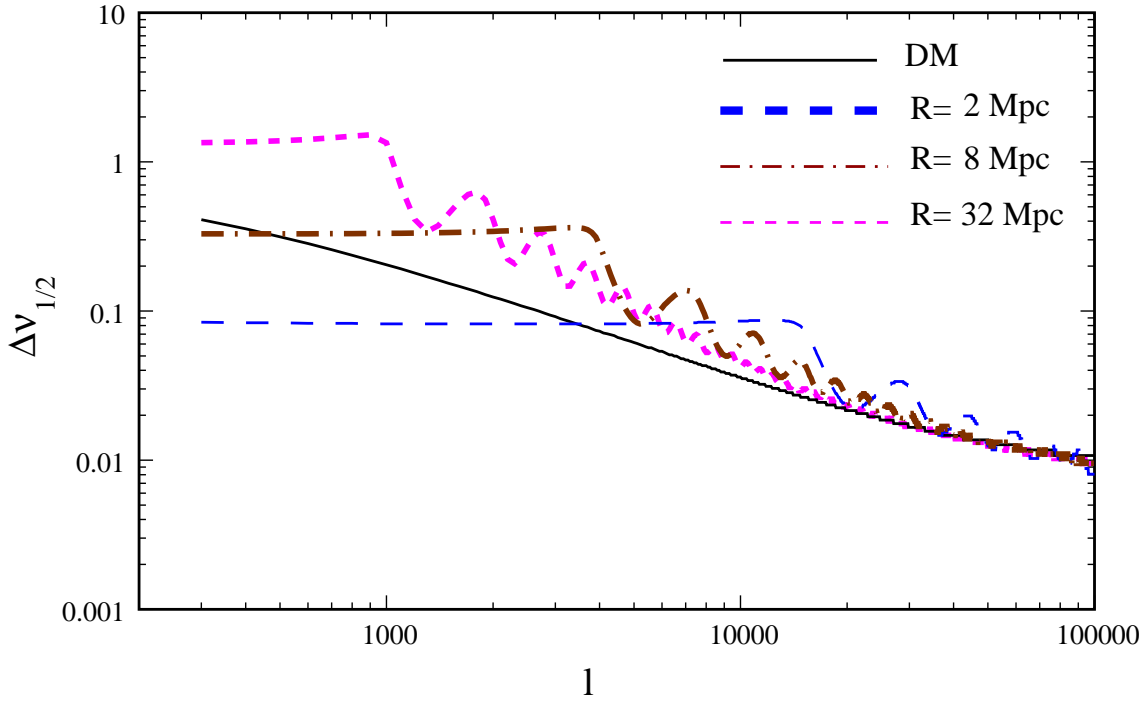


Figure 2.5: This shows $\Delta\nu_{1/2}$ vs. l for the DM model and the PR model with $b_c = 1$ for the R values shown in the figure.

various models of HI distribution considered here. The main aim of this exercise is to determine the frequency resolution that would be required to study the HI fluctuations on a given angular scale l . Optimally one would like to use a frequency resolution smaller than $\Delta\nu_{1/2}$. A wider frequency channel would combine different uncorrelated signals whereby the signal would cancel out. Further, combining such signals would not lead to an improvement in the signal to noise ratio. Thus it would be fruitful to combine the signal at two different frequencies only as long as they are correlated and not beyond, and we use $\Delta\nu_{1/2}$ to estimate this. The plot of $\Delta\nu_{1/2}$ vs l for the different HI models is shown in Figure 2.5.

We find that for the DM model $\Delta\nu_{1/2}$ falls monotonically with l and the relation is well approximated by a power law

$$\Delta\nu_{1/2} = 0.2 \text{ MHz} \times \left(\frac{l}{10^3} \right)^{-0.7} \quad (2.30)$$

2.4 Implications for Separating Signal from Foregrounds

which essentially says that $\Delta\nu_{1/2} \sim 0.66$ MHz on 1° angular scales, $\Delta\nu_{1/2} \sim 0.04$ MHz on $1'$ angular scales and $\Delta\nu_{1/2} \sim 2$ KHz on $1''$ angular scales.

For the PR model, as discussed earlier, $\kappa_l(\Delta\nu)$ is l independent on angular scales larger than the bubble size $l < \pi r_\nu/R$. As a consequence $\Delta\nu_{1/2}$ also is independent of l and it depends only on the bubble size R . This can be well approximated by

$$\Delta\nu_{1/2} \approx 0.04 \text{ MHz} \left(\frac{R}{\text{Mpc}} \right) \quad (2.31)$$

which given a large value 1.3 MHz for $R = 32$ Mpc while it falls below the DM model for 0.08 MHz for $R = 2$ Mpc. The large l behavior of $\Delta\nu_{1/2}$ approaches the DM model though there are oscillations which persist even at large l .

We note that our findings are consistent with the earlier findings of Bharadwaj & Ali (2005) whereas they significantly different from the results of Santos, Cooray & Knox (2005) who assume frequency channels of 1 MHz which is too large.

2.4 Implications for Separating Signal from Foregrounds

Astrophysical foregrounds are expected to be several order of magnitude stronger than the 21 cm signal. The MAPS foreground contribution at a frequency ν can be parametrized as (Santos, Cooray & Knox, 2005)

$$C_l(\Delta\nu) = A \left(\frac{\nu_f}{\nu} \right)^{\bar{\alpha}} \left(\frac{\nu_f}{\nu + \Delta\nu} \right)^{\bar{\alpha}} \left(\frac{1000}{l} \right)^\beta I_l(\Delta\nu) \quad (2.32)$$

where $\nu_f = 130$ MHz and $\bar{\alpha}$ is the mean spectral index. The actual spectral index varies with line of sight across the sky and this causes the foreground contribution to decorrelate with increasing frequency separation $\Delta\nu$ which is quantified through the foreground fre-

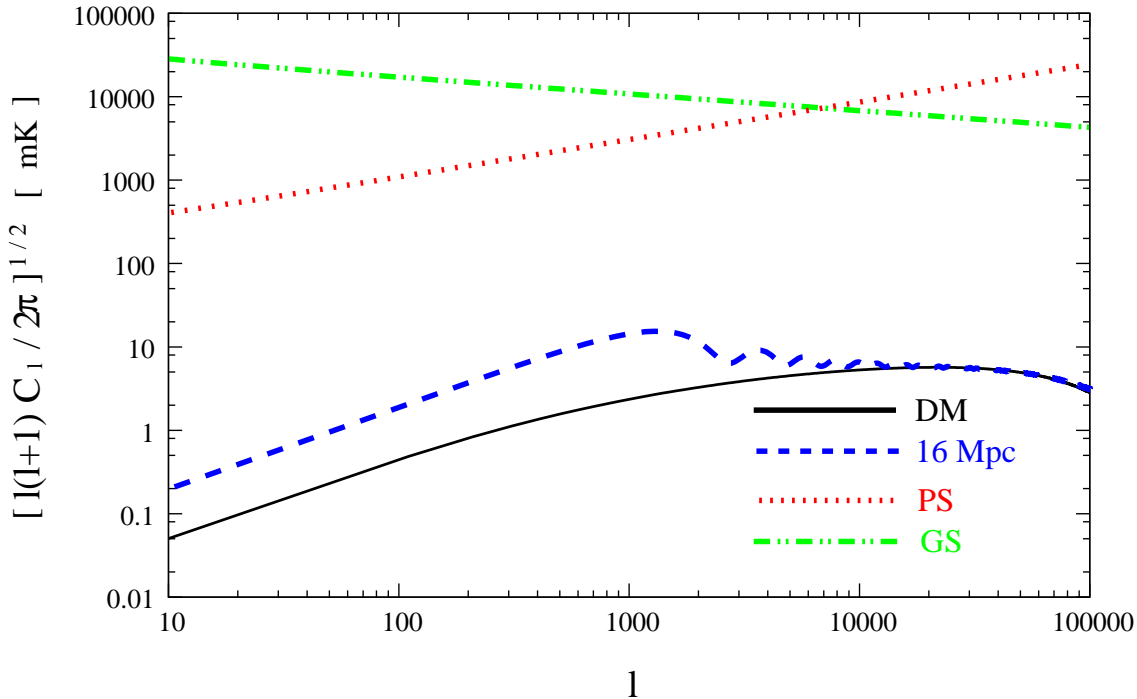


Figure 2.6: Angular power spectrum $C_l(0)$ at $\nu = 129$ MHz for the two most dominant foreground components, the diffuse galactic synchrotron radiation (GS) and the extragalactic point sources (PS) assuming $S_{cut} = 0.1$ mJy. The expected signal is also shown for the DM model and the PR model with $R = 16$ Mpc.

quency decorrelation function $I_l(\Delta\nu)$ (Zaldarriaga, Furlanetto & Hernquist, 2004) which has been modeled as

$$I_l(\Delta\nu) = \exp \left[-\log_{10}^2 \left(1 + \frac{\Delta\nu}{\nu} \right) / 2\xi^2 \right]. \quad (2.33)$$

We consider the two most dominant foreground components namely extragalactic point sources and the diffuse synchrotron radiation from our own galaxy. Point sources above a flux level S_{cut} can be identified in high-resolution images and removed. We assume $S_{cut} = 0.1$ mJy and adopt the parameter values from Table 1 of Santos, Cooray & Knox (2005) for A , $\bar{\alpha}$, β and ξ . Figure 2.6 shows the expected $C_l(0)$ for the signal and foregrounds. The galactic synchrotron radiation dominates at large angular scales $l < 10,000$

2.4 Implications for Separating Signal from Foregrounds

while the extragalactic point sources dominate at small angular scales. For all values of l , the foregrounds are at least two orders of magnitude larger than the signal.

The foregrounds have a continuum spectra, and the contributions at a frequency separation $\Delta\nu$ are expected to be highly correlated. For $\Delta\nu = 1$ MHz, the foreground decorrelation function $I_l(\Delta\nu)$ falls by only 2×10^{-6} for the galactic synchrotron radiation and by 3×10^{-5} for the point sources. In contrast, the HI decorrelation function $\kappa_l(\Delta\nu)$ is nearly constant at very small $\Delta\nu$ and then has a sharp drop well within 1 MHz, and is largely uncorrelated beyond. This holds the promise of allowing the signal to be separated from the foregrounds. A possible strategy is to cross-correlate different frequency channels of the full data which has both signal and foregrounds, and to use the distinctly different $\Delta\nu$ dependence to separate the signal from the foregrounds (Zaldarriaga, Furlanetto & Hernquist, 2004). An alternate approach is to subtract a best fit continuum spectra along each line of sight (Wang et al., 2006) and then determine the power spectrum. This is expected to be an effective foreground subtraction method in data with very low noise levels. We consider the former approach here, and discuss the implications of our results.

MAPS characterizes the joint l and $\Delta\nu$ dependence which is expected to be different for the signal and the foregrounds. For a fixed l , it will be possible to separate the two with relative ease at a frequency separation $\Delta\nu$ if the decrement in the signal $C_l(0)[1 - \kappa_l(\Delta\nu)]$ is more than that of the foregrounds $C_l(0)[1 - I_l(\Delta\nu)]$. Note that because the foregrounds are much stronger than the HI signal, a very small decorrelation of the foreground contribution may cause a decrement in $C_l(\Delta\nu)$ which is larger than that due to the signal. We use $F_l(\Delta\nu)$ defined as the ratio of the two decrements

$$F_l(\Delta\nu) = \frac{\{C_l(0)[1 - \kappa_l(\Delta\nu)]\}_{\text{Signal}}}{\{C_l(0)[1 - I_l(\Delta\nu)]\}_{\text{Foregrounds}}} \quad (2.34)$$

2 Multi-frequency Angular Power Spectrum of 21 cm Signal

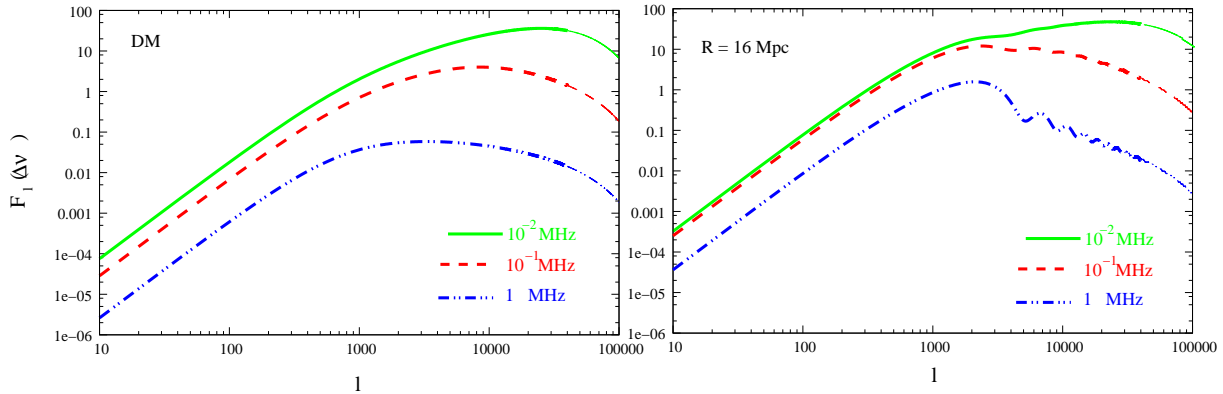


Figure 2.7: This shows $F_l(\Delta\nu)$ (defined in equation 2.34) for the $\Delta\nu$ values shown in the figure. We consider both the DM model(left panel) and the PR model(right panel).

to assess the feasibility of separating the HI signal from the foregrounds. This gives an estimate of the accuracy at which the $\Delta\nu$ dependence of the foreground $C_l(\Delta\nu)$ has to be characterized for the signal to be detected. Note we assume that the $(\frac{\nu_f}{\nu+\Delta\nu})^{\bar{\alpha}}$ term in eq. (2.32) can be factored out before considering the decrement in the foreground. Figure 2.7 shows the results for the DM model and the PR model with $R = 16$ Mpc. First we note that $F_l(\Delta\nu)$ peaks at the angular scales corresponding to $l \sim 10,000$ (*ie.* $2'$) and the prospects of separating the signal from the foregrounds are most favorable at these scales. A detection will be possible in the range $l > 1000$, $\Delta\nu \leq 10$ KHz and $l > 400$, $\Delta\nu \leq 100$ KHz for the DM and PR models respectively provided the $\Delta\nu$ dependence of the foregrounds $C_l(\Delta\nu)$ can be characterized with an uncertainty less than order unity. The l and $\Delta\nu$ range would increase if the $\Delta\nu$ dependence of the foreground $C_l(\Delta\nu)$ were characterized to 10% accuracy. The largest angular scales ($l < 100$) would require an accuracy better than 1% which would possibly set the limit for forthcoming observations.

The angular modes $l = 1,000$ and $l = 10,000$ correspond to baselines with antenna separations of ~ 300 m and ~ 3 km respectively. This baseline range is quite well covered by the GMRT, and also the forthcoming interferometric arrays. This is possibly

2.4 Implications for Separating Signal from Foregrounds

the optimal range for a detection. A possible detection strategy would be to use the $\Delta\nu$ behavior of $C_l(\Delta\nu)$ in the range where $F_l(\Delta\nu) \ll 1$ to characterize the foreground contribution. This can be extrapolated to predict the foreground contribution at small $\Delta\nu$ and any excess relative to this prediction can be interpreted as the HI signal. A very precise determination of the $\Delta\nu$ dependence of the foreground contribution would require a very large $\Delta\nu$ range in the region where $F_l(\Delta\nu) \ll 1$, and a bandwidth of ~ 10 MHz would be appropriate. On the other hand, at $l \sim 10,000$ the HI $C_l(\Delta\nu)$ decorrelates within ~ 50 KHz [or equivalently $F_l(\Delta\nu)$ shows a considerable drop between 10 KHz and 100 KHz, see Figure 2.7], and it would be desirable to have a frequency resolution better than ~ 10 KHz to optimally differentiate between the signal and the foregrounds. A lower resolution of ~ 20 KHz would possibly suffice at $l \sim 1,000$, particularly if the PR model holds.

2 Multi-frequency Angular Power Spectrum of 21 cm Signal

3 Detecting Ionized Bubbles in Redshifted 21 cm Maps *

3.1 Introduction

In this Chapter we consider the possibility of detecting ionized bubbles in redshifted 21 cm HI maps. An ionized bubble embedded in HI will appear as a decrement in the background redshifted 21 cm radiation. This decrement will typically span across several pixels and frequency channels in redshifted 21 cm maps. Detecting this is a big challenge because the HI signal (~ 1 mJy or lower) will be buried in foregrounds which are expected to be at least 2 – 3 orders of magnitude larger. An objective detection criteria which optimally combines the entire signal in the bubble while minimizing contributions from foregrounds, system noise and other such sources is needed to search for ionized bubbles. The noise in different pixels of maps obtained from radio-interferometric observations is correlated (eg. Thompson, Moran & Swenson (1986)), and it is most convenient to deal with visibilities instead. These are the primary quantities that are measured in radio-interferometry.

* *This chapter is adapted from the paper “Detecting ionized bubbles in redshifted 21 cm maps” by Datta, Bharadwaj & Choudhury (2007).*

In this Chapter we develop a visibility based formalism to detect an ionized bubble or conclusively rule it out in radio-interferometric observations of HI at high redshifts. We apply our formalism for detecting ionized bubbles to make predictions for the GMRT and for one of the forthcoming instruments, namely the MWA. For both telescopes we investigate the feasibility of detecting the bubbles, and in situations where a detection is feasible we predict the required observation time. For both telescopes we make predictions for observations only at a single frequency (150MHz), the aim here being to demonstrate the utility of our formalism and not present an exhaustive analysis of the feasibility of detecting ionized bubbles in different scenarios and circumstances. For the GMRT we have used the telescope parameters from their website, while for the MWA we use the telescope parameters from Bowman et al. (2006).

The outline of the Chapter is as follows: In Section 3.2 we discuss various sources which are expected to contribute in low frequency radio-interferometric observation, this includes the signal expected from an ionized bubble. In Section 3.3 we present the formalism for detecting an ionized bubble, and in Section 3.4 we present the results and discuss its implications. The cosmological parameters used throughout this Chapter are those determined as the best-fit mean values for a flat Λ CDM model by WMAP 3-year data release, i.e., $\Omega_m = 0.23$, $\Omega_b h^2 = 0.022$, $n_s = 0.96$, $h = 0.74$, $\sigma_8 = 0.76$ (Spergel et al. 2006).

3.2 Different Sources that Contribute to Low Frequency Radio Observations

The quantity measured in radio-interferometric observations is the visibility $V(\vec{U}, \nu)$ which is measured in a number of frequency channels ν across a frequency bandwidth

3.2 Different Sources that Contribute to Low Frequency Radio Observations

B for every pair of antennas in the array. For an antenna pair, it is convenient to use $\vec{U} = \vec{d}/\lambda$ to quantify the antenna separation \vec{d} projected in the plane perpendicular to the line of sight in units of the observing wavelength λ . We refer to \vec{U} as a baseline. The visibility is related to the specific intensity pattern on the sky $I_\nu(\vec{\theta})$ as

$$V(\vec{U}, \nu) = \int d^2\theta A(\vec{\theta}) I_\nu(\vec{\theta}) e^{2\pi i \vec{\theta} \cdot \vec{U}} \quad (3.1)$$

where $\vec{\theta}$ is a two dimensional vector in the plane of the sky with origin at the center of the field of view, and $A(\vec{\theta})$ is the beam pattern of the individual antenna. For the GMRT this can be well approximated by Gaussian $A(\vec{\theta}) = e^{-\theta^2/\theta_0^2}$ where $\theta_0 \approx 0.6 \theta_{\text{FWHM}}$ and we use the values 2.28° for θ_0 at 150 MHz for the GMRT. Each MWA antenna element consists of 16 crossed dipoles distributed uniformly in a square shaped tile, and this is stationary with respect to the earth. The MWA beam pattern is quite complicated, and it depends on the pointing angle relative to the zenith (Bowman et al., 2007). Our analysis largely deals with the beam pattern within 1° of the pointing angle where it is reasonable to approximate the beam as being circularly symmetric (Figures 3 and 5 of Bowman et al. 2007). We approximate the MWA antenna beam pattern as a Gaussian with $\theta_0 = 18^\circ$ at 153 MHz. Note that the MWA primary beam pattern is better modeled as $A(\vec{\theta}) \propto \cos^2(K\theta)$, but a Gaussian gives a reasonable approximation in the center of the beam which is the region of interest here. Equation (3.1) is valid only under the assumption that the field of view is small so that it can be well approximated by a plane, or under the unlikely circumstances that all the antennas are coplanar.

The visibility recorded in 150 MHz radio-interferometric observations is a combination of three separate contributions

$$V(\vec{U}, \nu) = S(\vec{U}, \nu) + N(\vec{U}, \nu) + F(\vec{U}, \nu) \quad (3.2)$$

where $S(\vec{U}, \nu)$ is the HI signal that we are interested in, $N(\vec{U}, \nu)$ is the system noise which is inherent to the measurement and $F(\vec{U}, \nu)$ is the contribution from other astrophysical sources referred to as the foregrounds. Man-made radio frequency interference (RFI) from cell phones and other communication devices are also expected to contribute to the measured visibilities. Given the lack of a detailed model for the RFI contribution, and anticipating that it may be possible to remove it before the analysis, we do not take it into account here.

3.2.1 The HI signal from ionized bubbles

According to models of reionization by UV sources, the early stages of reionization are characterized by ionized HII regions around individual source (QSOs or galaxies). As a first approximation, we consider these regions as ionized spherical bubbles characterized by three parameters, namely, its comoving radius R_b , the redshift of its center z_c and the position of the center determined by the two-dimensional vector in the sky-plane $\vec{\theta}_c$. The bubble is assumed to be embedded in an uniform intergalactic medium (IGM) with a neutral hydrogen fraction x_{HI} . We use r_ν to denote the comoving distance to the redshift where the HI emission, received at a frequency $\nu = 1420 \text{ MHz}/(1+z)$, originated, and define $r'_\nu = dr_\nu/d\nu$. The planar section through the bubble at a comoving distance r_ν is a disk of comoving radius $R_\nu = R_b \sqrt{1 - (\Delta\nu/\Delta\nu_b)^2}$ where $\Delta\nu = \nu_c - \nu$ is the distance from the the bubble center ν_c in frequency space with $\nu_c = 1420 \text{ MHz}/(1+z_c)$ and $\Delta\nu_b = R_b/r'_{\nu_c}$ is the bubble size in the frequency space. The bubble, obviously, extends from $\nu_c - \Delta\nu_b$ to $\nu_c + \Delta\nu_b$ in frequency and in each frequency channel within this frequency range the image of the ionized bubble is a circular disk of angular radius $\theta_\nu = R_\nu/r_\nu$; the bubble is not seen in HI beyond this frequency range. Under such

3.2 Different Sources that Contribute to Low Frequency Radio Observations

assumptions, the specific intensity of the redshifted HI emission is

$$I_\nu(\vec{\theta}) = \bar{I}_\nu x_{\text{HI}} \left[1 - \Theta \left(1 - \frac{|\vec{\theta} - \vec{\theta}_c|}{\theta_\nu} \right) \right] \Theta \left(1 - \frac{|\nu - \nu_c|}{\Delta\nu_b} \right) \quad (3.3)$$

where $\bar{I}_\nu = 2.5 \times 10^2 \frac{Jy}{sr} \left(\frac{\Omega_b h^2}{0.02} \right) \left(\frac{0.7}{h} \right) \left(\frac{H_0}{H(z)} \right)$ is the radiation background from the uniform HI distribution and $\Theta(x)$ is the Heaviside step function.

The soft X-ray emission from the quasar responsible for the ionized region is expected to heat the neutral IGM in a shell around the ionized bubble. The HI emission from this shell is expected to be somewhat higher than \bar{I}_ν (Wyithe & Loeb, 2004a). We do not expect this to make a very big contribution, and we do not consider this here.

If we assume that the angular extent of the ionized bubble is small compared to the angular scale of primary beam *ie.* $\theta_\nu \ll \theta_0$, we can take $A(\vec{\theta})$ outside the integral in eq. (3.1) and write the signal as $A(\vec{\theta}_c) \int d^2\theta I_\nu(\vec{\theta}) e^{2\pi i \vec{\theta} \cdot \vec{U}}$, which essentially involves a Fourier transform of the circular aperture $\Theta \left(1 - |\vec{\theta} - \vec{\theta}_c| r_\nu / R_\nu \right)$. For example, a bubble of radius as large as 40 Mpc at $z = 8.5$ would have an angular size of only $\theta_\nu \approx 0.25^\circ$ which satisfies the condition $\theta_\nu \ll \theta_0$. In a situation where the bubble is at the center of the field of view, the visibility is found to be

$$S_{\text{center}}(\vec{U}, \nu) = -\pi \bar{I}_\nu x_{\text{HI}} \theta_\nu^2 \left[\frac{2J_1(2\pi U \theta_\nu)}{2\pi U \theta_\nu} \right] \Theta \left(1 - \frac{|\nu - \nu_c|}{\Delta\nu_b} \right) \quad (3.4)$$

where $J_1(x)$ is the first order Bessel function. Note that $S_{\text{center}}(\vec{U}, \nu)$ is real and it is the Fourier transform of a circular aperture. The uniform HI background also contributes $\bar{I}_\nu \pi \theta_0^2 e^{-\pi^2 \theta_0^2 U^2}$ to the visibility, but this has been dropped as it is quite insignificant at the baselines of interest. Note that the approximations used in eqs. (3.4) have been tested extensively by comparing the values with the numerical evaluation of the integral in eq. (3.1). We find that the two match to a high level of accuracy for the situations of

3 Detecting Ionized Bubbles in Redshifted 21 cm Maps

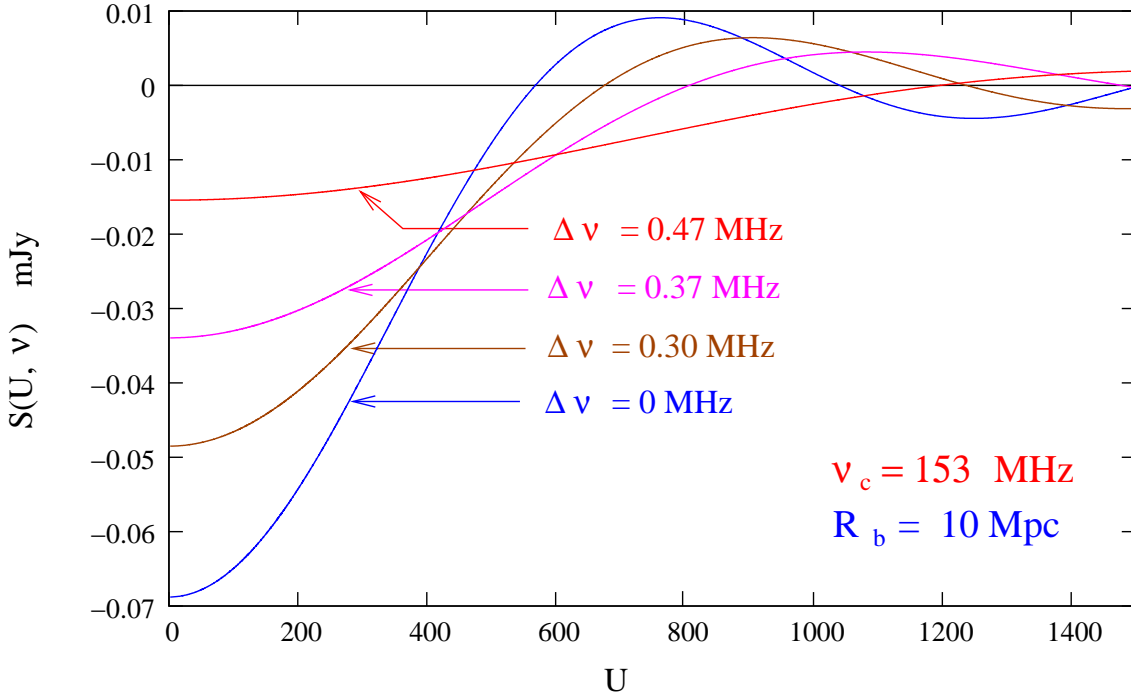


Figure 3.1: Signal from a spherical ionized bubble of comoving radius 10 Mpc as a function of baseline U for different frequency channels.

interest here. In the general situation where the bubble is shifted by $\vec{\theta}_c$ from the center of the field of view, the visibility is given by

$$S(\vec{U}, \nu) = e^{-\theta_c^2/\theta_0^2} e^{2\pi i \vec{U} \cdot \vec{\theta}_c} S_{\text{center}}(\vec{U}, \nu) \quad (3.5)$$

i.e., there is a phase shift of $e^{2\pi i \vec{U} \cdot \vec{\theta}_c}$ and a $e^{-\theta_c^2/\theta_0^2}$ drop in the overall amplitude.

Figures 3.1 and 3.2 show the U and $\Delta\nu$ dependence of the visibility signal from an ionized bubble with $R_b = 10$ Mpc located at the center of the field of view at $\nu_c = 153$ MHz ($z_c = 8.3$), assuming $x_{\text{HI}} = 1$. The signal extends over $\Delta\nu = \pm\Delta\nu_b$ where $\Delta\nu_b = 0.56$ MHz. The extent in frequency $\Delta\nu_b = R_b/r'_{\nu_c}$ scales $\propto R_b$ when the bubble size is varied. The Bessel function $J_1(x)$ has the first zero crossing at $x = 3.83$. As a result, the signal $S(\vec{U}, \nu)$ extends to $U_0 = 0.61 r_\nu [R_b \sqrt{1 - (\Delta\nu/\Delta\nu_b)^2}]^{-1}$ where it has the first zero crossing, and U_0 scales with the bubble size as $U_0 \propto 1/R_b$. The peak value

3.2 Different Sources that Contribute to Low Frequency Radio Observations

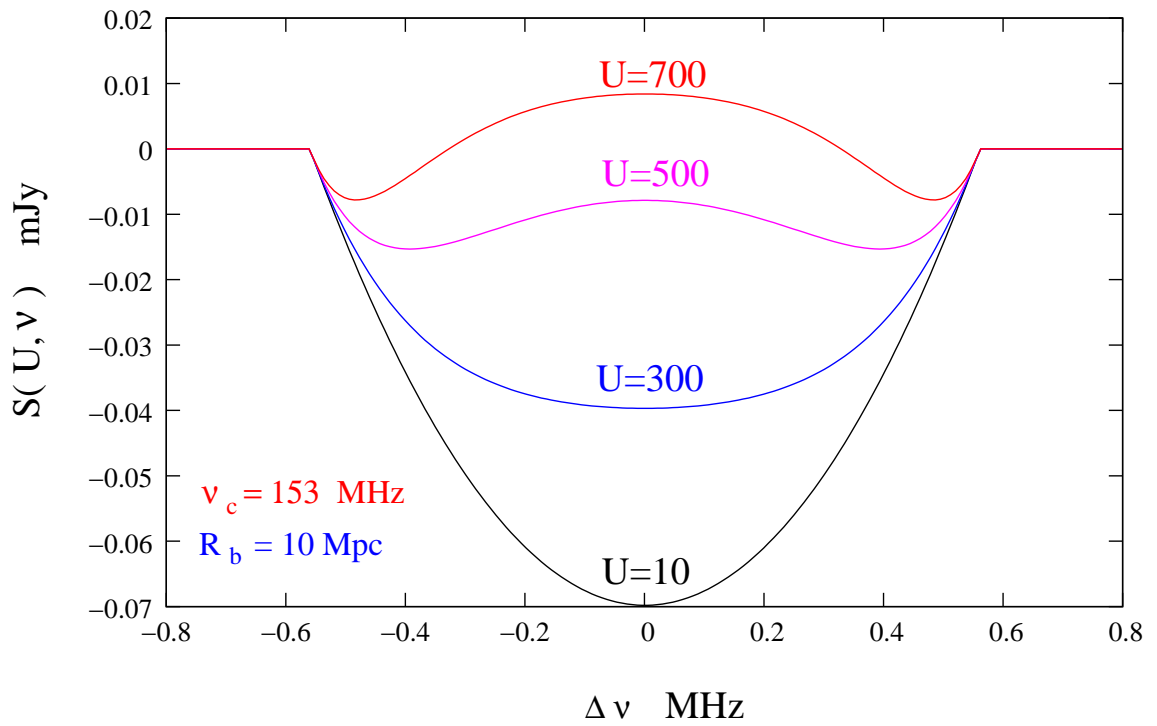


Figure 3.2: Signal from a spherical ionized bubble of comoving radius 10 Mpc as a function of $\Delta \nu = \nu - \nu_c$ for different baselines.

3 Detecting Ionized Bubbles in Redshifted 21 cm Maps

of the signal is $S(0, \nu) = \pi \bar{I}_\nu (R_b/r_\nu)^2 \sqrt{1 - (\Delta\nu/\Delta\nu_b)^2}$ and scales as $S(0, \nu) \propto R_b^2$ if the bubble size is varied. We see that the peak value of the signal is $S(0, \nu_c) = 70 \mu\text{Jy}$ for bubble size $R_b = 10 \text{ Mpc}$ and would increase to 1.75 mJy if $R_b = 50 \text{ Mpc}$. Detecting these ionized bubbles will be a big challenge because the signal is buried in noise and foregrounds which are both considerably larger in amplitude. Whether we are able to detect the ionized bubbles or not depends critically on our ability to construct optimal filters which discriminate the signal from other contributions.

3.2.2 HI fluctuations

In the previous sub-section, we assumed the ionized bubble to be embedded in a perfectly uniform IGM. In reality, however, there would be fluctuations in the HI distribution in the IGM which, in turn, would contribute to the visibilities. This contribution to the HI signal can be treated as a random variable $\hat{S}(\vec{U}, \nu)$ with zero mean $\langle \hat{S}(\vec{U}, \nu) \rangle = 0$, whose statistical properties are characterized by the two-visibility correlation $\langle \hat{S}(\vec{U}_1, \nu_1) \hat{S}^*(\vec{U}_2, \nu_2) \rangle$. This is related to $P_{\text{HI}}(\mathbf{k})$ the power spectrum of the 21 cm radiation efficiency in redshift space (Bharadwaj & Ali, 2004) through

$$\begin{aligned} \langle \hat{S}(\vec{U}_1, \nu) \hat{S}^*(\vec{U}_2, \nu + \Delta\nu) \rangle &= \delta_{\vec{U}_1, \vec{U}_2} \frac{\bar{I}_\nu^2 \theta_0^2}{2r_\nu^2} \\ &\times \int_0^\infty dk_{\parallel} P_{\text{HI}}(\mathbf{k}) \cos(k_{\parallel} r'_\nu \Delta\nu) \end{aligned} \quad (3.6)$$

where $\delta_{\vec{U}_1, \vec{U}_2}$ is the Kronecker delta *ie.* different baselines are uncorrelated, To estimate the contribution from the HI fluctuations we make the simplifying assumption that the HI traces the dark matter, which gives $P_{\text{HI}}(\mathbf{k}) = \bar{x}_{\text{HI}}^2 (1 + \mu^2)^2 P(k)$ where $P(k)$ is the dark matter power spectrum and μ is the cosine of the angle between \mathbf{k} and the line of sight. This assumption is reasonable because the scales of interest are much larger than

3.2 Different Sources that Contribute to Low Frequency Radio Observations

the Jeans length $\lambda_J \sim 10 - 100$ kpc, and we expect the HI to cluster in the same way as the dark matter.

In addition to the above, there could be other contributions to the HI signal too. For example, there would be several other ionized regions in the field of view other than the bubble under consideration. The Poisson noise from these ionized patches will increase the HI fluctuations and there will also be an overall drop in the contribution because of the reduced neutral fraction. These effects will depend on the reionization model, and the simple assumptions made would only provide a representative estimate of the actual contribution. Figure 3.3 shows the expected contribution from the HI fluctuations (HF) to the individual visibilities for GMRT and MWA. Note that while this can be considerably larger than the signal that we are trying to detect (particularly when the bubble size is small), there is a big difference between the two. The signal from the bubble is correlated across different baselines and frequency channels whereas the contribution from random HI fluctuations is uncorrelated at different baselines and it become uncorrelated beyond a certain frequency separation $\Delta\nu$ (Bharadwaj & Ali, 2005; Datta, Choudhury & Bharadwaj, 2007).

3.2.3 Noise and foregrounds

The system noise contribution $N(\vec{U}, \nu)$ in each baseline and frequency channel is expected to be an independent Gaussian random variable with zero mean ($\langle \hat{N} \rangle = 0$) and whose variance is independent of \vec{U} and ν_c . The predicted rms. noise contribution is (Thompson, Moran & Swenson (1986))

$$\sqrt{\langle \hat{N}^2 \rangle} = \frac{\sqrt{2}k_B T_{sys}}{A_{eff} \sqrt{\Delta\nu_c \Delta t}} \quad (3.7)$$

3 Detecting Ionized Bubbles in Redshifted 21 cm Maps

where T_{sys} is the total system temperature, k_B is the Boltzmann constant, A_{eff} is the effective collecting area of each antenna, $\Delta\nu_c$ is the channel width and Δt is the correlator integration time. Equation (3.7) can be rewritten as

$$\sqrt{\langle \hat{N}^2 \rangle} = C^x \left(\frac{\Delta\nu_c}{1\text{MHz}} \right)^{-1/2} \left(\frac{\Delta t}{1\text{sec}} \right)^{-1/2} \quad (3.8)$$

where C^x varies for different interferometric arrays. Using the GMRT parameters $T_{sys} = 482\text{K}$ and $A_{eff}/2k_B = 0.33\text{K/Jy}$ at 153MHz gives $C^x = 1.03\text{Jy}$ for the GMRT where as for MWA $T_{sys} = 470\text{K}$ and $A_{eff}/2k_B = 5 \times 10^{-3}\text{K/Jy}$ (Bowman et al., 2006) gives $C^x = 65.52\text{Jy}$. The rms noise is reduced by a factor $\sqrt{\Delta t/t_{obs}}$ if we average over $t_{obs}/\Delta t$ independent observations where t_{obs} is the total observation time. Figure 3.3 shows the expected noise for a single baseline at 153MHz for $\Delta\nu_c = 50\text{KHz}$ and an observation time of 100 hrs for both the GMRT and MWA. Though T_{sys} is nearly equal for the GMRT and the MWA, the noise in a single baseline is expected to be 60 times larger for MWA than that for the GMRT. This is because the individual antennas have a much larger collecting area at the GMRT as compared to the MWA. The fact that the MWA has many more antennas ($N = 500$) as compared to the GMRT ($N = 30$) compensates for this. Note that nearly half (16) of the GMRT antennas are at very large baselines which are not particularly sensitive to the signal on the angular scales the ionized bubble, and only the other 14 antennas in the $1\text{km} \times 1\text{km}$ central square will contribute towards detecting the signal. For both the GMRT and the MWA, T_{sys} is dominated by the sky contribution T_{sky} with the major contribution coming from our Galaxy. We expect T_{sys} to vary depending on whether the source is in the Galactic plane or away from it. The value which we have used is typical for directions off the Galactic plane. Further, the noise contribution will also be baseline dependent which is not included in our analysis.

Contributions from astrophysical foregrounds are expected to be several order of

3.2 Different Sources that Contribute to Low Frequency Radio Observations

magnitude stronger than the HI signal. Extragalactic point sources and synchrotron radiation from our Galaxy are predicted to be the most dominant foreground components. Assuming that the foregrounds are randomly distributed, with possible clustering, we have $\langle \hat{F}(U, \nu) \rangle = 0$ for all the baselines other than the one at zero spacing ($U = 0$), which is not considered in this work. The statistical properties are characterized by the two-visibility correlation $\langle \hat{F}(\vec{U}_1, \nu_1) \hat{F}(\vec{U}_2, \nu_2) \rangle$. We express this (details in Appendix C) in terms of the multi-frequency angular power spectrum (hereafter MAPS) $C_l(\nu_1 \nu_2)$ of the brightness temperature fluctuations at the frequencies ν_1 and ν_2 as (Santos, Cooray & Knox, 2005; Datta, Choudhury & Bharadwaj, 2007)

$$\langle \hat{F}(\vec{U}_1, \nu_1) \hat{F}(\vec{U}_2, \nu_2) \rangle = \delta_{\vec{U}_1, -\vec{U}_2} \pi \left(\frac{\theta_1^2 \theta_2^2}{\theta_1^2 + \theta_2^2} \right) \left(\frac{\partial B}{\partial T} \right)_{\nu_1} \left(\frac{\partial B}{\partial T} \right)_{\nu_2} C_{2\pi U_1}(\nu_1 \nu_2). \quad (3.9)$$

where $(\partial B / \partial T)_\nu = 2k_B \nu^2 / c^2$ is the conversion factor to specific intensity, and we have assumed that the primary beam pattern $A(\theta) = e^{-\theta^2 / \theta_0^2}$ is frequency dependent through $\theta_0 \propto \nu^{-1}$ and use θ_1 and θ_2 to denote the value of θ_0 at ν_1 and ν_2 respectively. Note that the foreground contribution to different baselines are expected to be uncorrelated.

For each component of the foreground the MAPS is modeled as

$$C_l(\nu_1 \nu_2) = A \left(\frac{\nu_f}{\nu_1} \right)^{\bar{\alpha}} \left(\frac{\nu_f}{\nu_2} \right)^{\bar{\alpha}} \left(\frac{1000}{l} \right)^\beta I_l(\nu_1 \nu_2). \quad (3.10)$$

where $\nu_f = 130$ MHz, and for each foreground component A , β and $\bar{\alpha}$ are the amplitude, the power law index of the angular power spectrum and the mean spectral index respectively. The actual spectral index varies with line of sight across the sky and this causes the foreground contribution to decorrelate with increasing frequency separation $\Delta\nu = |\nu_1 - \nu_2|$ which is quantified through the foreground frequency decorrelation func-

3 Detecting Ionized Bubbles in Redshifted 21 cm Maps

tion $I_l(\nu_1 \nu_2)$ (Zaldarriaga, Furlanetto & Hernquist, 2004) which has been modeled as

$$I_l(\nu_1 \nu_2) = \exp \left[-\log_{10}^2 \left(\frac{\nu_2}{\nu_1} \right) / 2\xi^2 \right]. \quad (3.11)$$

We consider the two most dominant foreground components namely extragalactic point sources and the diffuse synchrotron radiation from our own galaxy. Point sources above a flux level S_{cut} can be identified in high-resolution continuum images and removed. We note that absence of large baselines at the MWA restricts the angular resolution, but it may be possible to use the large frequency bandwidth 32 MHz to identify continuum point sources in the frequency domain. S_{cut} depends on σ the rms. noise in the image. We use $S_{cut} = 5\sigma$ where σ is the rms noise in the image given by (assuming 2 polarizations)

$$\sigma = \frac{C^x}{\sqrt{2N_b}} \left(\frac{B}{1\text{MHz}} \right)^{-1/2} \left(\frac{t_{obs}}{1\text{sec}} \right)^{-1/2} \quad (3.12)$$

where $N_b = N(N - 1)/2$ is the number of independent baselines, N is the number of antennas in the array, B is the total frequency bandwidth and t_{obs} the total observation time. For $t_{obs} = 100$ hrs and $B = 6$ MHz we have $S_{cut} = 0.1$ mJy for the GMRT and using $B = 32$ MHz it gives $S_{cut} = 0.2$ mJy for the MWA. The value of S_{cut} will be smaller for longer observations, but reducing S_{cut} any further does not make any difference to our results so we hold S_{cut} fixed at these values for the rest of our analysis. The confusion noise from the unresolved point sources is a combination of two parts, the Poisson contribution due to the discrete nature of these sources and the clustering contribution. The amplitude of these two contributions have different S_{cut} dependence. The parameter values that we have used are listed in Table 3.1. We have adopted the parameter values from Santos, Cooray & Knox (2005) and incorporated the S_{cut} dependence from DiMatteo. et al. (2002).

3.2 Different Sources that Contribute to Low Frequency Radio Observations

Table 3.1: Parameters values used for characterizing different foreground contributions

Foregrounds	$A(\text{mK}^2)$	$\bar{\alpha}$	β	ξ
Galactic synchrotron	700	2.80	2.4	4
Point source (clustered part)	$61 \left(\frac{S_{cut}}{0.1\text{mJy}} \right)^{0.5}$	2.07	1.1	2
Point source (Poisson part)	$0.16 \left(\frac{S_{cut}}{0.1\text{mJy}} \right)^{1.25}$	2.07	0	1

Figure 3.3 shows the expected foreground contributions for the GMRT and MWA. The galactic synchrotron radiation is the most dominant foreground component at large angular scales ($U < 1000$ for GMRT and $U < 2000$ for MWA), while the clustering of the unresolved extragalactic point sources dominates at small angular scales. For all values of U , the foregrounds are at least four orders of magnitude larger than the signal, and also considerably larger than the noise.

The MWA has been designed with the detection of the statistical HI fluctuation signal in mind, and hence it is planned to have a very large field of view. The foreground contribution to a single baseline is expected to be 10 times stronger for the MWA than for the GMRT because of a larger field of view. As we shall show later, the increased foreground contribution is not a limitation for detecting HII bubbles. The foregrounds have a continuum spectra, and the contribution at two different frequencies at a separation $\Delta\nu$ are expected to be highly correlated. For $\Delta\nu = 1$ MHz, the foreground decorrelation function $I_l(\Delta\nu)$ falls by only 2×10^{-6} for the galactic synchrotron radiation and by 3×10^{-5} for the point sources. In contrast, the signal from an ionized bubble peaks at a frequency corresponding to the bubble center and falls rapidly with $\Delta\nu$ (Figure 3.2). This holds the promise of allowing the signal to be separated from the foregrounds.

3 Detecting Ionized Bubbles in Redshifted 21 cm Maps

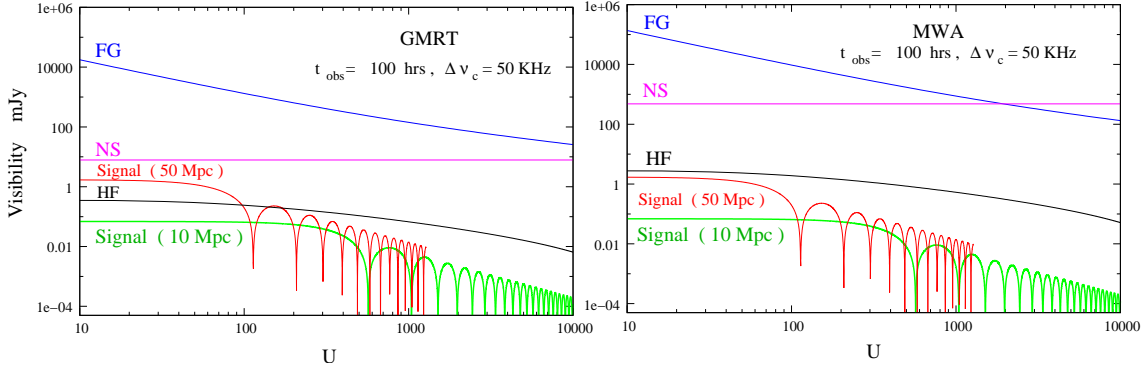


Figure 3.3: The magnitude of the different contributions to the visibility $V(\vec{U}, \nu)$ at $\nu = 153$ MHz as a function of U . The signal, foregrounds (FG), noise (NS) and HI fluctuations (HF) contributions are shown for the GMRT (left) and MWA (right). The expected signal is shown for bubbles with radius $R = 10$ Mpc and $R = 50$ Mpc. The noise is estimated for a single baseline assuming an observation time $t_{obs} = 100$ hrs and channel width $\Delta\nu_c = 50$ KHz.

3.3 Formalism for Detecting the Ionized Bubble

We consider a radio-interferometric observation of duration t_{obs} , carried out over the frequency range ν_1 to ν_2 . The HI signal from an ionized bubble, if it is present in the data, will be buried in foregrounds and noise both of which are expected to be much larger. In this Section we present a filtering technique aimed at detecting the signal from an ionized bubble if it is present in our observations. To detect the signal from an ionized bubble of radius R_b with center at redshift z_c (or frequency ν_c) and at an angle $\vec{\theta}_c$ from the center of the field of view, we introduce an estimator $\hat{E}[R_b, z_c, \vec{\theta}_c]$ defined as

$$\hat{E} = \left[\sum_{a,b} S_f^*(\vec{U}_a, \nu_b) \hat{V}(\vec{U}_a, \nu_b) \right] / \left[\sum_{a,b} 1 \right] \quad (3.13)$$

where $S_f(\vec{U}, \nu)$ is a filter which has been constructed to detect the particular ionized bubble. Here \vec{U}_a and ν_b refer to the different baselines and frequency channels in our observations, and in eq. (3.13) we are to sum over all independent data points (visibilities). Note that the estimator \hat{E} and the filter $S_f(\vec{U}, \nu)$ both depend on $[R_b, z_c, \vec{\theta}_c]$, the

3.3 Formalism for Detecting the Ionized Bubble

parameters of the bubble we wish to detect, but we do not show this explicitly. The values of these parameters will be clear from the context.

We shall be working in the continuum limit where the two sums in eq. (3.13) can be replaced by integrals and we have

$$\hat{E} = \int d^2U \int d\nu \rho_N(\vec{U}, \nu) S_f^*(\vec{U}, \nu) \hat{V}(\vec{U}, \nu) \quad (3.14)$$

$d^2U d\nu \rho_N(\vec{U}, \nu)$ is the fraction of data points *ie.* baselines and frequency channels in the interval $d^2U d\nu$. Note that $\rho_N(\vec{U}, \nu)$ is usually frequency dependent, and it is normalized so that $\int d^2U \int d\nu \rho_N(\vec{U}, \nu) = 1$. We refer to $\rho_N(\vec{U}, \nu)$ as the normalized baseline distribution function.

We now calculate $\langle \hat{E} \rangle$ the expectation value of the estimator. Here the angular brackets denote an average with respect different realizations of the HI fluctuations, noise and foregrounds, all of which have been assumed to be random variables with zero mean. This gives $\langle \hat{V}(\vec{U}, \nu) \rangle = S(\vec{U}, \nu)$ and

$$\langle \hat{E} \rangle = \int d^2U \int d\nu \rho_N(\vec{U}, \nu) S_f^*(\vec{U}, \nu) S(\vec{U}, \nu) \quad (3.15)$$

We next calculate the variance of the estimator which is the sum of the contributions from the noise (NS), the foregrounds(FG) and the HI fluctuations (HF)

$$\begin{aligned} \langle (\Delta \hat{E})^2 \rangle &\equiv \langle (\hat{E} - \langle \hat{E} \rangle)^2 \rangle \\ &= \left\langle (\Delta \hat{E})^2 \right\rangle_{\text{NS}} + \left\langle (\Delta \hat{E})^2 \right\rangle_{\text{FG}} + \left\langle (\Delta \hat{E})^2 \right\rangle_{\text{HF}} . \end{aligned} \quad (3.16)$$

To calculate the noise contribution we go back to eq. (3.13) and use the fact that the

3 Detecting Ionized Bubbles in Redshifted 21 cm Maps

noise in different baselines and frequency channels are uncorrelated. We have

$$\langle (\Delta \hat{E})^2 \rangle_{\text{NS}} = \langle \hat{N}^2 \rangle \left[\sum_{a,b} |S_f(\vec{U}_a, \nu_b)|^2 \right] / \left[\sum_{a,b} 1 \right]^2 \quad (3.17)$$

which in the continuum limit is

$$\begin{aligned} \langle (\Delta \hat{E})^2 \rangle_{\text{NS}} &= \left[\langle \hat{N}^2 \rangle / \sum_{a,b} 1 \right] \\ &\times \int d^2U \int d\nu \rho_N(\vec{U}, \nu) |S_f(\vec{U}, \nu)|^2 \end{aligned} \quad (3.18)$$

The term $\sqrt{\left[\langle \hat{N}^2 \rangle / \sum_{a,b} 1 \right]}$ is the same as σ , the rms. noise in the image (eq. 3.12). We then have

$$\langle (\Delta \hat{E})^2 \rangle_{\text{NS}} = \sigma^2 \int d^2U \int d\nu \rho_N(\vec{U}, \nu) |S_f(\vec{U}, \nu)|^2 . \quad (3.19)$$

For the foreground contribution we have

$$\begin{aligned} \langle (\Delta \hat{E})^2 \rangle_{\text{FG}} &= \int d^2U_1 \int d^2U_2 \int d\nu_1 \int d\nu_2 \\ &\times \rho_N(\vec{U}_1, \nu_1) \rho_N(\vec{U}_2, \nu_2) S_f^*(\vec{U}_1, \nu_1) S_f^*(\vec{U}_2, \nu_2) \\ &\times \langle \hat{F}(\vec{U}_1, \nu_1) \hat{F}(\vec{U}_2, \nu_2) \rangle \end{aligned} \quad (3.20)$$

In the continuum limit we have (details given in Appendix C)

$$\begin{aligned} \langle \hat{F}(\vec{U}_1, \nu_1) \hat{F}(\vec{U}_2, \nu_2) \rangle &= \delta_D^{(2)}(\vec{U}_1 + \vec{U}_2) \left(\frac{\partial B}{\partial T} \right)_{\nu_1} \left(\frac{\partial B}{\partial T} \right)_{\nu_2} \\ &\times C_{2\pi U_1}(\nu_1, \nu_2) \end{aligned} \quad (3.21)$$

which gives the variance of the foreground contribution to be

$$\begin{aligned} \langle (\Delta \hat{E})^2 \rangle_{\text{FG}} &= \int d^2U \int d\nu_1 \int d\nu_2 \left(\frac{\partial B}{\partial T} \right)_{\nu_1} \left(\frac{\partial B}{\partial T} \right)_{\nu_2} \\ &\quad \times \rho_N(\vec{U}, \nu_1) \rho_N(\vec{U}, \nu_2) S_f^*(\vec{U}, \nu_1) S_f(\vec{U}, \nu_2) \\ &\quad \times C_{2\pi U}(\nu_1, \nu_2) \end{aligned} \quad (3.22)$$

We use eq. (3.22) to calculate $\langle (\Delta \hat{E})^2 \rangle_{\text{HF}}$ too, with the difference that we use the power spectrum $C_{2\pi U}(\nu, \nu + \Delta\nu)$ for the HI fluctuation from Datta, Choudhury & Bharadwaj (2007) instead of the foreground contribution.

In an observation it will be possible to detect the presence of an ionized bubble having parameters $[R_b, z_c, \vec{\theta}_c]$ at, say 3-sigma confidence level, if $\langle \hat{E} \rangle \geq 3\sqrt{\langle (\Delta \hat{E})^2 \rangle}$. In such a situation, an observed value E_o can be interpreted as a detection with 99.7% (i.e., 3-sigma) confidence if $E_o > 3\sqrt{\langle (\Delta \hat{E})^2 \rangle}$. The presence of the ionized bubble can be ruled out at the same level of confidence if $\langle \hat{E} \rangle - E_o > 3\sqrt{\langle (\Delta \hat{E})^2 \rangle}$.

3.3.1 Baseline distribution

In this subsection we discuss the normalized baseline distribution function $\rho_N(\vec{U}, \nu)$ which has been introduced earlier. Figure 3.4 shows the baseline coverage for 14 hrs of observation towards a region at declination $\delta = 45^\circ$ with the GMRT at 153MHz. In this figure u and v refer to the Cartesian components of the baselines \vec{U} . Note that the baseline distribution is not exactly circularly symmetric. This asymmetry depends on the source declination which would be different for every observation. We make the simplifying assumption that the baseline distribution is circularly symmetric whereby $\rho_N(\vec{U}, \nu)$ is a function of U . This considerably simplifies our analysis and gives reasonable estimates of what we would expect over a range of declinations. Figure 3.5

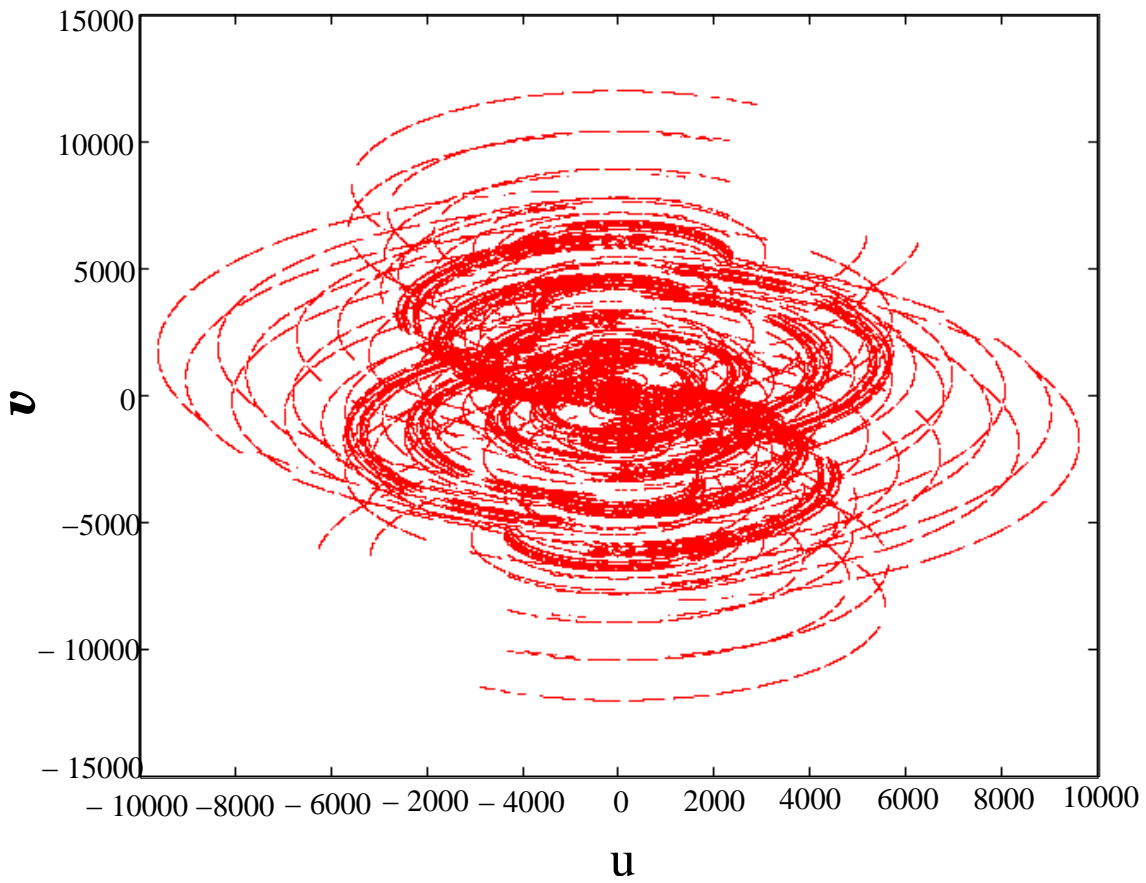


Figure 3.4: This shows the baseline coverage for 14 hrs of GMRT 153 MHz observation at 45° declination.

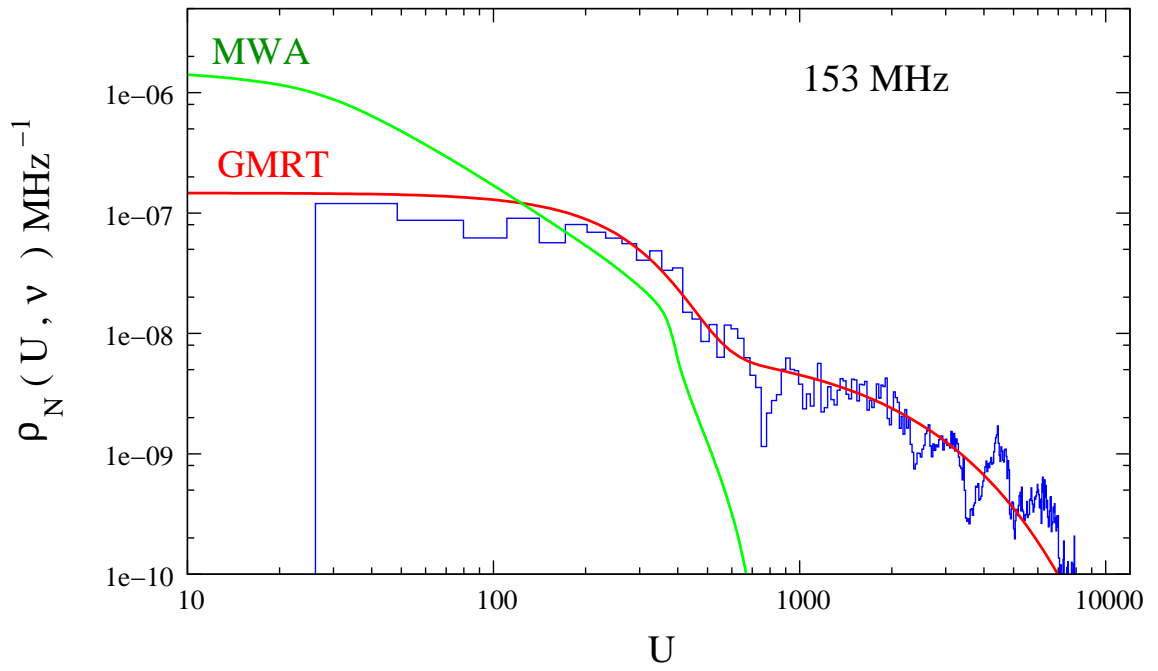


Figure 3.5: This shows the normalized baseline distribution $\rho_N(U, \nu)$ for the GMRT and the MWA at 153 MHz. The wiggly curve shows the actual values for the GMRT observation shown in Figure 3.4 and the smooth curve is the analytic fit.

3 Detecting Ionized Bubbles in Redshifted 21 cm Maps

shows $\rho_N(\vec{U}, \nu)$ for the GMRT determined from the baseline coverage shown in Figure 3.4. We find that this is well described by the sum of a Gaussian and an exponential distribution. The GMRT has a hybrid antenna distribution (Chengalur et al., 2003) with 14 antennas being randomly distributed in a central square approximately $1 \text{ km} \times 1 \text{ km}$ and 16 antennas being distributed along a Y each of whose arms is 14 km long. The Gaussian gives a good fit at small baselines in the central square and the exponential fits the large baselines. Determining the best fit parameters using a least square gives

$$\begin{aligned} \rho_N(\vec{U}, \nu) &= \frac{1}{B} \left(\frac{\lambda}{1 \text{ km}} \right)^2 \left[0.21 \exp \left(-\frac{U^2 \lambda^2}{2a^2} \right) \right. \\ &\quad \left. + 9.70 \times 10^{-3} \exp \left(-\frac{U\lambda - b}{d} \right) \right] \end{aligned} \quad (3.23)$$

where $a = 0.382 \text{ km}$, $b = 0.986 \text{ km}$, $d = 3.07 \text{ km}$ and B is the frequency bandwidth which has a maximum value of 6 MHz.

Following Bowman et al. (2006) we assume that the MWA antennas are distributed within a radius of 0.750 km with the density of antennas decreasing with radius r as $\rho_{ant}(r) \propto r^{-2}$ and with a maximum density of one antenna per 18 m^2 . The normalized baseline distribution is estimated in terms of $\rho_{ant}(r)$ and we have

$$\begin{aligned} \rho_N(\vec{U}, \nu) &= \frac{1}{4.4 \times 10^2 B} \frac{1}{B} \left(\frac{\lambda}{1 \text{ km}} \right)^2 \int_{r=0}^{\infty} d^2r \rho_{ant}(r) \\ &\quad \times \int_{\phi=0}^{2\pi} \rho_{ant}(|\vec{r} - \lambda \vec{U}|) d\phi \end{aligned} \quad (3.24)$$

where the bandwidth B is 32 MHz, $|\vec{r} - \lambda \vec{U}| = (r^2 + U^2 \lambda^2 - 2r \lambda U \cos\phi)^{1/2}$. Note that $\rho_N(\vec{U}, \nu)$ depends on the observed frequency. Figure 3.5 shows the normalized baseline distribution function $\rho_N(\vec{U}, \nu)$ for both the GMRT and the MWA. We see that maximum baseline for the GMRT is $U_{max} \sim 10,000$ whereas $U_{max} \sim 750$ for the MWA. However,

the smaller baselines will be sampled more densely in the MWA as compared to the GMRT.

3.3.2 Filter

It is a major challenge to detect the signal which is expected to be buried in noise and foregrounds both of which are much stronger (Figure 3.3). It would be relatively simple to detect the signal in a situation where there is only noise and no foregrounds. The signal to noise ratio (SNR) is maximum if we use the signal that we wish to detect as the filter (*ie.* $S_f(\vec{U}, \nu) = S(\vec{U}, \nu)$) and the SNR has a value

$$\frac{\langle(\hat{E})\rangle}{\sqrt{\langle(\Delta\hat{E})^2\rangle_{\text{NS}}}} = \frac{1}{\sigma} \left[\int d^2U \int d\nu \rho_N(\vec{U}, \nu) |S(\vec{U}, \nu)|^2 \right]^{0.5} \propto \sqrt{t_{\text{obs}}}. \quad (3.25)$$

The observing time necessary for a $3\text{-}\sigma$ detection (*i.e.*, $\text{SNR} = 3$) would be the least for this filter. Note that the factor $-\pi x_{\text{HI}} \bar{I}_\nu$ outside the signal (eq. 3.4) is almost constant along the line of sight of the ionized bubble. This factor does not affect the value of the quantity $\text{SNR} = \frac{\langle(\hat{E})\rangle}{\sqrt{\langle(\Delta\hat{E})^2\rangle_{\text{NS}}}}$. One can drop this term from the filter $S_f(\vec{U}, \nu)$ without losing the effectiveness of the method. The difficulty with using this filter is that the foreground contribution to $\sqrt{\langle(\Delta\hat{E})^2\rangle}$ is orders of magnitude more than $\langle(\hat{E})\rangle$. The foregrounds, unlike the HI signal, are all expected to have a smooth frequency dependence and one requires filters which incorporate this fact so as to reduce the foreground contribution. We consider two different filters which reduce the foreground contribution, but it occurs at the expense of reducing the SNR, and t_{obs} would be more than that predicted by eq. (3.25).

The first filter (Filter I) subtracts out any frequency independent component from

3 Detecting Ionized Bubbles in Redshifted 21 cm Maps

the frequency range $\nu_c - B'/2$ to $\nu_c + B'/2$ with $B' \leq B$ ie.

$$S_f(\vec{U}, \nu) = \left(\frac{\lambda_c}{\lambda}\right)^2 \left[S(\vec{U}, \nu) - \frac{\Theta(1 - 2|\nu - \nu_c|/B')}{B'} \int_{\nu_c - B'/2}^{\nu_c + B'/2} S(\vec{U}, \nu') d\nu' \right]. \quad (3.26)$$

This filter has the advantage that it does not require any prior knowledge about the foregrounds except that they have a continuous spectrum. It has the drawback that there will be contributions from the residual foregrounds as all the foregrounds are expected to have a power law spectral dependence and not a constant. A larger value of B' causes the SNR to increase, and in the limit $B' \rightarrow \infty$ the SNR approaches the value given in eq. (3.25). Unfortunately the residues in the foregrounds also increase with B' . We use $B' = 4\Delta\nu_b$ provided it is less than B , and $B' = B$ otherwise.

The frequency dependence of the total foreground contribution can be expanded in Taylor series. Retaining terms only up to the first order we have

$$C_l(\nu_1, \nu_2) = C_l(\nu_c, \nu_c) [1 - (\Delta\nu_1 + \Delta\nu_2) \alpha_{eff}/\nu_c] \quad (3.27)$$

where $\Delta\nu = \nu - \nu_c$ and $\alpha_{eff} = \frac{\sum_i \alpha^i A^i (1000/l)^{\beta_i}}{\sum_i A^i (1000/l)^{\beta_i}}$ is the effective spectral index, here i refers to the different foreground components. Note that α_{eff} is l dependent. The second filter that we consider (Filter II) allows for a linear frequency dependence of the foregrounds and we have

$$S_f(\vec{U}, \nu) = (1 + \alpha_{eff} \Delta\nu/\nu_c) \left(\frac{\lambda_c}{\lambda}\right)^2 \left[S(\vec{U}, \nu) - \frac{\Theta(1 - 2|\nu - \nu_c|/B')}{B'} \int_{\nu_c - B'/2}^{\nu_c + B'/2} S(\vec{U}, \nu') d\nu' \right].$$

(3.28)

Note that for both the filters we include an extra factor $(\lambda_c/\lambda)^2$. This is introduced with the purpose of canceling out the λ^2 dependence of the normalized baseline distribution function $\rho_N(\vec{U}, \nu)$ and this substantially reduces the foreground contribution.

3.4 Results and Discussions

We first consider the most optimistic situation where the bubble is at the center of the field of view and the filter center is exactly matched with the bubble center. The size distribution of HII regions are quite uncertain, and would depend on the reionization history and the distribution of ionizing sources. However, there are some indications in the literature on what could be the typical size of HII regions. For example, Wyithe, Loeb & Barnes (2005) deduce from proximity zone effects that $R_b \approx 35$ Mpc at $z \approx 6$, which should be considered as a lower limit. On the other hand, Furlanetto, McQuinn & Hernquist (2006) (Figure 1(a)) infer that the characteristic bubble size $R_b > 10$ Mpc at $z = 8$ if the ionized fraction $x_i > 0.75$ ($R_b \sim 50$ Mpc if $x_i \sim 0.9$). Theoretical models which match a variety of observations (Choudhury & Ferrara, 2007) imply that x_i could be as high as 90% at $z \sim 8$, which would mean bubble sizes of $\sim 40 - 50$ Mpc. To allow for the large variety of possibilities, we have presented results for a wide range of R_b values from 2 Mpc to 50 Mpc. We restrict our analysis to a situation where the IGM outside the bubble is completely neutral ($x_{\text{HI}} = 1$). The signal would fall proportional to x_{HI} if the IGM outside the bubble were partially ionized ($x_{\text{HI}} < 1$). The expected signal $\langle \hat{E} \rangle$ and 3-sigma fluctuation $3 \times \sqrt{\langle (\Delta \hat{E})^2 \rangle}$ from each of the different components discussed in Sections 2 and 3 as a function of bubble size R_b are shown in Figures 3.6 and 3.7. Both the figures show exactly the same quantities, the

3 Detecting Ionized Bubbles in Redshifted 21 cm Maps

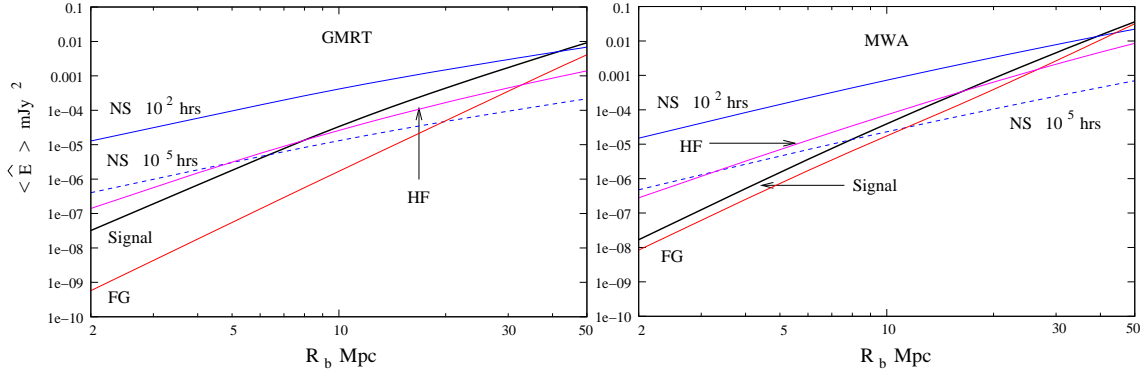


Figure 3.6: The signal quantified through the expectation value of the estimator $\langle \hat{E} \rangle$ for Filter I. The other components (NS - Noise, FG - Foregrounds, HF - HI Fluctuations) are quantified through their contribution to the 3-sigma fluctuation $3 \times \sqrt{\langle (\Delta \hat{E})^2 \rangle}$.

only difference being that they refer to Filter I and Filter II respectively. A detection is possible only in situations where $\langle \hat{E} \rangle > 3 \times \sqrt{\langle (\Delta \hat{E})^2 \rangle}$, the *rhs.* now refers to the total contribution to the estimator variance from all the components.

The signal is expected to scale as R_b^3 and the noise as $R_b^{3/2}$ in a situation where the baseline distribution is uniform *ie.* $\rho_N(\vec{U}, \nu)$ is independent of U . This holds at $U < 300$ for the GMRT (Figure 3.5), and the expected scaling is seen for $R_b \geq 20$ Mpc. For smaller bubbles the signal extends to larger baselines where $\rho_N(U, \nu)$ falls sharply, and the signal and the noise both have a steeper R_b dependence. The MWA baseline distribution is flat for only a small U range (Figure 3.5) beyond which it drops. In this case the signal and noise are found to scale as R_b^4 and R_b^2 respectively. Note that the maximum baseline at MWA is $U = 750$, and hence a considerable amount of the signal is lost for $R_b < 10$ Mpc.

At both the GMRT and the MWA, for 100 hrs of observation, the noise is larger than the signal for bubble size $R_b \leq 40$ Mpc. At the other extreme, for an integration time of 10^5 hrs the noise is below the signal for $R_b > 6$ Mpc for the GMRT and $R_b > 8$ Mpc for the MWA. The foreground contribution turns out to be smaller than the signal for

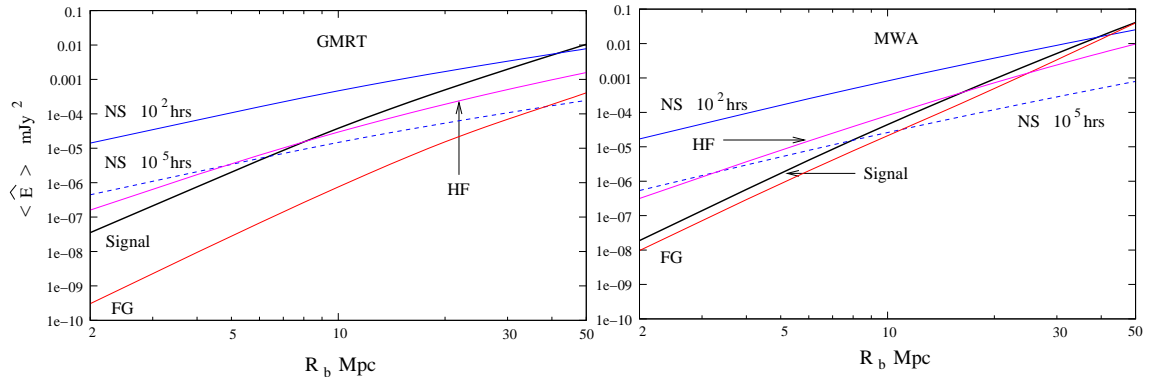


Figure 3.7: Same as Figure 3.6 except that Filter II is used instead of Filter I.

the entire range of bubble sizes that we have considered, thus justifying our choice of filters. Note that Filter II is more efficient in foreground subtraction, but it requires prior knowledge about the frequency dependence. For both the filters the foreground removal is more effective at the GMRT than the MWA because of the frequency dependence of $\rho_N(\vec{U}, \nu)$. The assumption that this is proportional to λ^2 is valid only when $\rho(\vec{U}, \nu)$ is independent of U , which, as we have discussed, is true for a large U range at the GMRT. The λ dependence is much more complicated at the MWA, but we have not considered such details here as the foreground contribution is anyway smaller than the signal. It should also be noted that the foreground contribution increases at small baselines (eq. 3.10), and is very sensitive to the smallest value of U which we set at $U = 20$ for our calculations. Here it must be noted that our results are valid only under the assumption that the foregrounds have a smooth frequency dependence. A slight deviation from this and the signal will be swamped by the foregrounds. Also note that this filtering method is effective only for the detection of the bubbles and not for the statistical HI fluctuations signal.

The contribution from the HI fluctuations impose a lower limit on the size of the bubble which can be detected. However long be the observing time, it will not be possible to detect bubbles of size $R_b < 8 \text{ Mpc}$ using the GMRT and size $R_b < 16 \text{ Mpc}$

3 Detecting Ionized Bubbles in Redshifted 21 cm Maps

using the MWA. The HI fluctuation contribution increases at small baselines. The problem is particularly severe at MWA because of the dense sampling of the small baselines and the very large field of view. We note that the MWA is being designed with the detection of the statistical HI fluctuation signal in mind, and hence it is not surprising that this contribution is quite large. For both telescopes it may be possible to reduce this component by cutting off the filter at small baselines. We have not explored this possibility in this work because the enormous observing times required to detect such small bubbles makes it unfeasible with the GMRT or MWA.

Figure 3.8 shows the observation time that would be required to detect bubbles of different sizes using Filter I for GMRT and the MWA. Note that the observing time shown here refers to a 3σ detection which is possibly adequate for targeted searches centered on observed quasar position. A more stringent detection criteria at the 5σ level would be appropriate for a blind search. The observing time would go up by a factor of 3 for a 5σ detection. The observing time is similar for Filter II and hence we do not show this separately. In calculating the observing time we have only taken into account the noise contribution as the other contributions do not change with time. The value of R_b below which a detection is not possible due to the HI fluctuations is shown by vertical lines for both telescopes. We see that with 100 hrs of observation both the telescopes will be able to detect bubbles with $R_b > 40$ Mpc while bubbles with $R_b > 22$ Mpc can be detected with 1000 hrs of observation.

The possibility of detecting a bubble is less when the bubble centre does not coincide with the centre of the field of view. In fact, the SNR falls as $e^{-\theta_c^2/\theta_0^2}$ if the bubble center is shifted away by θ_c from the center of the field of view and the filter is also shifted so that its center coincides with that of the bubble. There will be a corresponding increase $t_{obs} \propto e^{2\theta_c^2/\theta_0^2}$ in the observing time required to detect the bubble. It will be possible to detect bubbles only if they are located near the center of the field of view ($\theta_c \ll \theta_0$), and

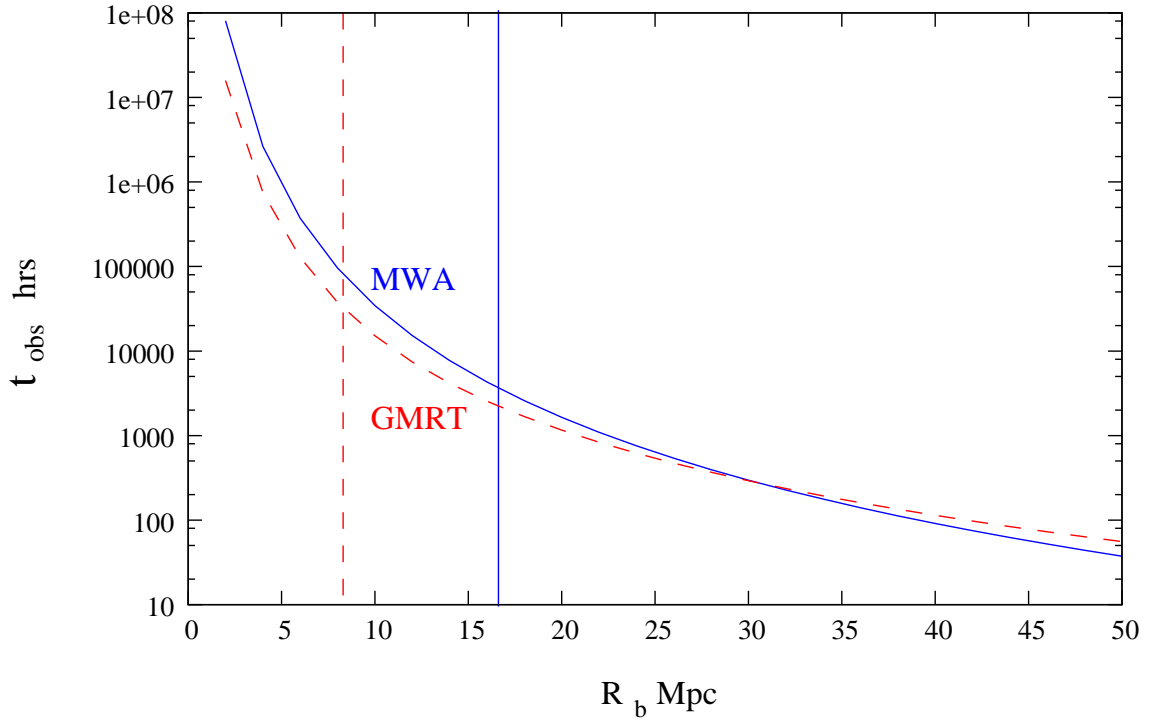


Figure 3.8: The observing time t_{obs} that would be required for a 3σ detection of a bubble of radius R_b provided it is at the center of the field of view. The vertical lines shows the lower limit (due to HI fluctuations) where a detection will be possible ($R_b = 8$ Mpc for GMRT and $R_b = 16$ Mpc for MWA).

3 Detecting Ionized Bubbles in Redshifted 21 cm Maps

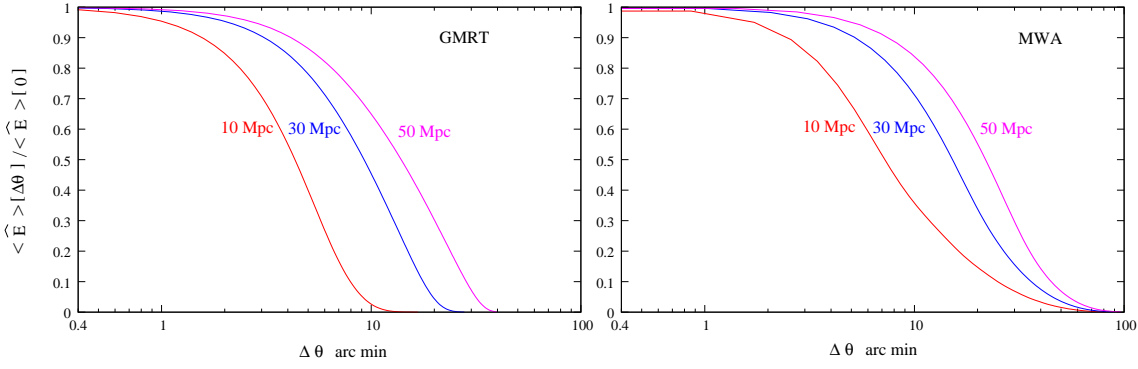


Figure 3.9: The Overlap between the signal and the filter when there is a mismatch $\Delta\theta$ between the centers of the bubble and the filter for GMRT (left) and MWA (right). The results are shown for different bubble sizes.

the required observing time increases rapidly with θ_c for off-centered bubbles.

When searching for bubbles in a particular observation it will be necessary to consider filters corresponding to all possible value of R_b , ν_c and $\vec{\theta}_c$. A possible strategy would be to search at a discrete set of values in the range of R_b , ν_c and $\vec{\theta}_c$ values where a detection is feasible. The crucial issue here would be the choice of the sampling density so that we do not miss out an ionized bubble whose parameters do not exactly coincide with any of the values in the discrete set and lie somewhere in between. To illustrate this we discuss the considerations for choosing an optimal value of $\Delta\theta_c$ the sampling interval for $\vec{\theta}_c$. We use $\langle \hat{E} \rangle[\Delta\theta]$ to denote the expectation value of the estimator when there is a mismatch $\Delta\theta$ between the centers of the bubble and the filter. The ratio $\text{Overlap} = \langle \hat{E} \rangle[\Delta\theta] / \langle \hat{E} \rangle[0]$, shown in Figure 3.9 for GMRT (left panel) and MWA (right panel), quantifies the overlap between the signal and the filter as $\Delta\theta$ is varied. We see that the choice of $\Delta\theta$ would depend on the size of the bubble we are trying to detect and it would be smaller for the GMRT as compared to the MWA. Permitting the Overlap to drop to 0.9 at the middle of the sampling interval, we find that it is $8'$ at the GMRT and $20'$ at the MWA for $R_b = 50$ Mpc.

The MWA is yet to be constructed, and it may be possible that an antennae distribu-

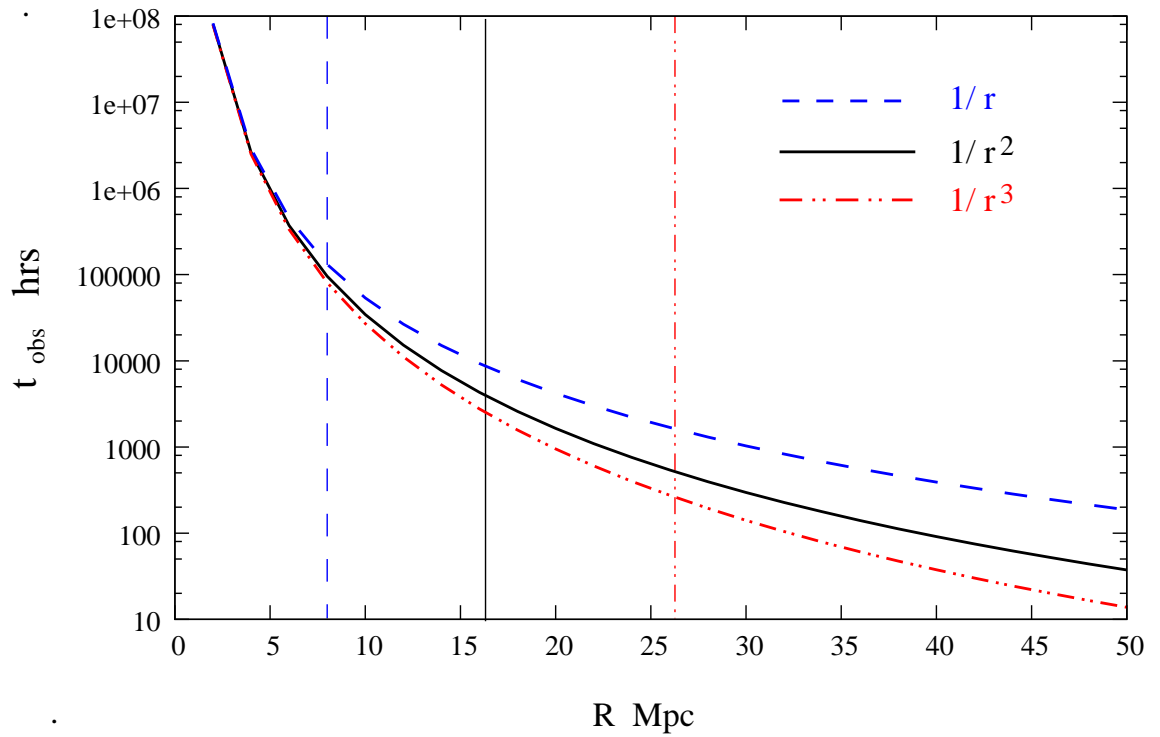


Figure 3.10: Same as the Figure 3.8 considering three different antenna distributions $\rho_{\text{ant}}(r) \propto 1/r, 1/r^2, 1/r^3$ for the MWA.

3 Detecting Ionized Bubbles in Redshifted 21 cm Maps

tion different from $\rho_{ant}(r) \propto 1/r^2$, may improve the prospects of detecting HII bubbles. We have tried out $\rho_{ant}(r) \propto 1/r$ and $1/r^3$ for which the results are shown in Figure 3.10. We find that the required integration time falls considerably for the $1/r^3$ distribution whereas the opposite occurs for $1/r$. For example, for $R_b = 50$ Mpc the integration time increases by 5 times for $1/r$ and decreases by 3 times for $1/r^3$ as compared to $1/r^2$. Based on this we expect the integration time to come down if the antenna distribution is made steeper, but this occurs at the expense of increasing the HI fluctuations and the foregrounds. We note that for the $1/r^3$ distribution the foreground contribution is more than the signal, but it may be possible to overcome this by modifying the filter. The increase in the HI fluctuations is inevitable, and it restricts the smallest bubble that can be detected to $R = 26$ Mpc for $1/r^3$. In summary, the $1/r^2$ distribution appears to be a good compromise between reducing the integration time and increasing the HI fluctuations and foregrounds.

Finally we examine some of the assumptions made in this work. First, the Fourier relation between the specific intensity and the visibilities (eq. 3.1) will be valid only near the center of the field of view and full three dimensional wide-field imaging is needed away from the center. As the feasibility of detecting a bubble away from the center falls rapidly, we do not expect the wide-field effects to be very important. Further, these effects are most significant at large baselines whereas most of the signal from ionized bubbles is in the small baselines.

Inhomogeneities in the IGM will affect the propagation of ionization fronts, and the ionized bubbles are not expected to be exactly spherical (Wyithe, Loeb & Barnes, 2005). This will cause a mismatch between the signal and the filter which in turn will degrade the SNR. In addition to this, in future we plan to address a variety of other issues like considering different observing frequencies and making predictions for the other upcoming telescopes.

Terrestrial signals from television, FM radio, satellites, mobile communication etc., collectively referred to as RFI, fall in the same frequency band as the redshifted 21cm signal from the reionization epoch. These are expected to be much stronger than the expected 21cm signal, and it is necessary to quantify and characterize the RFI. Recently Bowman et al. (2007) have characterized the RFI for the MWA site on the frequency range 80 to 300MHz. They find an excellent RFI environment except for a few channels which are dominated by satellite communication signal. The impact of RFI on detecting ionized bubbles is an important issue which we plan to address in future.

The effect of polarization leakage is another issue we postpone for future work. This could cause polarization structures on the sky to appear as frequency dependent ripples in the foregrounds intensity . This could be particularly severe for the MWA.

3 Detecting Ionized Bubbles in Redshifted 21 cm Maps

4 Simulating Matched Filter Search for Ionized Bubbles*

4.1 Introduction

In the previous Chapter we present an analytic framework for predicting the expected value and the standard deviation σ of the matched filter estimator for the detection of a spherical ionized bubble of comoving radius R_b . We identify three different contributions to σ , namely foregrounds, system noise and the fluctuations in the HI outside the bubble that we are trying to detect. Our analysis shows that the matched filter effectively removes the foreground contribution so that it falls below the signal. Considering the system noise for the GMRT and the MWA we find that a 3σ detection will be possible for

* *This Chapter is adapted from the paper “Simulating the impact of HI fluctuations on matched filter search for ionized bubbles in redshifted 21 cm maps” by Datta et al. (2008).*

4 *Simulating Matched Filter Search for Ionized Bubbles*

a bubble of comoving radius $R_b \geq 40$ Mpc in 100 hrs of observation and $R_b \geq 22$ Mpc in 1000 hrs of observation for both the instruments. The HI fluctuations, we find, impose a fundamental restriction on bubble detection. Under the assumption that the HI outside the ionized bubble traces the dark matter we find that it is not possible to detect bubble of size $R_b \leq 8$ Mpc and $R_b \leq 16$ Mpc at the GMRT and MWA respectively. Note that the matched filter technique is valid for both, a targeted search around QSOs as well as for a blind search in a random direction.

Here we validate the visibility based matched filter technique introduced in the previous Chapter through simulations of bubble detection. Our simulations are capable of handling interferometric arrays with widely different configurations like the GMRT and the MWA, the two instruments that we consider here. As mentioned earlier, the fluctuations in the HI outside the target bubble impose a fundamental restriction for bubble detection. The analytic approach of the Chapter 3 assumes that the HI outside the bubble traces the dark matter. In this Chapter we carry out simulations that incorporate this assumption and use these to assess the impact of HI fluctuations for bubble detection. We also use the simulations to determine the accuracy to which the GMRT and the MWA will be able to determine the size and the position of an ionized bubble, and test if this is limited due to the presence of HI fluctuations. In a real situation a typical FoV is expected to contain several ionized patches besides the one that we are trying to detect. We use simulations to assess the impact of HI fluctuations for bubble detection in patchy reionization scenarios.

The outline of the Chapter is as follows. Section 4.2 presents a brief description of how we simulate 21-cm maps for three different scenarios of the HI distribution, one where the HI traces the dark matter and two with patchy reionization. Subsections 4.2.1 and 4.2.2 respectively discuss how the simulated maps are converted into visibilities and how the matched filter analysis is simulated. We present our results in Section 4.3. Subsections

4.3.1, 4.3.2 and 4.3.3 present results for bubble detectability, size determination and position determination under the assumption that the HI outside the bubble traces the dark matter. Section 4.3.4 presents results for bubble detectability in patchy reionization scenarios. We discuss redshift dependence of bubble detection in Section 4.4 and present our summary in Section 4.5.

For the GMRT we have used the telescope parameters from their website, while for the MWA we use the telescope parameters from Bowman et al. (2006). The cosmological parameters for a flat ($k = 0$) Λ CDM model used throughout this paper are $\Omega_m = 0.3$, $\Omega_b h^2 = 0.022$, $n_s = 1.$, $h = 0.74$, $\sigma_8 = 1.$

4.2 Method of Simulation

We have simulated the detection of the HI signal of an ionized bubble whose center is at redshift $z_c = 6$ which corresponds to $\nu_c = 203$ MHz. The choice of z value is guided by the fact that we expect large ionized regions towards the end of reionization $z \gtrsim 6$ (Wyithe & Loeb, 2004; Furlanetto, McQuinn & Hernquist, 2006). Our aim here is to validate the analytic calculations of the Chapter 3 and hence the exact value of z is not very important.

We consider four scenarios of reionization for bubble detection. In the first three scenarios there is a spherical ionized bubble, the one that we are trying to detect, at the center of the FoV. This bubble has comoving radius R_b and is embedded in HI that traces the dark matter. In the first scenario there is a single bubble in the field of view. We refer to this as the SB scenario. In this scenario the HI fraction x_{HI} is assumed to be uniform outside the bubble. The uncertainty due to the HI fluctuations is expected to be lowest in this scenario because of the absence of patchiness. This is the most optimistic scenario for bubble detection.

4 *Simulating Matched Filter Search for Ionized Bubbles*

In the next two scenarios, we attempt to quantify the effect of patchy reionization (PR) outside the bubble that we are trying to detect by introducing many other, possibly overlapping, bubbles in the FoV. Unfortunately, there is no obvious way to fix the sizes of these bubbles from any theoretical models as they depend crucially on the nature of reionization sources and other physical factors. In scenario PR1, we assume that the large HII regions which we are trying to detect are surrounded by many small ionized regions whose sizes are fixed by the following procedure: we assume the globally averaged neutral fraction x_{HI} to be ~ 0.5 ; the reason for this choice is that the effects of patchiness would be most prominent when typically half of the IGM is ionized. Given the value of x_{HI} , we try to obtain a reasonable estimate of the size of the background bubbles from available models. For example, semi-numeric simulations of patchy reionization (Mesinger & Furlanetto, 2007) predict that the bubble size distribution peaks around 5 Mpc when $x_{\text{HI}} = 0.61$ (see their Fig 6). We thus choose the spherical background bubbles to have radii 6 Mpc and compute the number of background bubbles by demanding that the resulting neutral fraction is 0.5. The bubble centres are chosen such that they trace the underlying dark matter distribution. At the end, the value of x_{HI} turns out to be slightly higher 0.62 because of overlap of the bubbles. Note that because of these overlaps, the shapes of the resulting ionized regions would not always be perfectly spherical. In this scenario, we have essentially attempted to capture a situation where there are many small, possibly overlapping ionized regions produced by galaxies and a few large ionized regions (like the one that we are trying to detect) produced by QSOs.

Since the choice of the background bubble size is not robust by any means, we consider a different scenario PR2 where these bubbles have the same comoving radius R_b as the bubble that we are trying to detect. The centers of these extra bubbles trace the dark matter distribution as in PR1. The number of bubbles is fixed by the globally

averaged x_{HI} which we take to be 0.62 same as in PR1. The PR2 scenario represents a situation where we predominantly have large ionized regions produced either by rare luminous sources or through the overlap of several small ionized regions in the later stages of reionization.

A particle-mesh (PM) N-body code was used to simulate the dark matter distribution. In the Chapter 3 we show that the HI signal of the ionized bubble is largely concentrated at small baselines or large angular scales, thus a very high spatial resolution is not required. We have used a grid spacing of 2 Mpc for the simulations. This is adequate for bubbles in the range $4 \leq R_b \leq 50$ Mpc that we consider. The simulations use 256^3 particles on a 256^3 mesh. For the GMRT a single N-body simulation was cut into 8 equal cubes of size 256 Mpc on each side. Considering that each cube may be viewed along three different directions, we have a total of 24 different realization of the dark matter distribution. Each cube corresponds to 18 MHz in frequency and $\sim 2^\circ$ in angle which is comparable to the GMRT FoV which has FWHM= 1.7° at 203MHz. The MWA FoV is much larger (FWHM= 13°). Here eight independent N-body simulations were used. Viewing these along three different directions gives twenty four different realizations of the dark matter distribution. Limited computer memory restricts the simulation size and the angular extent ($\sim 4^\circ$) is considerably smaller than the MWA FoV. We do not expect this to affect the signal but the contribution from the HI fluctuations outside the bubble is possibly underestimated for the MWA.

The dark matter density contrast δ was used to calculate the redshifted 21 – cm specific intensity $I_\nu = \bar{I}_\nu x_{\text{HI}}(1 + \delta)$ for each grid point of our simulation. Here $\bar{I}_\nu = 2.5 \times 10^2 \frac{\text{Jy}}{\text{sr}} \left(\frac{\Omega_b h^2}{0.02} \right) \left(\frac{0.7}{h} \right) \left(\frac{H_0}{H(z)} \right)$ and x_{HI} the hydrogen neutral fraction is 0 inside the ionized bubbles and 1 outside. The simulated boxes are transformed to frequency and sky coordinate. Figure 4.1 shows the HI image on a slice through the center of the bubble of radius $R_b = 20$ Mpc. The mean neutral fraction \bar{x}_{HI} is ~ 1 in the SB scenario,

4 Simulating Matched Filter Search for Ionized Bubbles

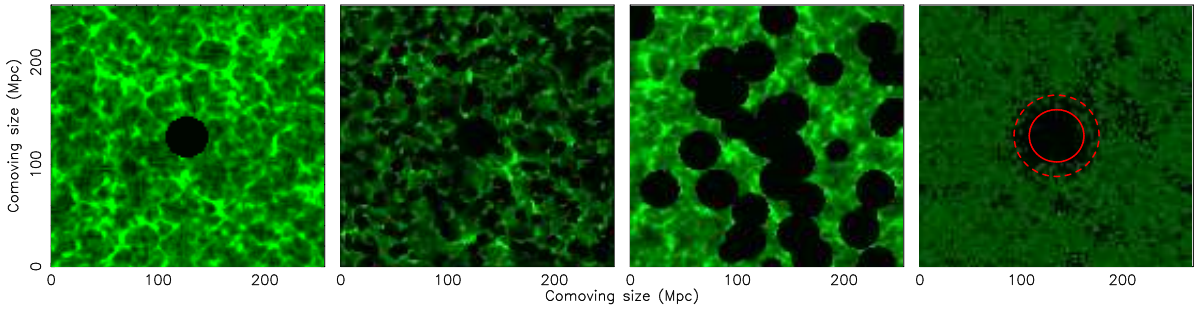


Figure 4.1: This shows HI images on slices through the center of the bubble for the four different scenarios SB, PR1, PR2 and SM (from left to right). In first three panels the central, circular dark region of radius $R_b = 20$ Mpc shows the HII bubble that we are trying to detect. The HI outside this bubble traces the dark matter distribution. In the SB scenario (left) the hydrogen neutral fraction is $x_{\text{HI}} = 1$ outside the bubble. In the PR1 scenario (2nd from left) the extra bubbles are all of a fixed comoving radius 6 Mpc. In the PR2 scenario (3rd from left) the extra bubbles have the same comoving radius as the bubble that we are trying to detect. In both the PR1 and PR2 reionization scenarios the centers of the extra bubbles trace the dark matter distribution and $x_{\text{HI}} = 0.62$. In the SM scenario (right) the central region up to radius 27 Mpc is fully ionized (marked with solid circle) and beyond that region up to radius 42 Mpc the region is partially filled with HI patches (dashed circle). The mean neutral fraction is $x_{\text{HI}} = 0.5$. These simulations are all for the GMRT.

while it is ~ 0.62 for the two PR simulations shown here.

The three scenarios discussed above consider only spherical bubbles, and the only departures from sphericity arise from bubble overlap. It is important to assess how well our bubble detection technique works for non-spherical bubbles, which we do using ionization maps produced by the semi-numeric (SM) approach. In particular, we use maps obtained by the method of Choudhury, Haehnelt & Regan (2008). Essentially, these maps are produced by incorporating an excursion-set based technique for identifying ionized regions given the density distribution and the ionizing sources (Zahn et al., 2007; Mesinger & Furlanetto, 2007; Geil & Wyithe, 2008). In addition, the method of Choudhury, Haehnelt & Regan (2008) incorporate inhomogeneous recombination and self-shielding of high-density regions so that it is consistent with the “photons-starved”

reionization scenario implied by the Ly α forest data (Bolton & Haehnelt, 2007; Choudhury, Ferrara 2008). We use a simulation box of size 270 Mpc with 2000^3 particles which can resolve collapsed halos as small as $\approx 10^9 M_\odot$. The ionization maps are generated at a much lower resolution with a grid size of 2.7 Mpc. The box corresponds to 19 **MHz** in frequency and $\sim 2^\circ$ in angle comparable to the GMRT FoV. We have assigned luminosities to the collapsed halos such that the mean neutral fraction $x_{\text{HI}} = 0.5$. The most massive halo (mass $\sim 10^{13} M_\odot$) identified in the box is made to coincide with the box centre and we assume that it hosts a luminous QSO; its luminosity and age are chosen such that it would produce a spherical HII region of comoving size ≈ 27 Mpc in a completely homogeneous neutral medium [see, e.g., equation (8) of Geil & Wyithe (2008)]. However, the actual ionized region is far from spherical both because of the surrounding bubbles from other halos and also because of inhomogeneous recombination. We find visually from the maps (see the rightmost panel of Figure 4.1) that the HII region is fully ionized up to radius ≈ 27 Mpc. Beyond that the region is partially filled with neutral patches. This patchy ionized region extends up to radius ~ 42 Mpc and then merges with the average IGM. The fully ionized region and the region with HI patches are marked with two circles. We use this box for GMRT as three independent realizations viewing the box along three different directions. For the MWA we need a much larger simulation box which requires substantially more computing power, beyond the resources available to us at present. Hence we do not consider the MWA for this scenario.

4.2.1 Simulating visibilities

The quantity measured in radio-interferometric observations is the visibility $V(\vec{U}, \nu)$ which is related to the specific intensity pattern on the sky $I_\nu(\vec{\theta})$ as

$$V(\vec{U}, \nu) = \int d^2\theta A(\vec{\theta}) I_\nu(\vec{\theta}) e^{2\pi i \vec{\theta} \cdot \vec{U}} \quad (4.1)$$

Here the baseline $\vec{U} = \vec{d}/\lambda$ denotes the antenna separation \vec{d} projected in the plane perpendicular to the line of sight in units of the observing wavelength λ , $\vec{\theta}$ is a two dimensional vector in the plane of the sky with origin at the center of the FoV, and $A(\vec{\theta})$ is the beam pattern of the individual antenna. For the GMRT this can be well approximated by Gaussian $A(\vec{\theta}) = e^{-\theta^2/\theta_0^2}$ where $\theta_0 \approx 0.6 \theta_{\text{FWHM}}$ and we use the values 1.7° for θ_0 at 203 MHz corresponding to the redshift $z = 6$ for the GMRT. The MWA beam pattern is expected to be quite complicated, and depends on the pointing angle relative to the zenith (Bowman et al., 2007). Our analysis largely deals with the beam pattern within 2° of the pointing angle where it is reasonable to approximate the beam as being circularly symmetric (Figures 3 and 5 of Bowman et al. 2007). We approximate the MWA antenna beam pattern as a Gaussian.

We consider 128 frequency channels across 18MHz bandwidth. The image $I_\nu(\theta)$ at each channel is multiplied with the telescope beam pattern $A(\vec{\theta}, \nu)$. The discrete Fourier transform (DFT) of the product $I_\nu(\theta) A(\vec{\theta}, \nu)$ gives the complex visibilities $\hat{V}(\vec{U}, \nu)$. The GMRT simulations have baselines in the range $30.5 \leq U \leq 3900$ which is adequate to capture the HI signal from ionized bubbles which is expected to be confined to small baselines $U < 1000$.

The visibility recorded in radio-interferometric observations is actually a combination

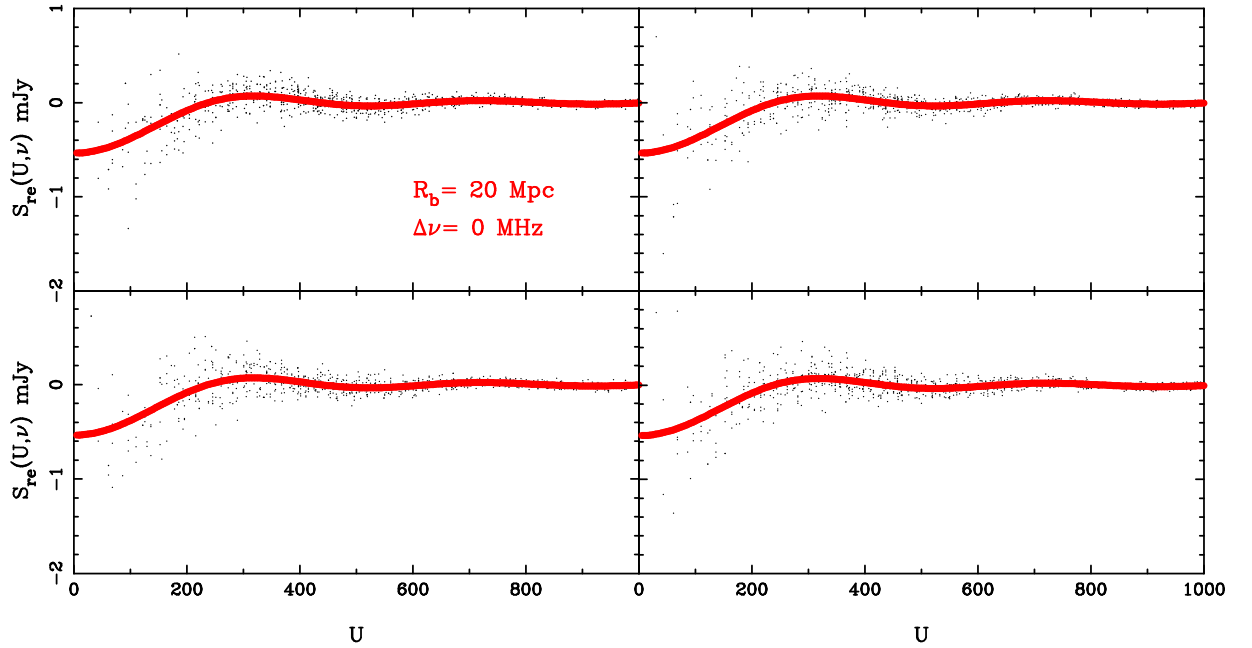


Figure 4.2: This shows the visibility signal (real part) from a frequency slice through the center of a spherical ionized bubble of comoving radius 20 Mpc embedded in HI. The solid curves show the expected signal assuming that the bubble is embedded in uniformly distributed HI. The data points show the visibilities for a few randomly chosen baselines from our simulation of the SB scenario. The difference between the data points and the solid curve is due to the fluctuations in the HI outside the bubble. Each panel corresponds to a different realization of the simulation.

4 Simulating Matched Filter Search for Ionized Bubbles

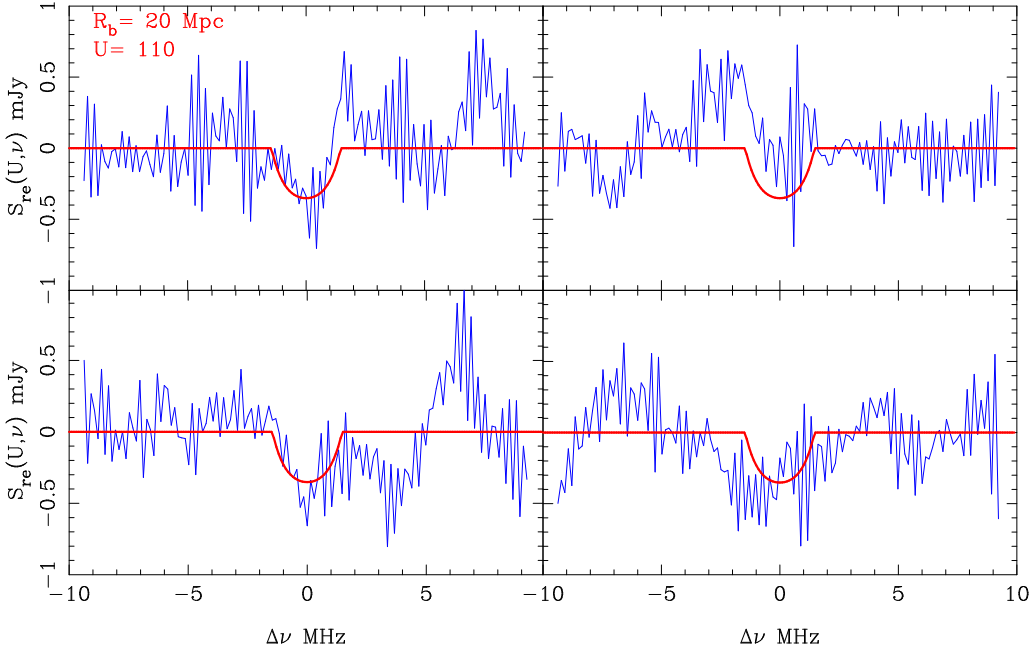


Figure 4.3: Same as the previous figure except that U is fixed at 110 while the frequency varies, and $\Delta\nu = \nu - \nu_c$.

of several contributions

$$V(\vec{U}, \nu) = S(\vec{U}, \nu) + HF(\vec{U}, \nu) + N(\vec{U}, \nu) + F(\vec{U}, \nu). \quad (4.2)$$

where $S(\vec{U}, \nu)$ is the HI signal that we are interested in, $HF(\vec{U}, \nu)$ is contribution from the fluctuating HI outside the bubble that we are trying to detect, $N(\vec{U}, \nu)$ is the system noise which is inherent to the measurement and $F(\vec{U}, \nu)$ is the contribution from other astrophysical sources referred to as the foregrounds. The signal $S(\vec{U}, \nu)$ from an ionized bubble of comoving radius R_b embedded in an uniform HI distribution can be analytically calculated (Chapter 3). The solid curve in Figures 4.2 and 4.3 show the expected signal for $R_b = 20$ Mpc. The U extent, frequency extent and peak value of the signal scale as R_b^{-1} , R_b and R_b^2 respectively for other values of R_b . Note that $S(\vec{U}, \nu)$ is real when the bubble is at the center of the FoV.

The data points shown in Figures 4.2 and 4.3 are the real part of a few randomly

chosen visibilities determined from the simulation of a $R_b = 20$ Mpc bubble in the SB scenario. The deviations from the analytic predictions are due to the HI fluctuations $HF(\vec{U}, \nu)$ *ie.* in the SB scenario the HI outside the bubble traces the dark matter fluctuations. Notice that these fluctuations are often so prominent that the signal cannot be made out. We expect even larger fluctuations in the other three scenarios which incorporate patchiness of reionization.

The system noise contribution $N(\vec{U}, \nu)$ in each baseline and frequency channel is expected to be an independent Gaussian random variable with zero mean ($\langle \hat{N} \rangle = 0$) and variance $\sqrt{\langle \hat{N}^2 \rangle}$ is independent of \vec{U} and ν_c . We use (Chapter 3)

$$\sqrt{\langle \hat{N}^2 \rangle} = C^x \left(\frac{\Delta \nu_c}{1\text{MHz}} \right)^{-1/2} \left(\frac{\Delta t}{1\text{sec}} \right)^{-1/2} \quad (4.3)$$

where C^x has values 0.53Jy and 54.21Jy for the GMRT and the MWA respectively (Chapter 3).

The contribution from astrophysical foregrounds $F(\vec{U}, \nu)$ is expected to be several order of magnitude stronger than the HI signal. The foregrounds are predicted to have a featureless, continuum spectra whereas the signal is expected to have a dip at ν_c (Figure 4.3). This difference holds the promise of allowing us to separate the signal from the foregrounds.

4.2.2 Simulating signal detection

The signal component $S(\vec{U}, \nu)$ in the observed visibilities $V(\vec{U}, \nu)$ is expected to be buried deep in other contributions many of which are orders of magnitude larger. Detecting this is a big challenge. For optimal signal detection we consider the estimator (Chapter

4 Simulating Matched Filter Search for Ionized Bubbles

3)

$$\hat{E} = \sum_{a,b} S_f^*(\vec{U}_a, \nu_b) \hat{V}(\vec{U}_a, \nu_b) \quad (4.4)$$

where $S_f(\vec{U}, \nu)$ is a filter which has been constructed to detect a particular ionized bubble, $\hat{V}(\vec{U}_a, \nu_b)$ refer to the observed visibilities and \vec{U}_a and ν_b refer to the different baselines and frequency channels in the observation. The filter $S_f(\vec{U}, \nu)$ depends on $[R_f, z_c, \vec{\theta}_c]$ the comoving radius, redshift and angular position of the bubble that we are trying to detect. We do not show this explicitly, the values of these parameters will be clear from the context.

The baselines obtained using DFT in our simulations are uniformly distributed on a plane. In real observations, the baselines will have a complicated distribution depending on the antenna layout and direction of observation. We incorporate this through the normalized baseline distribution function $\rho_N(U, \nu)$ which is defined such that $d^2U d\nu \rho_N(\vec{U}, \nu)$ is the fraction of data points *ie.* baselines in the interval $d^2U d\nu$ and $\int d^2U \int d\nu \rho_N(\vec{U}, \nu) = 1$. We use the functional forms of ρ_N determined in the Chapter 3 for the GMRT and the MWA.

Using the simulated visibilities, we evaluate the estimator as

$$\hat{E} = (\Delta U)^2 \Delta \nu \sum_{a,b} S_f^*(\vec{U}_a, \nu_b) \hat{V}(\vec{U}_a, \nu_b) \rho_N(\vec{U}_a, \nu_b) \quad (4.5)$$

where the sum is now over the baselines and frequency channels in the simulation.

The filter $S_f(\vec{U}, \nu)$ (Filter I of Chapter 3) is defined as

$$S_f(\vec{U}, \nu) = \left(\frac{\nu}{\nu_c}\right)^2 \left[S(\vec{U}, \nu) - \frac{\Theta(1 - 2|\nu - \nu_c|/B')}{B'} \int_{\nu_c - B'/2}^{\nu_c + B'/2} S(\vec{U}, \nu') d\nu' \right].$$

(4.6)

where the first term $S(\vec{U}, \nu)$ is the expected signal of the bubble that we are trying to detect. We note that this term is the matched filter that gives the maximum signal to noise ratio (SNR). The second term involving the Heaviside function $\Theta(x)$ subtracts out any frequency independent component from the frequency range $\nu_c - B'/2$ to $\nu_c + B'/2$. The latter term is introduced to subtract out the foreground contributions. The $(\nu/\nu_c)^2$ term accounts for the fact that $\rho_N(U, \nu)$ changes with frequency (equivalently wavelength).

We have used the 24 independent realizations of the simulation for the first three scenarios to determine the mean $\langle \hat{E} \rangle$ and the variance $\langle (\Delta \hat{E})^2 \rangle$ of the estimator. The high computational requirement restricts us to use just 3 realizations for the SM scenario. Only the signal is correlated with the filter, and only this is expected to contribute to the mean $\langle \hat{E} \rangle$. All the other components are uncorrelated with the filter and they are expected to contribute only to the variance $\langle (\Delta \hat{E})^2 \rangle$. The variance is a sum of three contributions (Chapter 3)

$$\langle (\Delta \hat{E})^2 \rangle = \langle (\Delta \hat{E})^2 \rangle_{HF} + \langle (\Delta \hat{E})^2 \rangle_N + \langle (\Delta \hat{E})^2 \rangle_{FG}. \quad (4.7)$$

The simulations give an estimate of $\langle (\Delta \hat{E})^2 \rangle_{HF}$ the contribution from HI fluctuations. We do not include system noise explicitly in our simulations. The noise contribution from a single visibility (eq. 4.3) is used to estimate $\langle (\Delta \hat{E})^2 \rangle_N$ (eq. 3.19 of Chapter 3). Under the assumed foreground model, the foreground contribution $\langle (\Delta \hat{E})^2 \rangle_{FG}$ is predicted to be smaller than the signal and we do not consider it here.

4.3 Results

We first consider the detection of an ionized bubbles and the estimation of its parameters in the SB scenario where there is only a single bubble in the FoV. We consider the most optimistic situation where the bubble is located in the center. In reality this can only be achieved in targeted observations of ionized bubbles around luminous QSOs. In a blind search, the bubble in general will be located at some arbitrary position in the FoV, and not the center. It has already been mentioned that the foregrounds can be removed by a suitable choice of the filter. Further, the system noise can, in principle, be reduced by increasing the observation time. The HI fluctuations outside the bubble impose a fundamental restriction on bubble detection.

4.3.1 Restriction on bubble detection

We have carried out simulations for different values of the bubble radius R_b chosen uniformly at an interval of 2 Mpc in the range 4 to 50 Mpc. In each case we consider only the most optimistic situation where the bubble radius R_f used in the filter is precisely matched to R_b . In reality it is necessary to try filters of different radius R_f to determine which gives the best match.

Figures 4.4 and 4.5 shows the results for the GMRT and the MWA respectively. We compare the analytic predictions of the Chapter 3 (left panel) with the prediction of our simulations (right panel). The analytical predictions for the mean value $\langle \hat{E} \rangle$ arising from the signal and $\sqrt{\langle (\Delta \hat{E})^2 \rangle_{HF}}$ due to the HI fluctuations are respectively calculated using equations (3.15) and (3.22) of the Chapter 3. The signal depends on the bubble radius R_b and the mean neutral fraction which is taken to be $x_{\text{HI}} = 1$. The uncertainty due to the HI fluctuations is calculated using the dark matter power spectrum under the assumption that the HI traces the dark matter.

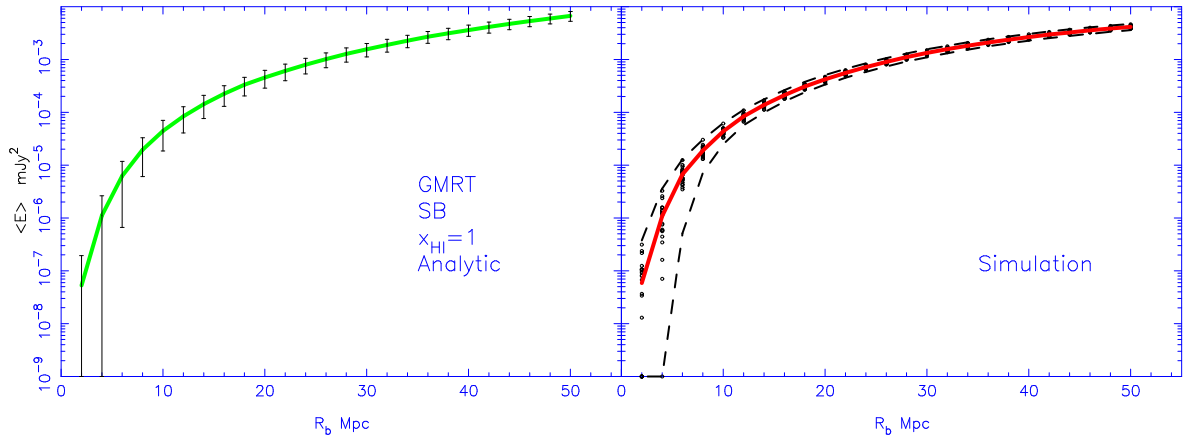


Figure 4.4: The estimator \hat{E} (defined in equation 4.4) for bubble size R_b ranging from 4 Mpc to 50 Mpc for the GMRT in the SB scenario. It is assumed that the filter is exactly matched to the bubble. The left panel shows the analytic predictions for the mean estimator $\langle \hat{E} \rangle$ and the $3-\sigma$ error-bars due to the HI fluctuations. The solid and the dashed lines in the right panel respectively show the $\langle \hat{E} \rangle$ and the $3-\sigma$ envelope determined from the simulations. The data points in the right panel show \hat{E} in the individual realizations.

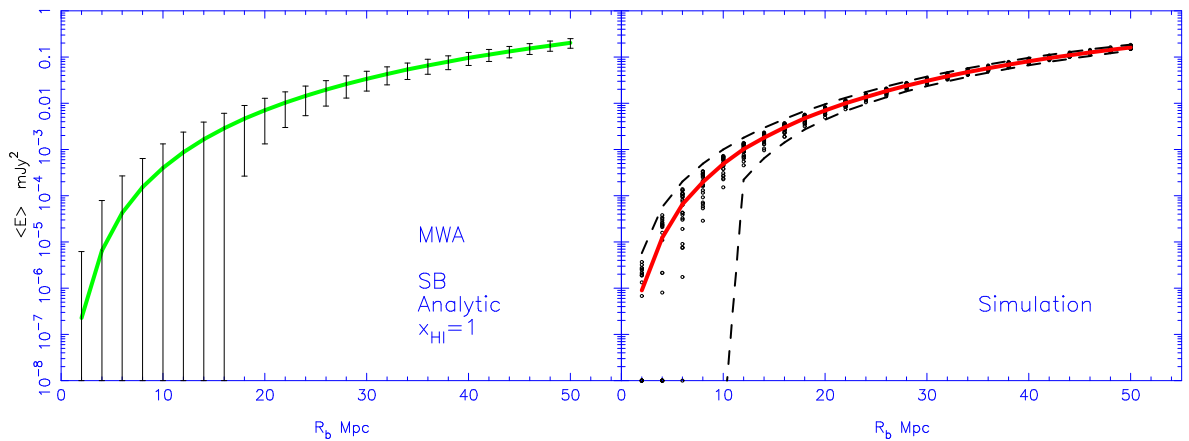


Figure 4.5: Same as the Figure 4.4 for the MWA.

4 Simulating Matched Filter Search for Ionized Bubbles

We find that $\langle \hat{E} \rangle$ and $\sqrt{\langle (\Delta \hat{E})^2 \rangle_{HF}}$ determined from the simulations is in rough agreement with the analytic predictions. The mean $\langle \hat{E} \rangle$ is in very good agreement for $R_b > 6$ Mpc, there is a slight discrepancy for smaller bubbles arising from the finite grid size (2 Mpc in the simulation). The HI fluctuations $\sqrt{\langle (\Delta \hat{E})^2 \rangle_{HF}}$ are somewhat underestimated by the simulations. This is more pronounced for the MWA where the limited box size of our simulations results in a FoV which is considerably smaller than the actual antennas. We note that the 24 different values of \hat{E} determined from the different realizations of the simulation all lie within $\langle \hat{E} \rangle \pm 3\sqrt{\langle (\Delta \hat{E})^2 \rangle_{HF}}$ determined from the analytic predictions.

The good agreement between the simulation results and the analytical predictions is particularly important because each is based on several approximations, many of which differ between the two methods. Our results show that the effect of these approximations, though present, are well under control. The analytical method has the advantage that it is very easy to calculate and can be evaluated very quickly at an extremely low computational cost. Unfortunately, its utility is mainly limited to the SB scenario and it cannot be easily applied to an arbitrary PR scenario with a complicated HI distribution. Simulations, though computationally more cumbersome and expensive, are useful in such a situation. It is thus important to test that the two methods agree for the SB scenario where both of them can be applied. Note that the HI fluctuation predicted by the SB scenario sets the lower limit for the HI fluctuation in any of the PR models. It is expected that patchiness will increase the HI fluctuations above the SB predictions.

It is meaningful to attempt bubble detection at, say 3σ confidence level, only if $\langle \hat{E} \rangle \geq 3\sqrt{\langle (\Delta \hat{E})^2 \rangle_{HF}}$. The HI fluctuations overwhelm the signal in a situation where this condition is not satisfied, and bubble detection is not possible. In a situation where this condition is satisfied, an observed value E_o of the estimator can be interpreted as

a 3σ detection if $E_o > 3\sqrt{\langle(\Delta\hat{E})^2\rangle}$. The simulations show that a $3 - \sigma$ detection is not possible for $R_b \leq 6$ Mpc and $R_b \leq 12$ Mpc at the GMRT and MWA respectively. As noted earlier, the HI fluctuations are somewhat under predicted in the simulations and the analytic predictions $R_b \leq 8$ Mpc and $R_b \leq 16$ Mpc respectively, are somewhat larger.

The limitation on the bubble size R_b that can be detected is larger for the MWA as compared to the GMRT. This is because of two reasons, the first being the fact that the MWA has a very dense sampling of the small baselines where the HI fluctuation are very large, and the second being the large FoV. In fact, the baseline distribution of the experiment has a significant role in determining the quantum of HI fluctuations and thereby determining the lower cut-off for bubble detection. Looking for an optimum baseline distribution for bubble detection is also an issue which we plan to address in future. In a situation where the antenna layout is already in place, it may possible to tune the filter to reduce the HI fluctuations.

We have not considered the effect of peculiar velocities (Bharadwaj & Ali, 2004) in our simulations. From equation (3.22) of the Chapter 3 we see that the HI fluctuations scale as $\sqrt{\langle(\Delta\hat{E})^2\rangle_{HF}} \propto \sqrt{C_l}$, where C_l is the HI multi-frequency angular power spectrum (MAPS). The C_l s increase by a factor ~ 2 due to peculiar velocities, whereby $\sqrt{\langle(\Delta\hat{E})^2\rangle_{HF}}$ goes up by a factor ~ 1.5 . This increase does not significantly change our results, and is small compared to the other uncertainties in the PR models.

The signal $\langle\hat{E}\rangle$ and the HI fluctuations $\sqrt{\langle(\Delta\hat{E})^2\rangle_{HF}}$ both scale as $\propto \bar{x}_{\text{HI}}$, and the lower limit for bubble detection is unchanged for smaller neutral fractions.

4.3.2 Size determination

In this subsection we estimate the accuracy to which it will be possible to determine the bubble radius R_b . This, in general, is an unknown quantity that has to be determined

4 Simulating Matched Filter Search for Ionized Bubbles

from the observation by trying out filters with different values of R_f . In the matched filter technique we expect the predicted SNR (only system noise) ratio

$$\text{SNR} = \frac{\langle \hat{E} \rangle}{\sqrt{\langle (\Delta \hat{E})^2 \rangle_{\text{NS}}}} \quad (4.8)$$

to peak when the filter is exactly matched to the signal *ie.* $R_f = R_b$. The solid line in the right panel of Figure 4.6 shows this for $R_b = 10$ Mpc. We find that the SNR peaks exactly when the filter size $R_f = 10$ Mpc. We propose that this can be used to observationally determine R_b . For varying R_f , we consider the ratio of the observed value E_o to the expected system noise $\sqrt{\langle (\Delta \hat{E})^2 \rangle_{\text{NS}}}$, referring to this as the SNR. The R_f value where this SNR peaks gives an estimate of the actual bubble size R_b . The observed SNR will differ from the predictions of eq. (4.8) due to the HI fluctuations outside the bubble. These variations will differ from realization to realization and this can introduce uncertainties in size estimation. We have used the simulations to estimate this.

The left panel of Figure 4.6 shows the SNR as a function of R_f for 4 different realizations of the simulation for the GMRT with bubble size $R_b = 10$ Mpc. We see that for $R_f \leq R_b$ the SNR shows a very similar behavior in all the realizations, and it always peaks around 10 Mpc as expected. For $R_f > R_b$ the behavior of the SNR as a function of R_f shows considerable variation across the realizations. In some cases the drop in SNR away from the peak is quite rapid whereas in others it is very gradual (for example, the dashed-dot-dot curve). In many cases there is an spurious extra peak in the SNR at an R_f value that is much larger than R_b . These spurious peaks do not pose a problem for size determination as they are well separated from R_b and can be easily distinguished from the genuine peak.

The error-bars in the right panel of Figure 4.6 show the $3 - \sigma$ fluctuation in the

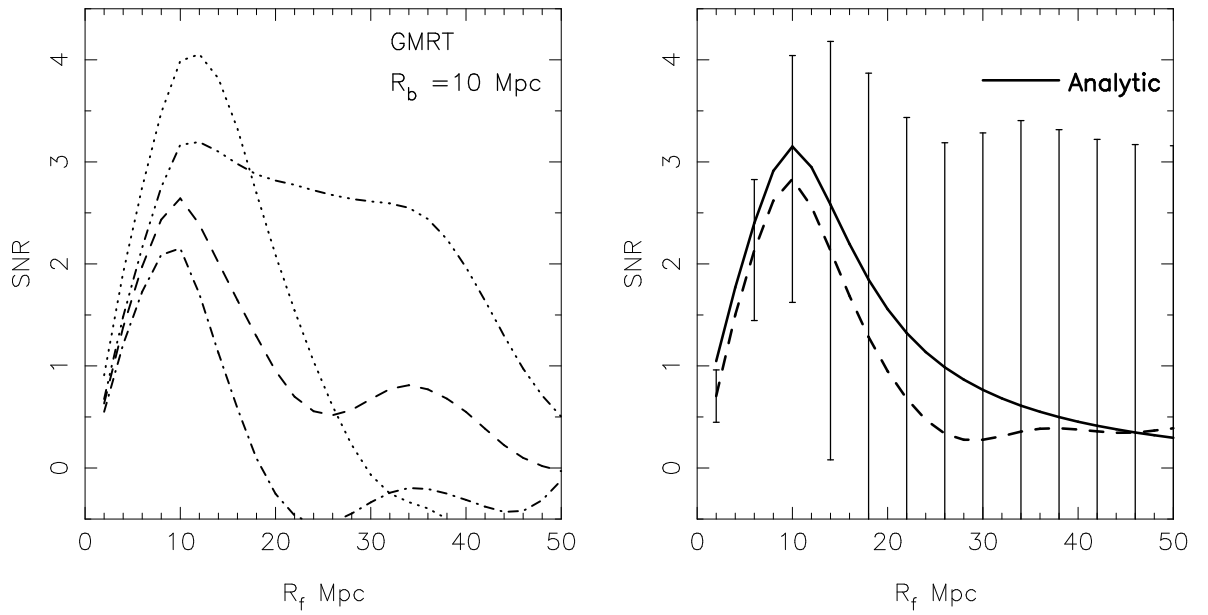


Figure 4.6: The $\text{SNR} = \langle \hat{E} \rangle / \sqrt{\langle (\Delta \hat{E})^2 \rangle_{\text{NS}}}$ for 1000 hrs observation with the GMRT as a function of the filter size R_f for the case where the actual bubble size is $R_b = 10$ Mpc . The left panel shows 4 different realizations of the simulation. The right panel shows the mean SNR and $3 - \sigma$ error-bars calculated using 24 realizations. The solid line shows the analytical predictions.

4 *Simulating Matched Filter Search for Ionized Bubbles*

simulated SNR determined from 24 realizations of the simulation. Note that the fluctuations at different R_f are correlated. Although the overall amplitude changes from one realization to another, the shape of the curve in the vicinity of $R_f = R_b$ is nearly invariant across all the realizations. In all of the 24 realizations we can identify a well defined peak at the expected value $R_f = R_b$.

Figures 4.7 and 4.8 show the results for a similar analysis with $R_b = 20$ Mpc for the GMRT and the MWA respectively. It is not possible to detect a bubble of size $R_b = 10$ Mpc with the MWA, and hence we do not show this. Here again, we find that for all the realizations of the simulations the SNR peaks at $R_f = R_b$. The relative variations in the SNR across the realizations is much less for $R_b = 20$ Mpc as compared to 10 Mpc and there are no spurious peaks. Also, for the same bubble size the variations are smaller for the GMRT as compared to the MWA. We do not find any spurious peaks for $R_b = 20$ Mpc.

A point to note is that the mean SNR determined from the simulations is somewhat smaller than the analytic predictions, both being shown in the right panels of Figures 4.6, 4.7 and Figure 4.8. There are a couple of reasons that could account for this namely, (i) the bubble in the simulation is not exactly a sphere because of the finite grid size and thus the match between the filter and the signal is not perfect even when the sizes are same and (ii) the finite box-size imposes a minimum baseline beyond which the signal is not represented in the simulation.

Based on our results we conclude that in the SB scenario for the GMRT the accuracy to which the bubble size can be determined in our simulations is decided by the resolution 2 Mpc and not by the HI fluctuations. In reality the limitation will come from the angular resolution of the instrument which sets the limit at 0.5 Mpc for the GMRT and 8 Mpc for the MWA.

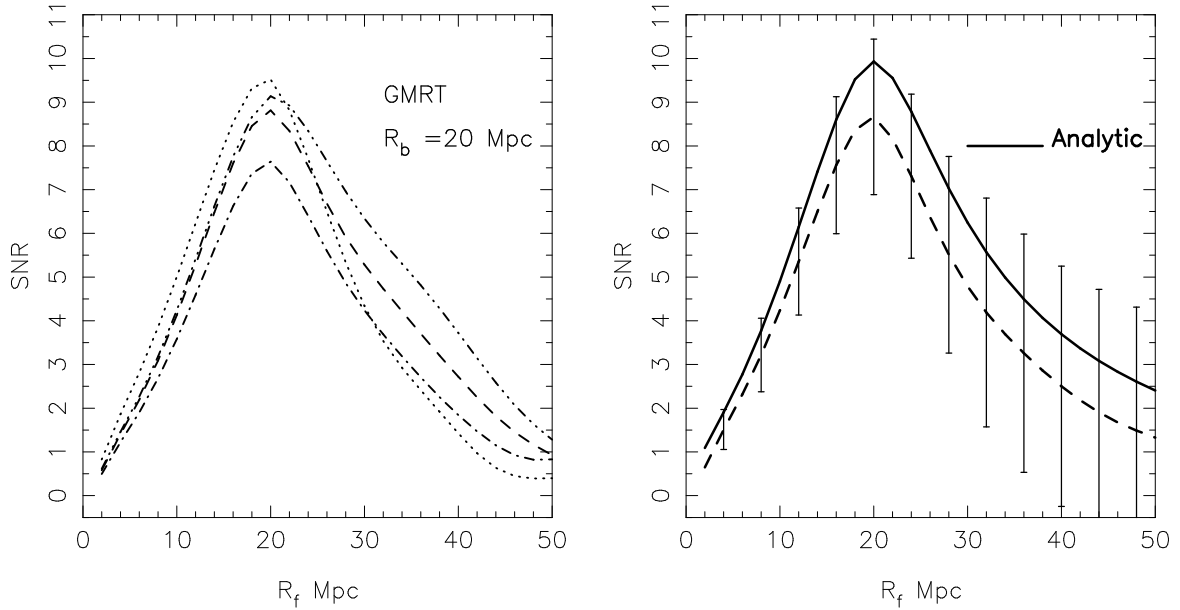


Figure 4.7: Same as the Figure 4.6 for $R_b = 20$ Mpc for the GMRT.

The height of the SNR peak depends on the neutral fraction and it can be used to observationally determine this. We find that the HI fluctuations do not change the position of the peak but introduce considerable variations in its height even if $x_{\text{HI}} = 1$. The HI fluctuations restrict the accuracy to which the neutral fraction can be estimated, an issue that we propose to address in future work.

4.3.3 Determining the position

In the previous two subsections, we have considered cases where the bubble's position is known. Here we assume that the bubble's size is known and we estimate the accuracy to which its position can be determined in the presence of HI fluctuations. The situation considered here is a blind search whereas the former is a targeted search centered on a QSO.

In a real situations it would be necessary to jointly determine four parameters the bubble radius R_b , two angular coordinates (θ_x, θ_y) and the central frequency ν_c from

4 Simulating Matched Filter Search for Ionized Bubbles

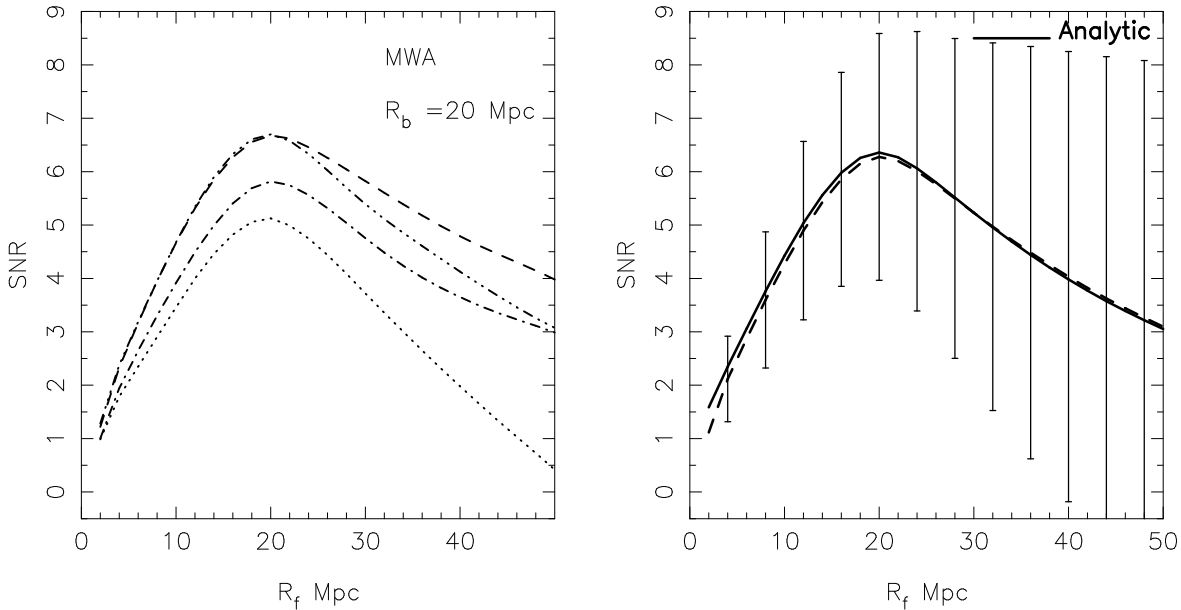


Figure 4.8: Same as the Figure 4.6 for $R_b = 20$ Mpc for the MWA.

the observation. However, to keep the computational requirement under control, in this analysis we assume that R_b is known. The bubble is placed at the center of the FoV and frequency band, and we estimate how well the position can be recovered from the simulation. To determine the bubble's position we move the center of the filter to different positions and search for a peak in the SNR. To reduce the computational requirement, this is done along one direction at a time, keeping the other two directions fixed at the bubble's actual center. We have also carried out simulations where the bubble is located off-center. We do not explicitly show these results because they are exactly the same as when the bubble is at the center except for the fact that the value of the peak SNR is lower because of the primary beam pattern.

Figure 4.9 shows the results for $R_b = 10$ Mpc for the GMRT. The left panel shows results for 4 realizations of the simulation, the right panels show the mean and $3-\sigma$ determined from 24 realizations of the simulations and the analytic prediction for the mean value. In all cases a peak is seen at the expected position matched with the bubble's actual center. The HI fluctuations pose a severe problem for determining the

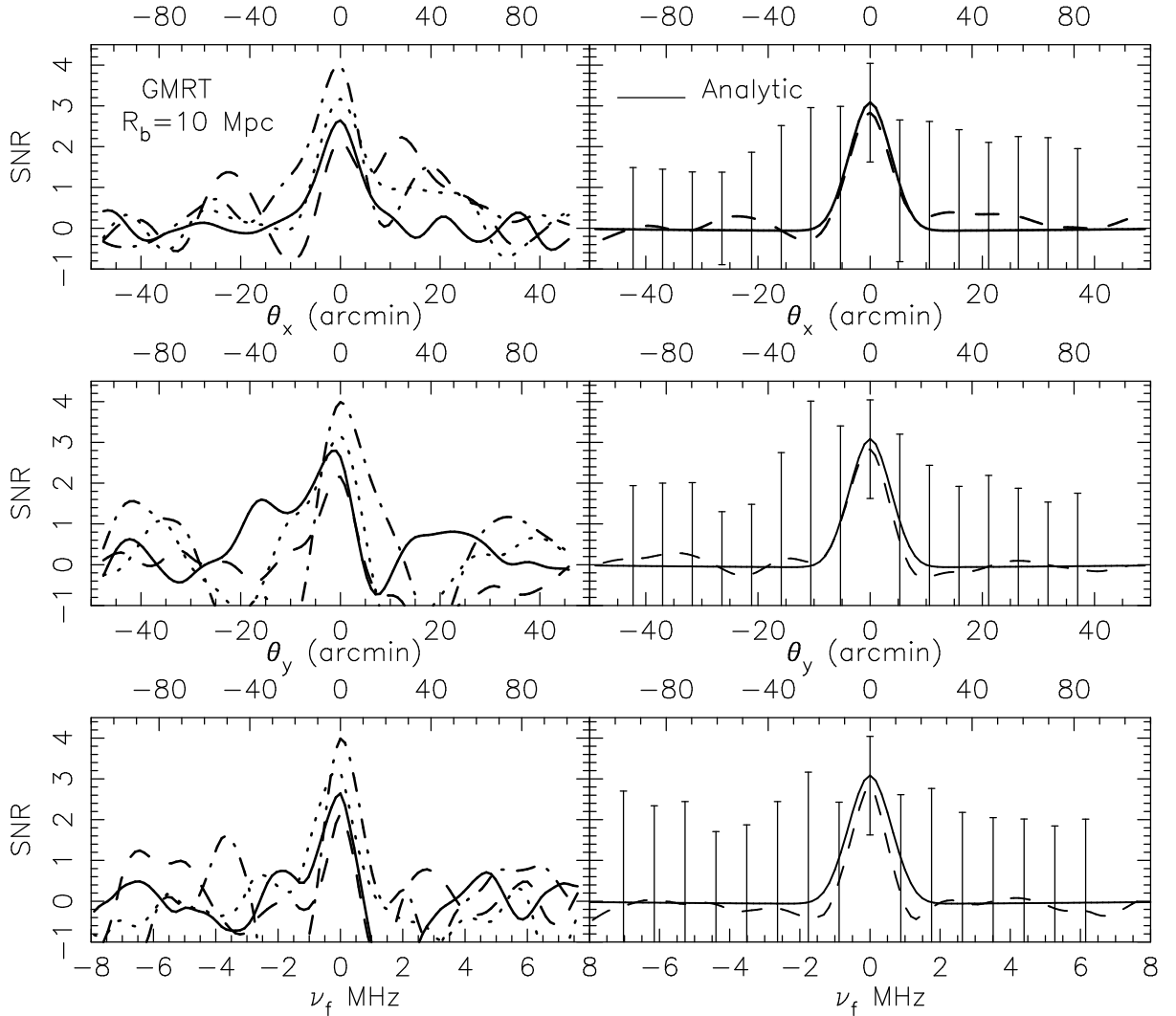


Figure 4.9: The SNR for 1000 hrs GMRT observations for a bubble of size $R_b = 10$ Mpc located at the center of the field of view. The filter scans along $\theta_x, \theta_y, \nu_f$ (top, middle, bottom) to determine the bubble's position. The left panel shows results for 4 realizations of the SB simulation, the right panels show the mean (dashed curve) and $3\text{-}\sigma$ error-bars determined from 24 realizations of the simulation and the analytic prediction for the mean (solid curve).

bubble's position as it introduces considerable fluctuations in the SNR. In some cases these fluctuations are comparable to the peak at the bubble's actual position (see the dashed line in the upper left panel). The possibility of spurious peaks makes it difficult to reliably determine the bubble's position.

We present the results for $R_b = 20$ Mpc in Figures 4.10 and 4.11 for the GMRT and MWA respectively. The HI fluctuations do not pose a problem for determining the position of such bubbles using the GMRT. In all the realizations of the GMRT simulations there is a peak at the expected position. The FWHM ~ 40 Mpc is approximately the same along θ_x, θ_y and ν_f and is comparable to the separation at which the overlap between the bubble and the filter falls to half the maximum value. The HI fluctuations does introduce spurious peaks, but these are quite separated from the actual peak and have a smaller height. We do not expect these to be of concern for position estimation.

The MWA simulations all show a peak at the expected bubble position. The FWHM along θ (~ 60 Mpc) is somewhat broader than that along ν (~ 40 Mpc). The low spatial resolution ~ 8 Mpc possibly contributes to increase the FWHM along θ . The HI fluctuations introduce spurious peaks whose heights are $\sim 50\%$ of the height of the actual peak.

4.3.4 Bubble detection in patchy reionization

The SB scenario considered till now is the most optimistic scenario in which the HI traces the dark matter. The presence of ionized patches other than the one that we are trying to detect is expected to increase the contribution from HI fluctuations. We first consider the PR1 scenario where there are several additional ionized bubbles of radius 6 Mpc in the FoV. Figures 4.12 & 4.13 show the mean value of the estimator $\langle \hat{E} \rangle$ and $3 - \sigma$ error-bars as a function of R_f for the GMRT and the MWA respectively. These

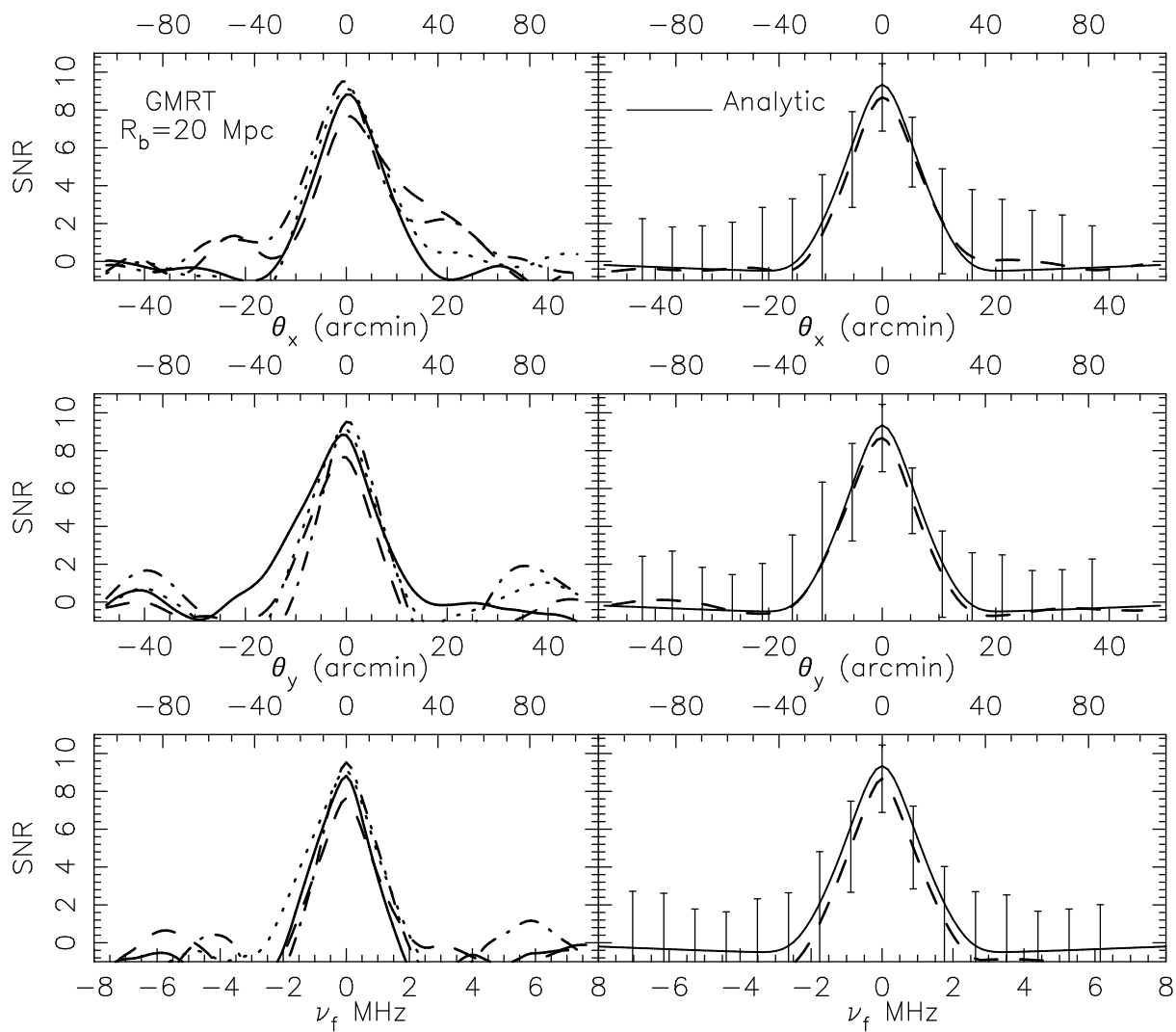


Figure 4.10: Same as the Figure 4.9 for $R_b = 20$ Mpc for the GMRT.

4 Simulating Matched Filter Search for Ionized Bubbles

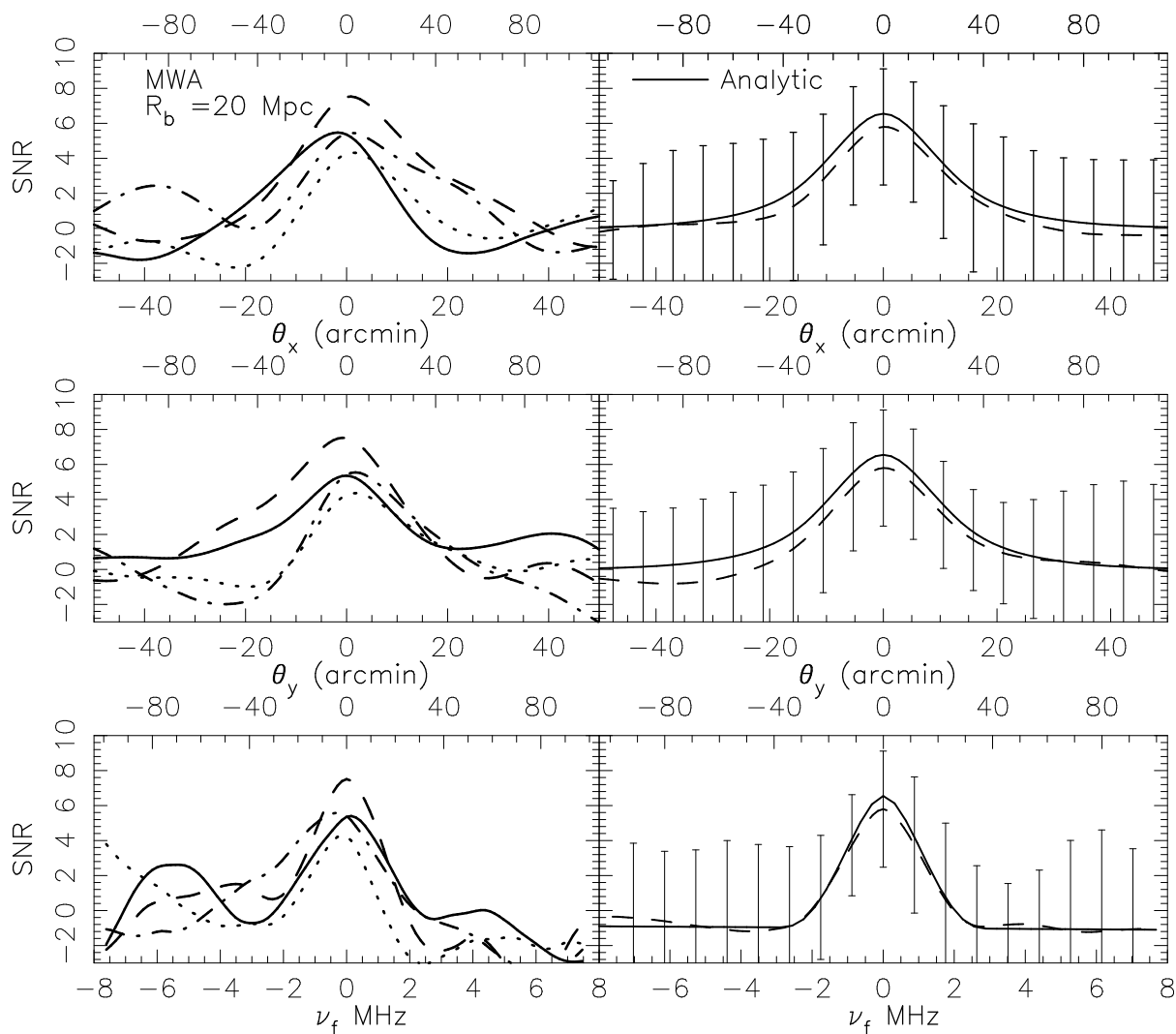


Figure 4.11: Same as the Figure 4.9 for $R_b = 20$ Mpc for the MWA.

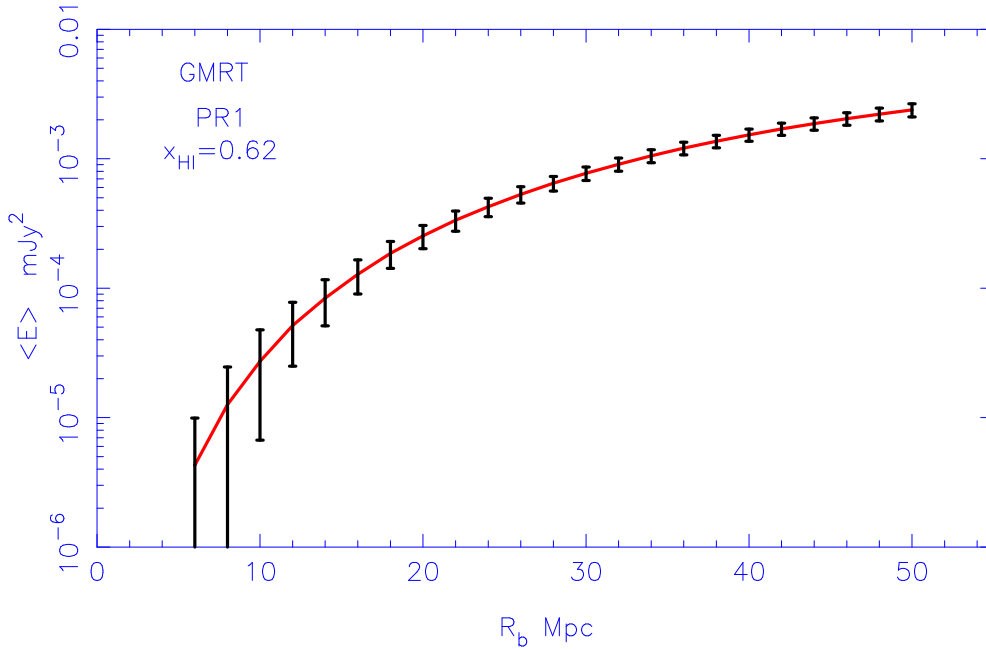


Figure 4.12: The mean $\langle \hat{E} \rangle$ and $3 - \sigma$ error-bars of the estimator as a function of R_f for the GMRT estimated from 24 different realizations of the PR1 scenario. In all cases the filter is exactly matched to the bubble.

were estimated from 24 different realizations of the simulation, using a filter exactly matched to the bubble.

We find that the results are very similar to those for the SB scenario except that the signal is down by 0.6 due to the lower neutral fraction ($x_{\text{HI}} = 0.62$) in the PR scenarios. Ionized bubbles with radius $R_b = 8$ Mpc and $= 12$ Mpc or smaller cannot be detected by the GMRT and MWA respectively due to the HI fluctuations. These limits are similar to those obtained in simulations of the SB scenario.

In the PR2 scenario the FoV contains other ionized bubbles of the same size as the bubble that we are trying to detect. We find that bubble detection is not possible in such a situation, the HI fluctuations always overwhelm the signal. This result obviously depends on number of other bubbles in the FoV, and this is decided by x_{HI} which we take to be 0.62. A detection may be possible at higher x_{HI} where there would be fewer bubbles in the FoV.

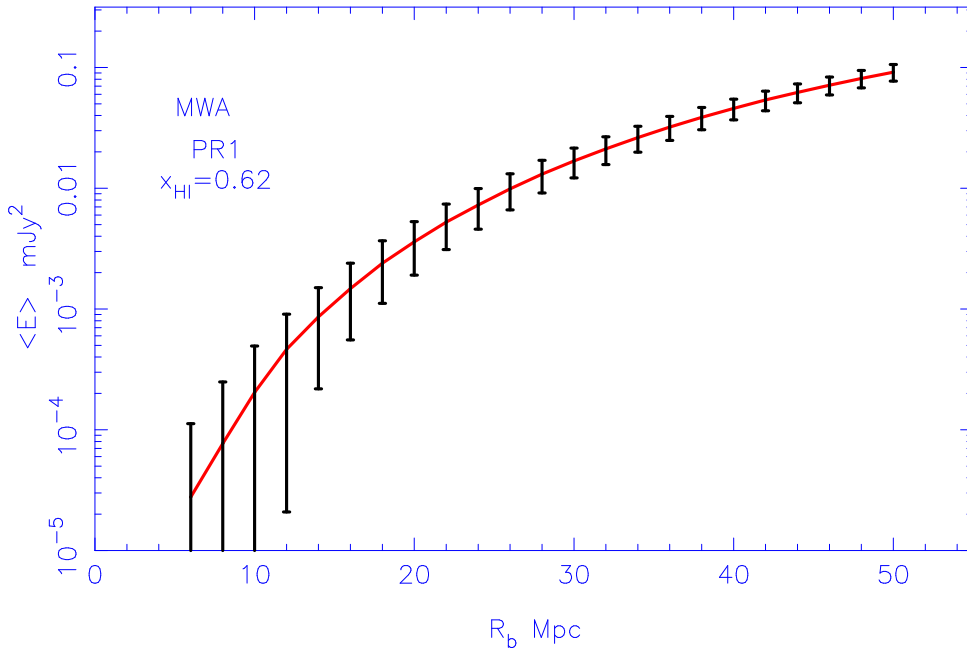


Figure 4.13: Same as the Figure 4.12 for the MWA.

In the SM scenario, the very large computation time restricts us from generating several realizations with central ionized regions of different sizes. Hence we are unable to study the restriction on bubble detection. We have only three realizations all of which have the same ionized region located at the center of the box. Based on these we find that the mean estimator $\langle \hat{E} \rangle$ is ~ 30 times larger than the standard deviation due to HI fluctuations. The detection of a bubble of the size present in our simulation (Figure 4.1) is not restricted by the HI fluctuations. We present size determination results in Figure 4.14. We see that the SNR peaks at $R_f = 42$ Mpc and not at $R_f = 27$ Mpc. Recall that in the 21-cm map (Figure 4.1) we have visually identified the former as the bubble's outer radius which includes several small patchy ionized regions towards the periphery and the latter is the inner radius which encloses the completely ionized region. We see that the matched filter identifies the bubble's outer radius. To study the effect of non-sphericity we compare our results in Figure 4.14 with the predictions for a spherical bubble of radius $R_b = 42$ Mpc embedded in uniform HI with the same neutral fraction $x_{\text{HI}} = 0.5$.

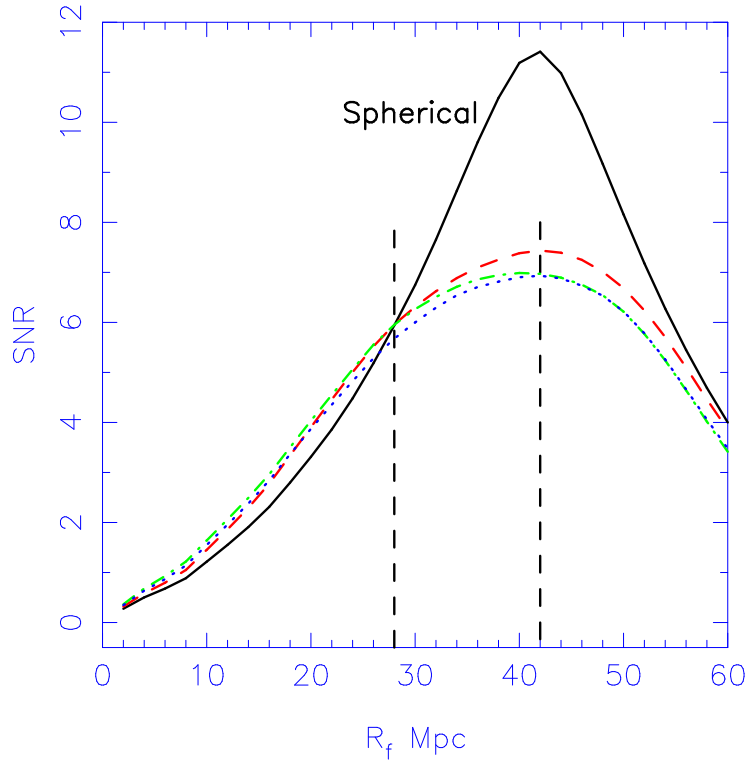


Figure 4.14: Same as Figure 4.6 for the SM scenario for the GMRT. The dotted, dashed, dash-dotted and dashed lines show results for three different realizations. To show the effect of non-sphericity, we compare these results with predictions for a spherical bubble of size $R_b = 42$ Mpc embedded in uniform HI with neutral fraction $x_{\text{HI}} = 0.5$ (solid line). The vertical line at $R_f = 28$ Mpc shows the radius up to which the bubble is fully ionized and the SNR follows the spherical predictions. The SNR peaks at $R_f = 42$ Mpc marked by another vertical line.

We find that our results for the SM scenario follow the spherical bubble prediction up to a filter size $R_f = 28$ Mpc (marked with a vertical line in Figure 4.14), corresponding to the bubble's inner radius which encloses a perfectly spherical ionized region. Beyond this, and upto the outer radius of 42 Mpc, the HI is not fully ionized. There are neutral patches which introduce deviations from spherical symmetry and cause the SNR to fall below the predictions of a spherical bubble beyond $R_f = 28$ Mpc. The deviations from sphericity also broadens the peak in the SNR relative to the predictions for a spherical bubble.

Our results based on the SM scenario show that the matched filter technique works well for bubble detection and for determining the bubble's size even when there are deviations from sphericity. We obtain good estimates for the extents of both, the completely ionized region and the partially ionized region. For the SM scenario, Figure 4.15 shows how well the bubble's position can be determined in a blind search. We have followed the same method as described for the SB scenario in subsection 3.3. We see that the SNR peaks at the expected position. Further, as the bubble size is quite large $\gtrsim 27$ Mpc there are no spurious peaks.

4.4 Redshift Dependence

Results shown so far are all at only one redshift $z = 6$. It would be interesting and useful to have predictions for higher redshifts. However, addressing this issue through direct computations at different redshifts would require considerable computation beyond the scope of this work. Since we find that the analytic predictions of the Chapter 3 are in good agreement with the simulations of the SB scenario, we use the analytic formalism to predict how different quantities are expected to scale with increasing z .

The redshift dependence of some of the quantities like the system noise, the back-

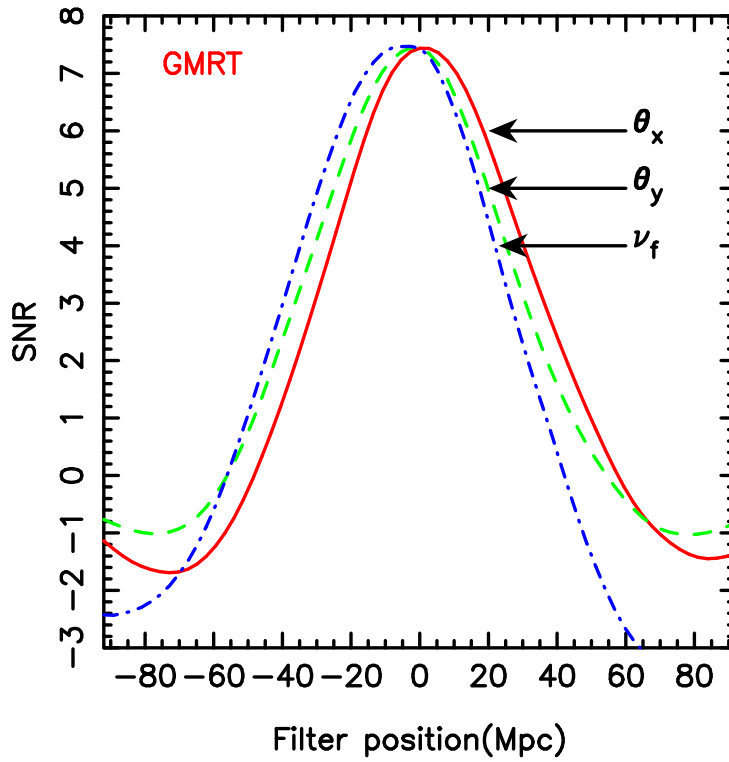


Figure 4.15: Same as Figure 4.9 for the SM scenario for the GMRT. The x-axis shows the comoving distance of the filter position from the center of the box. The three curves respectively show results for a search along three θ_x , θ_y and ν axes.

ground 21-cm brightness \bar{I}_ν , and the angular and frequency extent of a bubble of fixed comoving radius causes the SNR to decrease with increasing z . On the other hand the z dependence of the neutral fraction, the baseline distribution function and the effective antenna collecting area acts to increase the SNR at higher redshifts. We find that with increasing z both $\langle \hat{E} \rangle$ and $\sqrt{\langle (\Delta \hat{E})^2 \rangle_{\text{HF}}}$ decrease by nearly the same factor so that the restriction on bubble detection does not change significantly at higher redshift in the SB scenario. Assuming that the neutral fraction does not change with z , the SNR for bubble detection decreases with increasing redshift, the change depending on the bubble size. For example, for the GMRT at $z = 10$ the SNR decreases by a factor ~ 7 and 6 for bubbles of size $R_b = 10$ and 20 Mpc respectively. For the MWA this factor is 3 for both these bubble sizes. We expect a similar change in the SNR for the patchy reionization scenarios. The drop in SNR is slower for the MWA relative to the GMRT because the effective antenna collecting area of the MWA increases at higher redshifts.

The SNR is directly proportional to the global neutral fraction x_{HI} which increases with z . The details of how x_{HI} and the HI fluctuations change with redshift depends on how reionization proceeds with time, an issue beyond the scope of this thesis.

4.5 Summary

We have used a visibility-based formalism, introduced in Datta, Bharadwaj & Choudhury (2007), to simulate the detection of spherical HII bubbles in redshifted 21 cm maps through a matched-filtering technique. The main aim of this work is to use simulations to quantifying the limitations for bubble detection arising from the HI fluctuations outside the bubble. We have computed the results for two instruments, namely, the GMRT and the upcoming MWA. Our main conclusions are as follows:

- In the case where the HI fluctuations outside the bubble trace the dark matter distribution (SB scenario), we find that bubbles with radius $R_b = 6$ Mpc and $= 12$ Mpc or smaller cannot be detected by the GMRT and MWA respectively due to the HI fluctuations. Note that this limitation is fundamental to the observations and cannot be improved upon by increasing integration time.
- For targeted observations of ionized bubbles, the bubble size can be determined to an accuracy limited by the instrument's resolution; we find that HI fluctuations do not play any significant role. However, the HI fluctuations can restrict the accuracy to which the neutral fraction can be estimated. In addition, we find that determining the position of the bubble in a blind search could be quite difficult for small (~ 10 Mpc) bubbles as the HI fluctuations introduce large fluctuations in the signal; for larger bubbles the accuracy is determined by the instrument's resolution.
- In a scenario of patchy reionization where the targeted HII region is surrounded by many small ionized regions of size ~ 6 Mpc (PR1 scenario), the lower limit for bubble detection is similar to that in the SB scenario. Thus the assumption that the HI traces the dark matter gives a reasonable estimate of the contribution from HI fluctuations if the background ionized bubbles are small ~ 6 Mpc. However, the situation is quite different when the surrounding bubbles are of similar size as the targeted bubble (PR2 scenario). The large HI fluctuations do not permit bubble detection for a neutral fraction $x_{\text{HI}} < 0.6$. Thus for $x_{\text{HI}} = 0.6$ or lower, bubble detection is possible only if the other ionized regions in the FoV are much smaller than the bubble that we are trying to detect.
- The matched filter technique works well for more realistic cases based on the semi-numeric modelling of ionized regions (Choudhury, Haehnelt & Regan, 2008). Here

4 Simulating Matched Filter Search for Ionized Bubbles

the bubbles are substantially non-spherical because of surrounding bubbles and inhomogeneous recombination. Our method gives a good estimate of the size of both the fully ionized and the partially ionized regions in the bubble.

To put our conclusions in an overall perspective, let us consider an ionized bubble around a luminous QSO at $z \gtrsim 6$. We expect $R_b \gtrsim 30\text{Mpc}$ from studies of QSO absorption spectra (Wyithe & Loeb 2004; Mesinger & Haiman 2004). It has also been pointed out that these bubbles may survive as large “gray fossils” a long time after the source has shut down (Furlanetto et al. 2008). It will be possible to detect such bubbles only if the background bubbles are smaller, say, $< 30\text{Mpc}$. We find from models of Mesinger & Furlanetto (2007) that the typical sizes of ionized regions when $x_{\text{HI}} \sim 0.3(0.1)$ is $\sim 20(70)\text{Mpc}$. Though these values could be highly model-dependent, it still gives us an idea that the bubbles around the luminous QSO would be detectable even in a highly ionized IGM with, say, $x_{\text{HI}} \sim 0.3$. If the size of the targeted bubble is larger, then this constraint is less severe. This gives a realistic hope of detecting these bubbles at $z \gtrsim 6$ with near-future facilities.

A caveat underlying a large part of our analysis is the assumption that the bubbles under consideration are perfectly spherical. This is not the case in reality. For example, non-isotropic emission from the sources (QSOs), density fluctuations in the IGM and radiative transfer effects would distort the shape of the bubble. The semi-numeric simulations (SM scenario) incorporate some of these effects and give an estimate of the impact of the deviations from sphericity on bubble detection. This is an important issue which we plan to address in more detail in future. In addition, the finite light travel time gives rise to an apparent non-sphericity even if the physical shape is spherical (Wyithe & Loeb, 2004a; Yu, 2005). This effect can, in principle, be estimated analytically and incorporated in the filter. We plan to address this effect in future.

5 Optimum Redshift for Detecting Ionized Bubbles*

5.1 Introduction

In Chapter 3 we have introduced a matched filter technique to detect individual ionized bubbles in 21-cm maps. The technique optimally combines the entire signal from an ionized bubble while minimizing the noise and foreground. In Chapter 4 we use different simulated 21-cm maps to study the impact of the HI fluctuations outside the bubble that we are trying to detect.

Various redshift dependent parameters are important in bubble detection. The background 21-cm brightness and the angular and frequency extent of a bubble of a fixed comoving size increase from higher to lower redshift. The system noise in low frequency radio experiments is dominated by the sky temperature which becomes lower at higher

* *A sharpened, compact version of this chapter is presented in the paper “The optimal redshift for detecting ionized bubbles in HI 21-cm maps” by Datta, Bharadwaj & Choudhury (2009)*

5 Optimum Redshift for Detecting Ionized Bubbles

frequency. This makes the noise lower at lower redshifts. All the above mentioned factors are expected to enhance the signal to noise ratio (SNR) at lower redshifts. On the other hand, the neutral hydrogen fraction decreases as the reionization process proceed and it becomes almost zero around redshift $z = 6$. We will also see later in the text that the baseline distribution also changes significantly with the frequency band of our interest. This change is also expected to enhance the SNR at higher redshifts. Again, for MWA like experiments the increase in effective collecting area of the individual antenna is expected to reduce the system noise at higher redshifts. Together these parameters will try to suppress the SNR at lower redshifts with no signal at redshift $z = 6$ where the Universe is completely reionized. Because of these two oppositely behaving set of parameters there is an intermediate redshift where the SNR for a bubble of fixed co-moving size peaks. The detection of ionized bubbles is optimal at this redshift. The prior knowledge of this optimum redshift is important for any future attempt to detect ionized bubbles in 21-cm maps.

In this Chapter we investigate the optimum redshift to detect ionized bubbles considering different models of the neutral fraction evolution with redshift. Predictions are made for the GMRT and the MWA. We also establish scaling relations for the SNR with redshift for a fixed value of bubble size.

The Chapter is organized as follows. We begin with a brief description on the 21-cm signal from an ionized bubbles and its redshift dependence Section 5.2. In Section 5.3 we present a short note on our matched filtering technique to detect ionized bubbles. In Section 5.4 we establish scaling relations for the SNR with redshift considering both uniform-frequency independent and nonuniform-frequency dependent baseline distribution. In the same section we also briefly describe the models of HI evolution that we adopt for our calculations. We present our results in Section 5.5 and conclusions in Section 5.6

Throughout out this Chapter we adopt cosmological parameters from Dunkley et al.(2008). For the GMRT we use the antenna specifications from their website and for the MWA we use the instrumental parameters from Bowman et. al. (2007).

5.2 Ionized Bubbles in Redshifted 21-cm Observations

The quantity measured in radio-interferometric observations is the visibility $V(\vec{U}, \nu)$ which is measured in a number of frequency channels ν across a frequency bandwidth B for every pair of antennas in the array. The visibility is related to the sky specific intensity $I_\nu(\vec{\theta})$ as

$$V(\vec{U}, \nu) = \int d^2\theta A(\vec{\theta}) I_\nu(\vec{\theta}) e^{2\pi\vec{\theta}\cdot\vec{U}} \quad (5.1)$$

where the baseline $\vec{U} = \mathbf{d}/\lambda$, \mathbf{d} is physical separation between a pair of antennas projected on the plane perpendicular to the line of sight. λ and $\vec{\theta}$ respectively are observing wavelength and two dimensional vector in the plane of the sky with origin at the center of the field of view, and $A(\vec{\theta})$ is the beam pattern of the individual antenna. We have used $A(\vec{\theta})$ described in Chapter 3. The visibility recorded in radio-interferometric observations is a combination of four separate contributions

$$V(\vec{U}, \nu) = S(\vec{U}, \nu) + HF(\vec{U}, \nu) + N(\vec{U}, \nu) + F(\vec{U}, \nu) \quad (5.2)$$

where $S(\vec{U}, \nu)$ is the HI signal that we are interested in, $HF(\vec{U}, \nu)$ is contribution from fluctuating HI outside the target bubble, $N(\vec{U}, \nu)$ is the system noise which is inherent to the measurement and $F(\vec{U}, \nu)$ is the contribution from other astrophysical sources referred to as the foregrounds.

We consider a spherical ionized bubble of comoving radius R_b centered at redshift z_c at the center of the FoV. This bubble is also assumed to be embedded in an uni-

5 Optimum Redshift for Detecting Ionized Bubbles

form inter-galactic medium (IGM) with neutral hydrogen fraction x_{HI} . The planar section through the bubble at a comoving distance r_ν is a disk of comoving radius $R_\nu = R_b \sqrt{1 - (\Delta\nu/\Delta\nu_b)^2}$ where $\Delta\nu = \nu_c - \nu$ is the distance from the the bubble center ν_c in frequency space with $\nu_c = 1420 \text{ MHz}/(1 + z_c)$ and $\Delta\nu_b = R_b/r'_{\nu_c}$ is the bubble size in the frequency space. The expected observed visibility from this bubble can be written as (for details see Chapter 3)

$$S_{\text{center}}(\vec{U}, \nu) = -\pi \bar{I}_\nu x_{\text{HI}} \theta_\nu^2 \left[\frac{2J_1(2\pi U \theta_\nu)}{2\pi U \theta_\nu} \right] \Theta \left(1 - \frac{|\nu - \nu_c|}{\Delta\nu_b} \right) \quad (5.3)$$

where $\bar{I}_\nu = 2.5 \times 10^2 \frac{Jy}{sr} \left(\frac{\Omega_b h^2}{0.02} \right) \left(\frac{0.7}{h} \right) \left(\frac{H_0}{H(z)} \right)$ is the radiation background from the uniform HI distribution. $\theta_\nu = R_\nu/r_\nu$ is angular radius of the circular disc through the bubble at comoving distance r_ν . $J_1(x)$ and $\Theta(x)$ are the first order Bessel function and the Heaviside step function respectively.

The peak value of the signal is $S(0, \nu) = \pi \bar{I}_\nu \theta_\nu^2$. For a fixed value of bubble size the peak value changes with redshift. The Bessel function $J_1(x)$ has the first zero crossing at $x = 3.83$. As a result, in baseline the signal $S(\vec{U}, \nu)$ extends to $U_0 = 0.61\theta_\nu^{-1}$ where it has the first zero crossing. The signal extends over $\Delta\nu = \pm\Delta\nu_b$ in frequency. Note that the angular size θ_ν and extent in frequency of a bubbles for a fixed value of comoving size change with redshift because of change in comoving distance r_ν and r'_ν . We will discuss the effect of these change on bubble detection at various redshifts in Section 5.4. Detecting these ionized bubbles will be a big challenge because the signal is buried in noise and foregrounds which are both considerably larger in amplitude. Whether we are able to detect the ionized bubbles or not depends critically on our ability to construct optimal filters which discriminate the signal from other contributions.

5.3 Matched Filtering Technique to Detect Ionized Bubbles

For optimal signal detection we consider the estimator (Chapter 3)

$$\hat{E} = \left[\sum_{a,b} S_f^*(\vec{U}_a, \nu_b) \hat{V}(\vec{U}_a, \nu_b) \right] / \left[\sum_{a,b} 1 \right] \quad (5.4)$$

where $S_f(\vec{U}, \nu)$ is a filter which has been constructed to detect a particular ionized bubble, $\hat{V}(\vec{U}_a, \nu_b)$ respectively refer to the observed visibilities and \vec{U}_a and ν_b refer to the different baselines and frequency channels in the observation and in eq. (5.4) we are to sum over all independent data points (visibilities). The filter $S_f(\vec{U}, \nu)$ depends on $[R_f, z_c, \vec{\theta}_c]$ the comoving radius, redshift and angular position of the bubble that we are trying to detect.

We now calculate $\langle \hat{E} \rangle$ the expectation value of the estimator. Here the angular brackets denote an average with respect different realizations of the HI fluctuations, noise and foregrounds, all of which have been assumed to be random variables with zero mean. This gives $\langle \hat{V}(\vec{U}, \nu) \rangle = S(\vec{U}, \nu)$ in the continuum limit and

$$\langle \hat{E} \rangle = \int d^2U \int d\nu \rho_N(\vec{U}, \nu) S_f^*(\vec{U}, \nu) S(\vec{U}, \nu) \quad (5.5)$$

The variance of the estimator which is the sum of the contributions from the noise (NS), the foregrounds(FG) and the HI fluctuations (HF) can be written as

$$\langle (\Delta \hat{E})^2 \rangle = \langle (\Delta \hat{E})^2 \rangle_{\text{NS}} + \langle (\Delta \hat{E})^2 \rangle_{\text{FG}} + \langle (\Delta \hat{E})^2 \rangle_{\text{HF}} . \quad (5.6)$$

5 Optimum Redshift for Detecting Ionized Bubbles

Assuming that the noise in different baselines and frequency channels are uncorrelated we have

$$\langle (\Delta \hat{E})^2 \rangle_{\text{NS}} = \sigma^2 \int d^2U \int d\nu \rho_N(\vec{U}, \nu) |S_f(\vec{U}, \nu)|^2 . \quad (5.7)$$

where σ is the rms. noise in the image.

The variance due to HI fluctuations is given as

$$\begin{aligned} \langle (\Delta \hat{E})^2 \rangle_{\text{HF}} &= \int d^2U \int d\nu_1 \int d\nu_2 \left(\frac{dB}{dT} \right)_{\nu_1} \left(\frac{dB}{dT} \right)_{\nu_2} \\ &\quad \times \rho_N(\vec{U}, \nu_1) \rho_N(\vec{U}, \nu_2) S_f^*(\vec{U}, \nu_1) S_f(\vec{U}, \nu_2) \\ &\quad \times C_{2\pi U}(\nu_1, \nu_2) \end{aligned} \quad (5.8)$$

where $C_{2\pi U}(\nu_1, \nu_2)$ is the multi-frequency angular power spectrum of the HI fluctuation from Datta, Choudhury & Bharadwaj (2007) (Chapter 2).

5.4 Redshift Dependence: Scaling Relations

5.4.1 Uniform and frequency independent baseline distribution

The estimator $\langle E \rangle$ and its variance depend on the size (R_b), redshift (z_c) and position ($\vec{\theta}_c$) of the bubble. In this Section we present a scaling relations for the estimator describing its change with redshift. We assume a bubble of fixed size at the center of the FoV and the filter is exactly matched with bubble. In a situation where the baseline distribution ($\rho(\vec{U}, \nu)$) is (i) uniform in baseline over the signal $S(\vec{U}, \nu)$ (ii) independent of frequency channels and (iii) the frequency bandwidth is much larger than the bubble

($BW \gg \Delta\nu_b$) the estimator scales exactly as

$$\langle \hat{E} \rangle(z) \propto x_{\text{HI}}^2(z) \bar{I}_\nu^2 \theta_{\nu_c}^2 \Delta\nu_b \quad (5.9)$$

where $x_{\text{HI}}(z)$ quantifies the evolution of the neutral hydrogen fraction. The redshifted 21-cm background \bar{I}_ν scales as $(1+z)^{-1.5}$ at higher redshifts. The angular size θ_{ν_c} which is $\propto 1/r_\nu$ approximately scales as $(1+z)^{-0.25}$ for a fixed value of bubble size. Similarly the frequency extent of the bubble ($2\Delta\nu_b$) decreases with redshift as $(1+z)^{-0.5}$. Considering all these quantities we get

$$\langle \hat{E} \rangle(z) \propto x_{\text{HI}}^2(z) (1+z)^{-4}. \quad (5.10)$$

The system noise is dominated by the sky temperature T_{sky} for the frequency range of interest. The sky temperature T_{sky} increases with observed wavelength and scales as $(1+z)^\beta$, where β is the spectral index. Considering this fact and under the same assumptions mentioned above the noise variance can be written as

$$\langle (\Delta \hat{E})^2 \rangle_{\text{NS}}(z) \propto x_{\text{HI}}^2(z) (1+z)^{2\beta-4}. \quad (5.11)$$

In this equation we have assumed that the individual antenna collecting area is independent of frequency (applicable to the GMRT). For MWA like antenna the individual antenna collecting area is expected to increase with observed wavelength as $\sim \lambda^2$ and the noise variance scales as

$$\langle (\Delta \hat{E})^2 \rangle_{\text{NS}}(z) \propto (1+z)^{2\beta-8}. \quad (5.12)$$

The fluctuating HI outside the ionized bubble also contribute to the variance of the estimator. This contribution can not be reduced by increasing observation time and put

5 Optimum Redshift for Detecting Ionized Bubbles

fundamental restrictions in detecting ionized bubbles. The HI distribution outside the target bubble during reionization is highly unknown and differs drastically for different models of reionizations. For simplicity we assume that the HI outside the bubble trace the dark matter distribution. The presence of other ionized regions outside the bubble are expected to increase this contribution. The assumption that the HI outside the bubble trace the dark matter distribution will give the minimum variance contribution to the estimator. Analytical derivation of the scaling relation for the $\langle(\Delta\hat{E})^2\rangle_{\text{HF}}$ is not straight forward because of the term $C_{2\pi U}(\nu_1, \nu_2)$. Assuming that the HI to trace the dark matter we numerically calculate $\langle(\Delta\hat{E})^2\rangle_{\text{HF}}$ at various redshifts using equation 5.8. We then fit the data with a power law of $(1+z)$ which comes out to be

$$\langle(\Delta\hat{E})^2\rangle_{\text{HF}} \propto x_{\text{HI}}^2(z)(1+z)^{-10.5}. \quad (5.13)$$

Detection of bubble is possible when $\langle\hat{E}\rangle(z) > \langle(\Delta\hat{E})^2\rangle_{\text{HF}}$. When this is satisfied we are interested only in $\langle\hat{E}\rangle/\sqrt{\langle(\Delta\hat{E})^2\rangle_{\text{NS}}}$ which we call SNR. Note that the term $x_{\text{HI}}(z)$ in the equations 5.9, 5.11 is almost constant along the line of sight of the ionized bubble. This factor does not affect the value of the quantity SNR. One can drop $x_{\text{HI}}(z)$ and similarly \bar{I}_ν from the filter $S_f(\vec{U}, \nu)$ without losing the effectiveness of the method. We calculate the SNR at different redshifts ranging from $z = 6$ to 16 for a fixed value of bubble size. Using equations 5.10 and 5.11 for a GMRT like antenna we have

$$SNR \propto x_{\text{HI}}(z)(1+z)^{-\beta-2} \quad (5.14)$$

For a MWA like antenna this is

$$SNR \propto x_{\text{HI}}(z)(1+z)^{-\beta} \quad (5.15)$$

Note that in the above two equations $x_{\text{HI}}(z)$ is an increasing function of redshift z and for a typical value of $\beta \approx 2.5 - 2.8$, we expect the SNR to be peaked at an intermediate redshift during reionization. As we discussed earlier this is due to three reasons, firstly the sky temperature increases at low frequency i.e., at higher redshifts. Second the background specific intensity \bar{I}_ν also decreases at higher redshift. Finally the angular size and frequency extent of the bubble also become smaller at higher redshift due to the increase in r_ν and r'_ν with redshift. We see that the two factors are opposite in nature—one increases with redshift whereas the other decreases. There is an intermediate redshift z where the SNR is maximum.

5.4.2 Non uniform and frequency dependent baseline distribution

The baseline distribution in general is not uniform in \vec{U} (see figure 3.5 in Chapter 3) and also frequency dependent. This non uniformity changes the above scaling relations. We introduce a parameter n to take into account this effect and now modified SNR can be written as

$$SNR \propto x_{\text{HI}}(z)(1+z)^{n/2-\beta-2} \quad (5.16)$$

for the GMRT like antenna. For MWA like antenna this is

$$SNR \propto x_{\text{HI}}(z)(1+z)^{n/2-\beta} \quad (5.17)$$

The normalized baseline distribution function $\rho_N(\vec{U}, \nu)$ is frequency dependent and the parameter n takes care of that. Note that $n = 0$ is the situation for uniform baseline coverage. The value of n depends on the bubble size. For large bubbles the signal remains confined within small baselines whereas for smaller bubbles a significant amount

5 Optimum Redshift for Detecting Ionized Bubbles

of signal spreads to larger baselines. Thus the normalized baseline distribution function $\rho_N(\vec{U}, \nu)$ acts in different manner on bubbles of different sizes. For a situation when the $\rho_N(\vec{U}, \nu)$ is constant in \vec{U} over the signal we have $n = 2$. In a situation where the signal is constant in \vec{U} over the whole baseline range $\rho_N(\vec{U}, \nu)$ does not play significant role and $n = 0$. In general we have $0 < n < 2$. We will discuss more about the exact values of n for the GMRT and the MWA later.

The GMRT baseline distribution is well described by the sum of a Gaussian (at small baselines) and an exponential (at large baseline)(Figure 3.5 in Chapter 3). Here $\rho_N(\vec{U}, \nu)$ remains almost constant up to a baseline $\vec{U} = 100$ for the frequency range of interest and then it decays. For the larger bubbles of radius $R_b \geq 50\text{Mpc}$, the signal is confined with a maximum baseline of $\vec{U} = 100$ and we have $n = 2$ for which $SNR \propto x_{\text{HI}}(z)(1+z)^{-3.6}$ where we assume $\beta = 2.6$. For smaller bubbles the signal extends to larger baselines where the baseline distribution function $\rho_N(\vec{U}, \nu)$ decays with \vec{U} and the n value also becomes smaller. For example, for the bubbles of sizes $R_b = 30, 20$ and 10Mpc the values of n are 1.27, 1.07 and 0.5 respectively. We have assumed that the MWA antenna distribution is $\rho_{ant} \sim r^{-2}$, where r is physical distance from the center of the array. Here $\rho_N(\vec{U}, \nu)$ also decays monotonically. For the bubble sizes $R_b = 50, 30, 20$ and 10Mpc the values of n are 0.45, 0.18 and 0 respectively.

The behavior of the HI fluctuations contribution also changes with redshift when we calculate for non-uniform and frequency dependent baseline distribution. As we go to higher redshifts the HI fluctuations decreases but slowly than uniform baseline case. This is due to the same reason as discussed in the 1st paragraph of this subsection. Using equation 5.8 we calculate $\langle(\Delta\hat{E})^2\rangle_{\text{HF}}$ numerically at different redshifts for the bubble sizes $R_b = 10, 20, 30$ and 50Mpc . For the GMRT we find that $\sqrt{\langle(\Delta\hat{E})^2\rangle_{\text{HF}}} \sim x_{\text{HI}}(z)(1+z)^{-3.67}, x_{\text{HI}}(z)(1+z)^{-3.37}, x_{\text{HI}}(z)(1+z)^{-3.25}$ and $x_{\text{HI}}(z)(1+z)^{-3.16}$ respectively. For the MWA these are $x_{\text{HI}}(z)(1+z)^{-4.26}, x_{\text{HI}}(z)(1+z)^{-4.18}, x_{\text{HI}}(z)(1+z)^{-4}$ and $x_{\text{HI}}(z)(1+z)^{-3.85}$

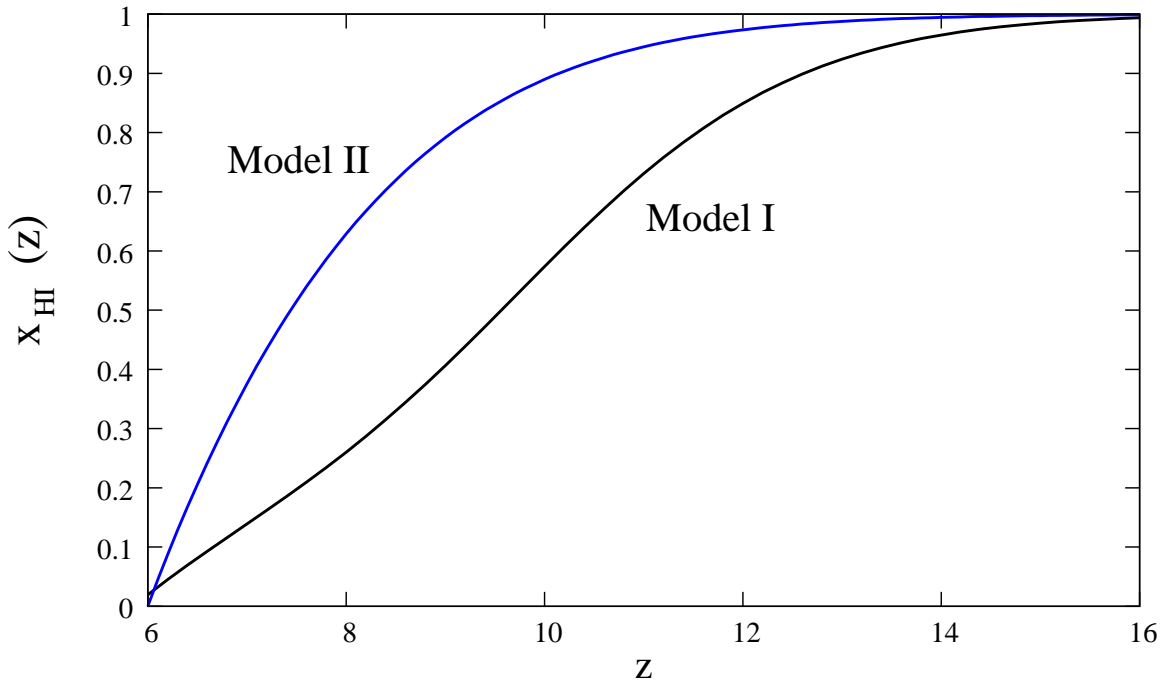


Figure 5.1: This shows the evolution of the mean neutral fraction x_{HI} with redshift for the two different reionization models discussed in the text.

respectively.

5.4.3 Evolution of neutral fraction with redshift

In this work, we consider two physically motivated models of reionization, namely, the early reionization model and the late reionization model which we call Model I and Model II respectively. These models are constructed using the semi-analytical formalism (Choudhury & Ferrara, 2005; Choudhury & Ferrara, 2006a) which implements most of the relevant physics governing the thermal and ionization history of the IGM, such as the inhomogeneous IGM density distribution, three different classes of ionizing photon sources (massive PopIII stars, PopII stars and QSOs), radiative feedback inhibiting star formation in low-mass galaxies and chemical feedback for transition from PopIII to PopII stars. The models are consistent with various observational data, namely, the redshift evolution of Lyman-limit absorption systems, the Gunn-Peterson effect, electron

5 Optimum Redshift for Detecting Ionized Bubbles

scattering optical depths, temperature of the IGM and cosmic star formation history.

In Model I, hydrogen reionization starts around $z \approx 16$ driven by metal-free (PopIII) stars, and it is 50% complete by $z \approx 10$. The contribution of PopIII stars decrease below this redshift because of the combined action of radiative and chemical feedback. As a result, reionization is extended considerably completing only at $z \approx 6$ (Figure 5.1).

In Model II, the contribution from the metal-free stars is ignored, which makes reionization start much later and is only 50 per cent complete only around $z \approx 7.5$. The main difference between this model with the previous one is in their predictions for the electron scattering optical depth (which is 0.15 for the early reionization model and 0.06 for the late reionization model). Recent measurements of the electron scattering optical depth $\tau_e = 0.087 \pm 0.017$ (Dunkley et al. 2008) suggests that these two models are possibly at two extreme ends of different possible reionization scenarios.

5.5 Optimum Redshift to Detect Ionized Bubbles

We consider bubbles of comoving size ranging from 2 Mpc to 50 Mpc at redshifts from $z = 6$ to 16. Figure 5.2 shows the SNR contours for 1000 hrs of observations with the GMRT. The left panel shows results for a constant neutral fraction $x_{\text{HI}} = 1$. This shows the joint effect of factors such as the background 21-cm brightness \bar{I}_ν , angular and frequency extent of the bubble, sky temperature, normalized baseline distribution function and the effective area of individual antenna. We see that the SNR is maximum at redshift the $z = 6$ for any bubble size. As we have discussed in Section 5.4 (equations 5.16 and 5.17) this is because of the lower noise at lower redshift. The region to the left of a line is allowed for the detection. For example a 5σ detection is possible for a bubble size $R_b > 16$ Mpc at redshift $z = 6$. At $z \geq 11$ a 5σ is not possible even for bubbles of size 50 Mpc. The middle shows the same results for Model I. We see that the redshift

5.5 Optimum Redshift to Detect Ionized Bubbles

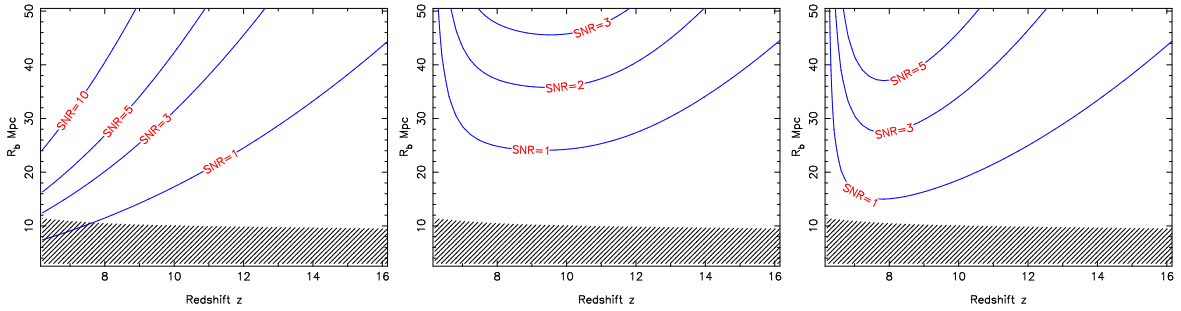


Figure 5.2: This shows the SNR contours for 1000 hrs observations with the GMRT. The left panel shows results for a constant neutral fraction $x_{\text{HI}} = 1$. Middle and right panel show results for the Model I and the Model II respectively. The HI fluctuations dominate over the signal in the shaded region and bubble detection is not possible.

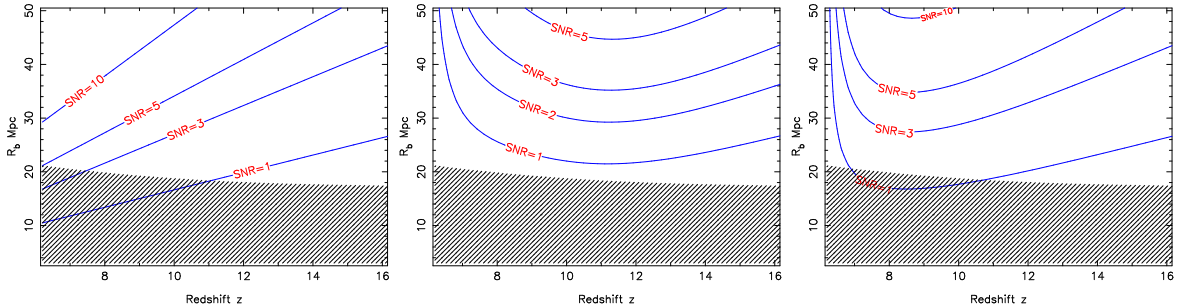


Figure 5.3: Same as the figure 5.2 for the MWA.

range $z \sim 9$ to 10 where the SNR is maximum is the optimum redshift range for bubble detection. We also see that a 3σ detection is possible for bubbles of size ≥ 46 Mpc at the optimum redshift. A 3σ detection is also possible for a bubble size $R_b \geq 50$ Mpc in the redshift range $z \sim 7$ to 11 . Results for the Model II are presented in the right panel. Here we see that redshift $z = 8$ is optimum for bubble detection. In this model the reionization occurred at lower redshift and hence the SNR is comparatively higher. Bubble detection is relatively easier in Model II. For example a 5σ detection is possible for $R_b \geq 38$ Mpc at $z = 8$ which is not possible in the Model I. In all the panels bubble detection is not possible on the shaded region due to the HI fluctuations.

Figure 5.3 shows the same results for the MWA. The effective collecting area of the individual MWA antenna is expected to increase with wavelength i.e, with redshift as

5 Optimum Redshift for Detecting Ionized Bubbles

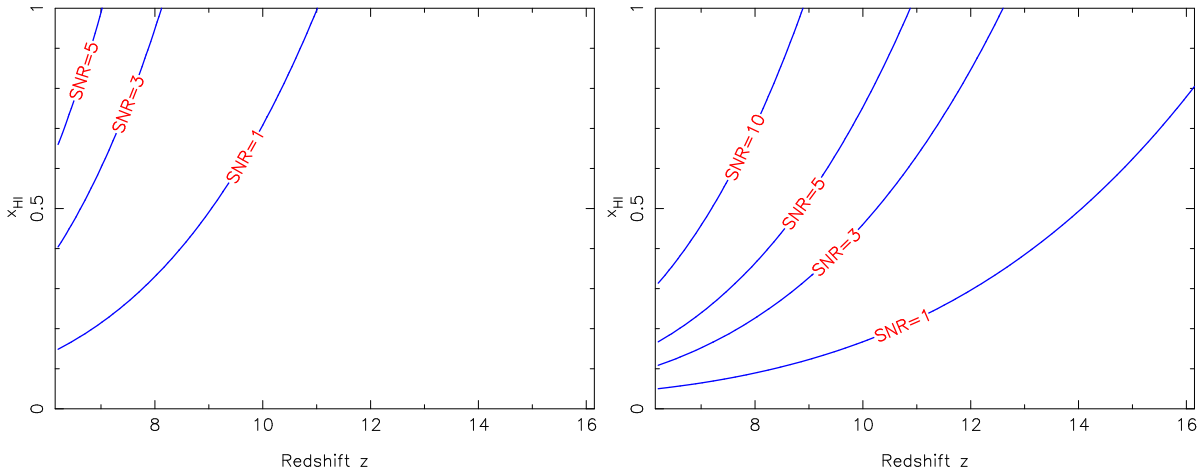


Figure 5.4: This shows the SNR contours for a fixed value of bubble size with the GMRT. Left panel shows results for a $R_b = 20$ Mpc bubble and 4000 hrs of observations. Right panel shows results for $R_b = 50$ Mpc bubble size and 1000 hrs of observations

$\sim (1+z)^2$. This will reduce the noise rms at higher redshifts and make bubble detection easier at higher redshifts than the GMRT. For example a 5σ detection is possible in Model I for bubble $R_b = 50$ Mpc in the redshift range $z = 9$ to 15 which seems impossible with the GMRT. The SNR is 3 times higher than the GMRT at redshift $z = 16$ for a $R_b = 46$ Mpc bubble. The optimum redshift in Model I for the MWA is $z \sim 11$ which is slightly higher than the GMRT. Detection of bubbles in model II is more optimistic in the MWA where 5σ is possible for bubbles of $R_b \geq 38$ Mpc at redshift $z \sim 8.5$ which is the optimum redshift of detection in this model.

In the above discussion we consider different models of the mean HI evolution. The HI evolution surrounding the ionized bubbles is highly unknown and model dependent. Keeping this in mind we consider a bubble of a fixed size and calculate the SNR for neutral fraction $x_{\text{HI}} = 0$ to 1 at various redshift ranging from $z = 6$ to 16 . We present results in Figures 5.4 and 5.5 for the GMRT and the MWA respectively for bubble size $R_b = 20$ Mpc (left panel) and 50 Mpc (right panel). The left panel in the figure 5.4 shows results for 4000 hrs of observation. The Figure demonstrates the detectability of

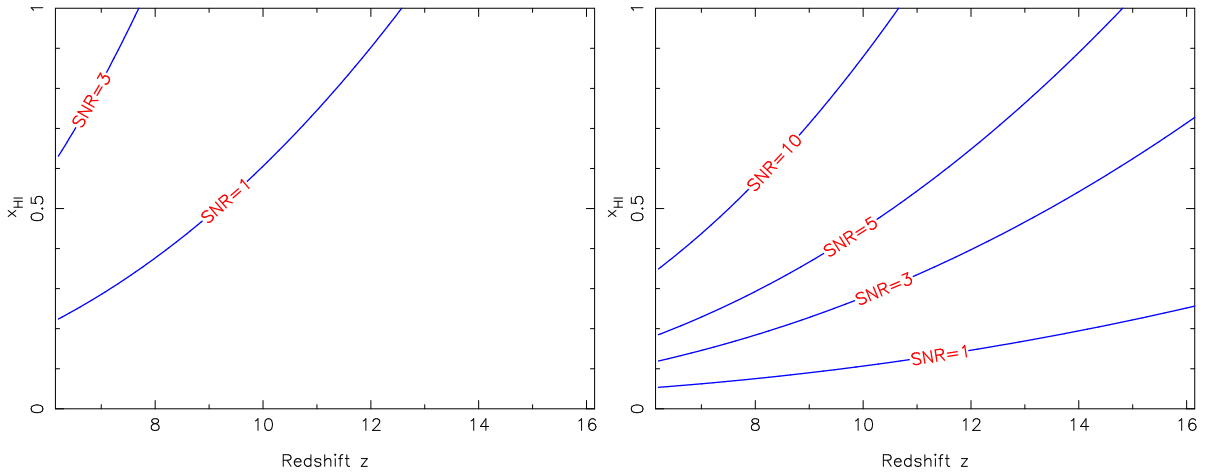


Figure 5.5: Same as the figure 5.4 for the MWA.

a $R_b = 20(50)$ Mpc bubble embedded in the HI of some neutral fraction. We see that a higher neutral fraction is required to detect bubbles at higher redshifts. For example we see that a 3σ detection for a bubble $R_b = 50$ Mpc is possible for neutral fraction ~ 0.1 at redshift $z = 6$ with the GMRT (Figure 5.4) but the neutral fraction ~ 1 is required at $z = 12$ to detect the same bubble. Bubble detection is found to be easier at higher redshifts for the MWA.

5.6 Conclusions

We investigate the optimum redshift for bubble detection. We find that for early reionization the redshift $z = 9$ and 11 are respectively the optimum redshifts for the GMRT and the MWA. For late reionization redshift $z = 8$ is found to be the optimum redshift for both the experiments. Bubble detection will be easier if the reionization occurred late. This is because of less noise and higher 21-cm background intensity. The MWA is suitable for bubble detection at higher redshifts ($z > 8.5$) than the GMRT. We also find that at redshift $z = 6$ if surrounding mean neutral fraction is $x_{\text{HI}} \geq 0.1$ a bubble of size $R_b > 50$ Mpc is possible to detect with 1000 hrs of observation for both the experiments.

5 *Optimum Redshift for Detecting Ionized Bubbles*

References

- Ali, S. S., Bharadwaj, S., & Pandey, B. , 2005, What will anisotropies in the clustering pattern in redshifted 21-cm maps tell us?, *Monthly Notices of Royal Astronomical Society*, 363, 251
- Ali, S. S., Bharadwaj, S., & Pandey, S. K. , 2006, Probing the bispectrum at high redshifts using 21-cm HI observations, *Monthly Notices of Royal Astronomical Society*, 366, 213
- Ali, S. S., Bharadwaj, S., & Chengalur, J. N. , 2008, Foregrounds for redshifted 21-cm studies of reionization: Giant Meter Wave Radio Telescope 153-MHz observations, *Monthly Notices of Royal Astronomical Society*, 385, 2166
- Alvarez, M. A., Shapiro, P. R., Ahn, K. & Iliev, I. T., 2006, Implications of WMAP 3 Year Data for the Sources of Reionization, *Astrophysical Journal Letters*, 644, L101
- Alvarez, M. A., & Abel, T. , 2007, Quasar HII regions during cosmic reionization, *Monthly Notices of Royal Astronomical Society: Letters*, 380, 54, L30
- Arons J., & Wingert D. W., 1972, Theoretical Models of Photoionized Intergalactic Hydrogen, *Astrophysical Journal*, 177, 1
- Ballinger, W. E., Peacock, J. A., Heavens, A. F., 1996, Measuring the cosmological constant with redshift surveys, *Monthly Notices of Royal Astronomical Society*, 282, 877
- Barkana R. & Loeb A., 2001, In the beginning: the first sources of light and the reionization of the universe, *Physics Report*, 349, 125
- Barkana, R., & Loeb, A. , 2005, A Method for Separating the Physics from the Astrophysics of High-Redshift 21 Centimeter Fluctuations, *Astrophysical Journal Letters*, 624, L65

References

- Barkana R., 2006, The First Stars in the Universe and Cosmic Reionization, *Science*, 313, 789, 931
- Becker, Robert H., Fan, Xiaohui, White, Richard L., Strauss, Michael A., Narayanan, Vijay K., Lupton, Robert H., Gunn, James E., Annis, James, Bahcall, Neta A., Brinkmann, J., Connolly, A. J., Csabai, Istvn, Czarapata, Paul C., Doi, Mamoru, Heckman, Timothy M., Hennessy, G. S., Ivezi, eljko, Knapp, G. R., Lamb, Don Q., McKay, Timothy A., Munn, Jeffrey A., Nash, Thomas, Nichol, Robert, Pier, Jeffrey R., Richards, Gordon T., Schneider, Donald P., Stoughton, Chris, Szalay, Alexander S., Thakar, Aniruddha R., York, D. G., 2001, Evidence for Reionization at $z \approx 6$: Detection of a Gunn-Peterson Trough in a $z=6.28$ Quasar, *Astronomical Journal*, 122, 2850
- Bharadwaj, S., Nath, B. B., & Sethi, S. K., 2001, Using HI to Probe Large Scale Structures at $z \approx 3$, *Journal of Astrophysics and Astronomy*, 22, 21
- Bharadwaj, S. & Sethi, S. K. , 2001, HI Fluctuations at Large Redshifts: I-Visibility correlation, *Journal of Astrophysics and Astronomy*, 22, 293
- Bharadwaj, S. & Pandey, S. K. , 2003, HI Fluctuations at Large Redshifts: II - the Signal Expected for the GMRT, *Journal of Astrophysics and Astronomy*, 24, 23
- Bharadwaj, S., & Srikant, P. S. , 2004, HI Fluctuations at Large Redshifts: III - Simulating the Signal Expected at GMRT, *Journal of Astrophysics and Astronomy*, 25, 67
- Bharadwaj, S., & Ali, S. S. , 2004, The cosmic microwave background radiation fluctuations from HI perturbations prior to reionization, *Monthly Notices of Royal Astronomical Society*, 352, 142
- Bharadwaj, S., & Ali, S. S. , 2005, On using visibility correlations to probe the HI distribution from the dark ages to the present epoch - I. Formalism and the expected signal, *Monthly Notices of Royal Astronomical Society*, 356, 1519
- Bharadwaj, S., & Pandey, S. K. , 2005, Probing non-Gaussian features in the HI distribution at the epoch of re-ionization, *Monthly Notices of Royal Astronomical Society*, 358, 968
- Bhatnagar S., 2001, Radio study of Galactic Supernova Remnants and the Interstellar Medium, PhD Thesis, submitted to Tata Institute of Fundamental Research
- Bolton, J. S., & Haehnelt, M. G., 2007, The observed ionization rate of the intergalactic medium and the ionizing emissivity at $z \geq 5$: evidence for a photon-starved and extended epoch of reionization, *Monthly Notices of Royal Astronomical Society*, 382, 325

- Bowman, J. D., Morales, M. F., & Hewitt, J. N. , 2006, The Sensitivity of First-Generation Epoch of Reionization Observatories and Their Potential for Differentiating Theoretical Power Spectra, *Astrophysical Journal*, 638, 20
- Bowman, Judd D., Barnes, David G., Briggs, Frank H., Corey, Brian E., Lynch, Merv J., Bhat, N. D. Ramesh, Cappallo, Roger J., Doeleman, Sheperd S., Fanous, Brian J., Herne, David, Hewitt, Jacqueline N., Johnston, Chris, Kasper, Justin C., Kocz, Jonathon, Kratzenberg, Eric, Lonsdale, Colin J., Morales, Miguel F., Oberoi, Divya, Salah, Joseph E., Stansby, Bruce, Stevens, Jamie, Torr, Glen, Wayth, Randall, Webster, Rachel L., Wyithe, J. Stuart B. Bowman, 2007, Field Deployment of Prototype Antenna Tiles for the Mileura Widefield Array Low Frequency Demonstrator, *Astronomical Journal*, 133,1505
- Bunn E.F., & White M., 1997, The 4 Year COBE Normalization and Large-Scale Structure, *Astrophysical Journal*, 480, 6
- Carilli, C. L. , 2006, HI 21 cm probes of reionization, and beyond, *New Astronomy Review*, 50, -3, 162
- Chen, X. & Miralda-Escude, J., 2004, The Spin-Kinetic Temperature Coupling and the Heating Rate due to Ly Scattering before Reionization: Predictions for 21 Centimeter Emission and Absorption, *Astrophysical Journal*, 602, 1
- Chengalur, J.N., Gupta, Y., & Dwarkanath, K.S., 2003, Low frequency Radio Astronomy, Pune-India, National Center for Radio Astronomy, 1st edition, 191
- Choudhury, T. R., & Ferrara, A., 2005, Experimental constraints on self-consistent reionization models, *Monthly Notices of Royal Astronomical Society*, 361, 577
- Choudhury T. R., Ferrara A., 2006, Physics of Cosmic Reionization, Cosmic Polarization, Editor - R. Fabbri, Trivandrum-India, Research Signpost, 205, astro-ph/0603149
- Choudhury T. R., Ferrara A. , 2006a, Updating reionization scenarios after recent data, *Monthly Notices of Royal Astronomical Society: Letters*, 371, L55
- Choudhury T. R., Ferrara A., 2007, Searching for the reionization sources, *Monthly Notices of Royal Astronomical Society: Letters*, 380, L6
- Choudhury, T. R., Ferrara, A., & Gallerani, S., 2008, On the minimum mass of reionization sources, *Monthly Notices of Royal Astronomical Society: Letters*, 385, L58
- Choudhury, T. R., Haehnelt, M. G., & Regan, J. , 2008, Inside-out or Outside-in: The topology of reionization in the photon-starved regime suggested by Lyman-alpha forest data, *Monthly Notices of Royal Astronomical Society*, in press, arXiv:0806.1524
- Ciardi, B. & Madau, P., 2003, Probing beyond the Epoch of Hydrogen Reionization with 21 Centimeter Radiation, *Astrophysical Journal*, 596, 1

References

- Cohn J. D., & Chang T. C., , 2007, Source mergers and bubble growth during reionization, *Monthly Notices of Royal Astronomical Society*, 374, 72
- Colombo, L. P. L., , 2004, Constraining the reionization history with large angle cosmic microwave background polarization, *Journal of Cosmology and Astroparticle Physics*, 003
- Cooray, A., & Furlanetto, S. R. , 2005, Polarization signals of the 21-cm background from the era of reionization, *Monthly Notices of Royal Astronomical Society: Letters*, 359, L47
- Cooray, A. , 2005, Large-scale non-Gaussianities in the 21-cm background anisotropies from the era of reionization, *Monthly Notices of Royal Astronomical Society*, 363, 1049
- Datta, K. K., Choudhury, T., R., & Bharadwaj, S. , 2007, The multifrequency angular power spectrum of the epoch of reionization 21-cm signal, *Monthly Notices of Royal Astronomical Society*, 378, 119
- Datta, K. K., Bharadwaj, S., & Choudhury, T., R., 2007, Detecting ionized bubbles in redshifted 21-cm maps, *Monthly Notices of Royal Astronomical Society*, 382, 809
- Datta, K. K., Majumdar, S., Bharadwaj, S., & Choudhury, T., R., , 2008, Simulating the impact of HI fluctuations on matched filter search for ionized bubbles in redshifted 21-cm maps, *Monthly Notices of Royal Astronomical Society*, 391, 1900
- Datta, K. K., Bharadwaj, S., & Choudhury, T., R., 2009, The optimal redshift for detecting ionized bubbles in HI 21-cm maps, [arxiv:0906.0360](https://arxiv.org/abs/0906.0360)
- Di Matteo, T., Perna R., Abel, T., Rees, M. J., , 2002, Radio Foregrounds for the 21 Centimeter Tomography of the Neutral Intergalactic Medium at High Redshifts, *Astrophysical Journal*, 564, 576
- Di Matteo, T., Ciardi, B., & Miniati, F. , 2004, The 21-cm emission from the reionization epoch: extended and point source foregrounds, *Monthly Notices of Royal Astronomical Society*, 355, 1053
- Dunkley, J., Komatsu, E., Nolte, M. R., Spergel, D. N., Larson, D., Hinshaw, G., Page, L., Bennett, C. L., Gold, B., Jarosik, N., Weiland, J. L., Halpern, M., Hill, R. S., Kogut, A., Limon, M., Meyer, S. S., Tucker, G. S., Wollack, E., Wright, E. L., 2008, Five-Year Wilkinson Microwave Anisotropy Probe, WMAP Observations: Likelihoods and Parameters from the WMAP data, *Astrophysical Journal Supplement Series*, in press, [arXiv:0803.0586](https://arxiv.org/abs/0803.0586)
- Ellingson S. W., 2005, Receivers for Low-Frequency Radio Astronomy, From Clark Lake to the Long Wavelength Array: Bill Erickson's Radio Science, Editors: Kassim, Namir E., Perez, Mario R., Junor, William, Henning, Patricia A, *Astronomical Society of Pacific Conference Series*, 345, 321

- Fan, Xiaohui, Narayanan, Vijay K., Strauss, Michael A., White, Richard L., Becker, Robert H., Pentericci, Laura, Rix, Hans-Walter, 2002, Evolution of the Ionizing Background and the Epoch of Reionization from the Spectra of $z \approx 6$ Quasars, *Astronomical Journal*, 123, 1247
- Fan, Xiaohui, Strauss, Michael A., Becker, Robert H., White, Richard L., Gunn, James E., Knapp, Gillian R., Richards, Gordon T., Schneider, Donald P., Brinkmann, J., Fukugita, Masataka, 2006, Constraining the Evolution of the Ionizing Background and the Epoch of Reionization with $z \approx 6$ Quasars. II. A Sample of 19 Quasars, *Astronomical Journal*, 132, 117
- Fan, X., Carilli, C. L., Keating, B., 2006, Observational Constraints on Cosmic Reionization, *Annual Review of Astronomy & Astrophysics*, 44, 415
- Fridman P. A., Baan, W. A., 2001, RFI mitigation methods in radio astronomy, *Astronomy & Astrophysics*, 378, 327
- Furlanetto, S. R., Sokasian, A., & Hernquist, L., 2004, Observing the reionization epoch through 21-centimetre radiation, *Monthly Notices of Royal Astronomical Society*, 347, 187
- Furlanetto, S. R., Zaldarriaga, M., & Hernquist, L., 2004a, The Growth of H II Regions During Reionization, *Astrophysical Journal*, 613, 1
- Furlanetto, S. R., Zaldarriaga, M., & Hernquist, L., 2004b, Statistical Probes of Reionization with 21 Centimeter Tomography, *Astrophysical Journal*, 613, 16
- Furlanetto, S. R., McQuinn, M., & Hernquist, L., 2006, Characteristic scales during reionization, *Monthly Notices of Royal Astronomical Society*, 365, 115
- Furlanetto, S. R., Oh, S. P., & Briggs, F. H., 2006, Cosmology at low frequencies: The 21 cm transition and the high-redshift Universe, *Physics Report*, 433, 181
- Furlanetto, S., Haiman, Z., & Oh, S. P., 2008, Fossil Ionized Bubbles around Dead Quasars during Reionization, *Astrophysical Journal*, 686, 25
- Gallerani, S., Ferrara, A., Fan, X., Roy, C. T., & Salvaterra, R., 2008, Was the Universe neutral beyond redshift six? Proceedings 'A Century of Cosmology', San Servolo, Venezia, Italy, to be published in *II Nuovo Cimento*, arXiv:0801.4674
- Geil, P. M., & Wyithe, J. S. B., 2008, The impact of a percolating IGM on redshifted 21-cm observations of quasar HII regions, *Monthly Notices of Royal Astronomical Society*, 386, 1683
- Geil, P. M., Wyithe, S., Petrovic, N., & Oh, P., 2008, The effect of Galactic foreground subtraction on redshifted 21-cm observations of quasar HII regions, *Monthly Notices of Royal Astronomical Society*, 390, 1496

References

- Gleser, L., Nusser, A., & Benson, A. J. , 2008, Decontamination of cosmological 21-cm maps, *Monthly Notices of Royal Astronomical Society*, 391, 383
- Gnedin, N. Y. & Ostriker, J. P, 1997, Reionization of the Universe and the Early Production of Metals, *Astrophysical Journal*, 486, 581-598
- Gnedin, N. Y., & Shaver, P. A. , 2004, Redshifted 21 Centimeter Emission from the Pre-Reionization Era. I. Mean Signal and Linear Fluctuations, *Astrophysical Journal*, 608, 611
- Gunn J. E. & Peterson B. A, 1965, On the Density of Neutral Hydrogen in Intergalactic Spacs, *Astrophysical Journal*, 142, 1633
- Haiman, Z. & Holder, G.P., 2003, The Reionization History at High Redshifts. I. Physical Models and New Constraints from Cosmic Microwave Background Polarization, *Astrophysical Journal*, 595, 1
- He, P., Liu, J., Feng, L.-L., Bi, H.-G., & Fang, L.-Z. , 2004, Statistical Features of 21 Centimeter Emission from the Epoch between Reionization and the Gunn-Peterson Transparency, *Astrophysical Journal*, 614, 6
- Hogan, C. J. & Rees, M. J., 1979, Spectral appearance of non-uniform gas at high Z, *Monthly Notices of Royal Astronomical Society*, 188, 791
- Higgins, J., & Meiksin, A. , 2009, The Wouthuysen-Field effect in a clumpy intergalactic medium, *Monthly Notices of Royal Astronomical Society*, 393, 949
- Hu, W., & Holder, G. P. , 2003, Model-independent reionization observables in the CMB, *Physical Review D*, 68, 023001
- Iliev, I.T., Shapiro, P.R., Farrara, A., Martel, H., 2002, On the Direct Detectability of the Cosmic Dark Ages: 21 Centimeter Emission from Minihalos, *Astrophysical Journal*, 572, L123
- Iliev, I.T., Scannapieco, E., Martel, H., Shapiro, P.R. , 2003, Non-linear clustering during the cosmic Dark Ages and its effect on the 21-cm background from minihaloes, *Monthly Notices of Royal Astronomical Society*, 341, 81
- Kaplinghat, M., Chu, M., Haiman, Z., Holder, G.P., Knox, L., & Skordis, C., 2003, Probing the Reionization History of the Universe using the Cosmic Microwave Background Polarization, *Astrophysical Journal Letters*, 583, 24
- Kohler, K., Gnedin, N. Y., Miralda-Escudé, J., & Shaver, P. A. , 2005, Redshifted 21 cm Emission from the Pre-Reionization Era. II. H II Regions around Individual Quasars, *Astrophysical Journal*, 633, 552

- Komatsu, E., Dunkley, J., Nolta, M. R., Bennett, C. L., Gold, B., Hinshaw, G., Jarosik, N., Larson, D., Limon, M., Page, L., Spergel, D. N., Halpern, M., Hill, R. S., Kogut, A., Meyer, S. S., Tucker, G. S., Weiland, J. L., Wollack, E., Wright, E. L. , 2008, Five-Year Wilkinson Microwave Anisotropy Probe, WMAP Observations: Cosmological Interpretation, *Astrophysical Journal Supplement Series*, in press, arXiv:0803.0547
- Kramer R. H., Haiman Z., & Oh S. P., 2006, Feedback from Clustered Sources during Reionization, *Astrophysical Journal*, 649, 570
- Leshem, A., van der Veen, A. J., & Boonstra, A. J., 2000, Multichannel Interference Mitigation Techniques in Radio Astronomy, *Astrophysical Journal Supplement Series*, 131, 355
- Loeb, A., & Zaldarriaga, M. , 2004, Measuring the Small-Scale Power Spectrum of Cosmic Density Fluctuations through 21cm Tomography Prior to the Epoch of Structure Formation, *Physical Review Letters*, 92, 211301
- Madau P., Meiksin A. & Rees, M. J., 1997, 21 Centimeter Tomography of the Inter-galactic Medium at High Redshift, *Astrophysical Journal*, 475, 429
- Maselli, A., Gallerani, S., Ferrara, A. & Choudhury, T. R., 2007, On the size of HII regions around high-redshift quasars, *Monthly Notices of Royal Astronomical Society: Letters*, 376, L34
- McQuinn, M., Zahn, O., Zaldarriaga, M., Hernquist, L., Furlanetto, S.R., 2006, Cosmological Parameter Estimation Using 21 cm Radiation from the Epoch of Reionization, *Astrophysical Journal*, 653, 815
- Mesinger, A., & Haiman, Z., 2004, Evidence of a Cosmological Strmgren Surface and of Significant Neutral Hydrogen Surrounding the Quasar SDSS J1030+0524, *Astrophysical Journal Letters*, 611, L69
- Mesinger, A., & Furlanetto, S. , 2007, Efficient Simulations of Early Structure Formation and Reionization, *Astrophysical Journal*, 669, 663-675
- Miralda-Escude, J., 2003, The Dark Age of the Universe, *Science* 300, 300, 627, 1904
- Morales M. F.,& Hewitt J. N., 2004, Toward Epoch of Reionization Measurements with Wide-Field Radio Observations, *Astrophysical Journal*, 615, 7
- Morales M. F., Bowman J. D., & Hewitt J. N., 2006, Improving Foreground Subtraction in Statistical Observations of 21 cm Emission from the Epoch of Reionization, *Astrophysical Journal*, 648, 767
- Oh, S.P., & Mack,K.J., 2003, Foregrounds for 21-cm observations of neutral gas at high redshift, *Monthly Notices of Royal Astronomical Society*, 346, 871

References

- Page, L., Hinshaw, G., Komatsu, E., Nolta, M. R., Spergel, D. N., Bennett, C. L., Barnes, C., Bean, R., Dor, O., Dunkley, J., Halpern, M., Hill, R. S., Jarosik, N., Kogut, A., Limon, M., Meyer, S. S., Odegard, N., Peiris, H. V., Tucker, G. S., Verde, L., Weiland, J. L., Wollack, E., Wright, E. L., 2007, Three-Year Wilkinson Microwave Anisotropy Probe, WMAP Observations: Polarization Analysis, *Astrophysical Journal Supplement Series*, 170, 335
- Peacock J.A., 1999, *Cosmological Physics*, Cambridge, Cambridge University Press, First Edition, p. 517
- Salvaterra, R., Ciardi, B., Ferrara, A., & Baccigalupi, C., 2005, Reionization history from coupled cosmic microwave background/21-cm line data, *Monthly Notices of Royal Astronomical Society*, 360, 1063
- Santos, M. G., Cooray, A., & Knox, L. , 2005, Multifrequency Analysis of 21 Centimeter Fluctuations from the Era of Reionization, *Astrophysical Journal*, 625, 575
- Scott D. & Rees, M. J., 1990, The 21-cm line at high redshift: a diagnostic for the origin of large scale structure, *Monthly Notices of Royal Astronomical Society*, 247, 510-516
- Sethi, S. K., , 2005, HI signal from re-ionization epoch, *Monthly Notices of Royal Astronomical Society*, 363, 818
- Shapiro P. R., & Giroux M. L., 1987, Cosmological H II regions and the photoionization of the intergalactic medium, *Astrophysical Journal Letters*, 321, L107
- Shaver, P. A., Windhorst, R. A., Madau, P. & de Bruyn, A. G., 1999, Can the reionization epoch be detected as a global signature in the cosmic background?, *Astronomy & Astrophysics*, 345, 380
- Sheth, R., 1996, The distribution of pairwise peculiar velocities in the non-linear regime, *Monthly Notices of Royal Astronomical Society*, 279, 1310
- Spergel, D. N., Bean, R., Dore, O., Nolta, M. R., Bennett, C. L., Dunkley, J., Hinshaw, G., Jarosik, N., Komatsu, E., Page, L., Peiris, H. V., Verde, L., Halpern, M., Hill, R. S., Kogut, A., Limon, M., Meyer, S. S., Odegard, N., Tucker, G. S., Weiland, J. L., Wollack, E., Wright, E. L., 2007, Three-Year Wilkinson Microwave Anisotropy Probe, WMAP Observations: Implications for Cosmology, *Astrophysical Journal Supplement Series*, 170, 377
- Sunyaev, R. A. & Zeldovich, Ya. B., 1972, Formation of Clusters of Galaxies; Proto-cluster Fragmentation and Intergalactic Gas Heating, *Astronomy & Astrophysics*, 22, 189
- Swarup G., Ananthakrishnan S., Kapahi V.K., Rao A.P., Subramanya C.R., Kulkarni V.K., 1991, The Giant Metre-Wave Radio Telescope, *Current Science*, 60, 95

- Thompson A. R., Moran J. M. & Swenson G. W., Jr., 1986, *Interferometry and Synthesis in Radio Astronomy*, New York, John Wiley and Sons, First Edition, pp 405
- Tozzi, P., Madau, P., Meiksin, A., Rees, M. J., 2000, Radio Signatures of H I at High Redshift: Mapping the End of the “Dark Ages”, *Astrophysical Journal*, 528, 597
- Wang, X. & Hu, W., 2006, Redshift Space 21 cm Power Spectra from Reionization, *Astrophysical Journal*, 643, 585
- Wang, X., Tegmark, M., Santos, M. G., & Knox, L. , 2006, 21 cm Tomography with Foregrounds, *Astrophysical Journal*, 650, 529
- White, R. L., Becker, R. H., Fan, X., & Strauss, M. A. , 2003, Probing the Ionization State of the Universe at $z \gtrsim 6$, *Astronomical Journal*, 126, 1
- Wyithe, J. S. B., Loeb, A., 2004, A characteristic size of ~ 10 Mpc for the ionized bubbles at the end of cosmic reionization, *Nature*, 432, 014, 194
- Wyithe, J. S. B., & Loeb, A. , 2004a, Redshifted 21 Centimeter Signatures around the Highest Redshift Quasars, *Astrophysical Journal*, 610, 117
- Wyithe, J. S. B., Loeb, A., & Barnes, D. G. , 2005, Prospects for Redshifted 21 cm Observations of Quasar H II Regions, *Astrophysical Journal*, 634, 715
- Wyithe, J. S. B. , 2008, Redshifted 21-cm observations of high-redshift quasar proximity zones, *Monthly Notices of Royal Astronomical Society*, 387, 469
- Yu, Q. , 2005, The Apparent Shape of the Stromgren Sphere around the Highest Redshift QSOs with Gunn-Peterson Troughs, *Astrophysical Journal*, 623, 683
- Zahn, O., Lidz, A., McQuinn, M., Dutta, S., Hernquist, L., Zaldarriaga, M., & Furlanetto, S. R. , 2007, Simulations and Analytic Calculations of Bubble Growth during Hydrogen Reionization, *Astrophysical Journal*, 654, 12
- Zaldarriaga, M., Furlanetto, S. R., & Hernquist, L. , 2004, 21 Centimeter Fluctuations from Cosmic Gas at High Redshifts, *Astrophysical Journal*, 608, 622

Appendix

A Calculation of the angular power spectrum $C_l(\nu_1, \nu_2)$

In this section, we present the details of the calculation for the 21 cm angular power spectrum $C_l(\nu_1, \nu_2)$. The first step would be to calculate the spherical harmonic component a_{lm} of the brightness temperature $T(\nu, \hat{\mathbf{n}})$. Using the expression (2.6) for $\tilde{\eta}_{\text{HI}}(\mathbf{k})$ in equation (2.10), the expression for a_{lm} can be written as

$$a_{lm}(\nu) = \bar{T} \bar{x}_{\text{HI}} \int d\Omega Y_{lm}^*(\hat{\mathbf{n}}) \int \frac{d^3k}{(2\pi)^3} \times \left[\Delta_{\text{HI}}(\mathbf{k}) + (\hat{\mathbf{n}} \cdot \hat{\mathbf{k}})^2 \Delta(\mathbf{k}) \right] e^{-ikr_\nu(\hat{\mathbf{k}} \cdot \hat{\mathbf{n}})} \quad (\text{A1})$$

which then essentially involves solving angular integrals of the forms $\int d\Omega Y_{lm}^* e^{-ikr_\nu(\hat{\mathbf{k}} \cdot \hat{\mathbf{n}})}$ and $\int d\Omega Y_{lm}^* (\hat{\mathbf{n}} \cdot \hat{\mathbf{k}})^2 e^{-ikr_\nu(\hat{\mathbf{k}} \cdot \hat{\mathbf{n}})}$ respectively. Expanding the term $e^{-ikr_\nu(\hat{\mathbf{k}} \cdot \hat{\mathbf{n}})}$ in terms of spherical Bessel functions $j_l(kr_\nu)$, one can show that

$$\int d\Omega Y_{lm}^*(\hat{\mathbf{n}}) e^{-ikr_\nu(\hat{\mathbf{k}} \cdot \hat{\mathbf{n}})} = 4\pi (-i)^l j_l(kr_\nu) Y_{lm}^*(\hat{\mathbf{k}}) \quad (\text{A2})$$

Differentiating the above equation with respect to kr_ν twice

$$\int d\Omega (\hat{\mathbf{k}} \cdot \hat{\mathbf{n}})^2 Y_{lm}^*(\hat{\mathbf{n}}) e^{-ikr_\nu(\hat{\mathbf{k}} \cdot \hat{\mathbf{n}})} = -4\pi (-i)^l j_l''(kr_\nu) Y_{lm}^*(\hat{\mathbf{k}}) \quad (\text{A3})$$

where $j_l''(x)$ is the second derivative of $j_l(x)$ with respect to its argument, and can be obtained through the recursion relation

$$(2l+1)j_l''(x) = \frac{l(l-1)}{2l-1} j_{l-2}(x) - \left[\frac{l^2}{2l-1} + \frac{(l+1)^2}{2l+3} \right] j_l(x)$$

5 Appendix

$$+\frac{(l+1)(l+2)}{2l+3}j_{l+2}(x) \quad (\text{A4})$$

So the final expression of a_{lm} is given by

$$\begin{aligned} a_{lm}(\nu) &= 4\pi\bar{T}\bar{x}_{\text{HI}}(-i)^l \int \frac{d^3k}{(2\pi)^3} Y_{lm}^*(\hat{\mathbf{k}}) \\ &\times [\Delta_{\text{HI}}(\mathbf{k})j_l(kr_\nu) - \Delta(\mathbf{k})j_l''(kr_\nu)] \end{aligned} \quad (\text{A5})$$

The next step is to calculate the the power spectrum $C_l(\nu_1, \nu_2) \equiv \langle a_{lm}(\nu_1) a_{lm}^*(\nu_2) \rangle$.

The corresponding expression is then given by

$$\begin{aligned} C_l(\nu_1, \nu_2) &= (4\pi)^2 \bar{T}(z_1) \bar{T}(z_2) \bar{x}_{\text{HI}}(z_1) \bar{x}_{\text{HI}}(z_2) \\ &\times \int \frac{d^3k_1}{(2\pi)^3} \int \frac{d^3k_2}{(2\pi)^3} Y_{lm}^*(\hat{\mathbf{k}}_1) Y_{lm}(\hat{\mathbf{k}}_2) \\ &\times \langle [\Delta_{\text{HI}}(z_1, \mathbf{k}_1) j_l(k_1 r_{\nu_1}) - \Delta(z_1, \mathbf{k}_1) j_l''(k_1 r_{\nu_1})] \\ &\times [\Delta_{\text{HI}}^*(z_2, \mathbf{k}_2) j_l(k_2 r_{\nu_2}) - \Delta^*(z_2, \mathbf{k}_2) j_l''(k_2 r_{\nu_2})] \rangle \end{aligned} \quad (\text{A6})$$

where we have put back the redshift-dependence into the expressions for clarity. Now note that we would mostly be interested in cases where $\nu_2 - \nu_1 \equiv \Delta\nu \ll \nu_1$. In such cases, one can safely assume $\bar{T}(z_2) \approx \bar{T}(z_1)$ and $\bar{x}_{\text{HI}}(z_2) \approx \bar{x}_{\text{HI}}(z_1)$. Furthermore, the terms involving the ensemble averages of the form $\langle \Delta\Delta^* \rangle$ can be approximated as $\langle \Delta(z_1, \mathbf{k}_1) \Delta^*(z_2, \mathbf{k}_2) \rangle \approx (2\pi)^3 \delta_D(\mathbf{k}_1 - \mathbf{k}_2) P(z_1, k_1)$ and similarly for terms involving Δ_{HI} . We can then use the Dirac delta function $\delta_D(\mathbf{k}_1 - \mathbf{k}_2)$ to compute the \mathbf{k}_2 -integral, and thus can write the angular power spectrum as

$$C_l(\Delta\nu) \equiv C_l(\nu, \nu + \Delta\nu)$$

$$\begin{aligned}
&= (4\pi)^2 \bar{T}^2 \bar{x}_{\text{HI}}^2 \int \frac{d^3 k_1}{(2\pi)^3} Y_{lm}^*(\hat{\mathbf{k}}) Y_{lm}(\hat{\mathbf{k}}) \\
&\times \left[j_l(kr_\nu) j_l(kr_{\nu_2}) P_{\Delta_{\text{HI}}}^2(k) \right. \\
&\quad - \{ j_l(kr_\nu) j_l''(kr_{\nu_2}) + j_l(kr_{\nu_2}) j_l''(kr_\nu) \} P_{\Delta_{\text{HI}}}(k) \\
&\quad \left. + j_l''(kr_\nu) j_l''(kr_{\nu_2}) P(k) \right] \tag{A7}
\end{aligned}$$

Using the normalization property of the spherical harmonics $\int d\hat{\mathbf{n}} |Y_{lm}(\hat{\mathbf{n}})|^2 = 1$, one can carry out the angular integrals in the above expression, and hence obtain the final result (2.11) as quoted in the main text.

B Correspondence between all-sky and flat-sky power spectra

As discussed in section 2.2.3, we shall mostly be interested in very small angular scales, which corresponds to $l \gg 1$. For high values of l , it is most useful to work in the flat-sky approximation, where a small portion of the sky can be approximated by a plane. Then the unit vector $\hat{\mathbf{n}}$ towards the direction of observation can be decomposed into $\hat{\mathbf{n}} = \mathbf{m} + \theta$, where \mathbf{m} is a vector towards the center of the field of view and θ is a two-dimensional vector in the plane of the sky.

Without loss of generality, let us now consider a small region around the pole $\theta \rightarrow 0$. In that case the vector θ can be treated as a Cartesian vector with components $\{\theta \cos \phi, \theta \sin \phi\}$. This holds true for any two-dimensional vector on the sky, in particular $\mathbf{U} = \{U \cos \phi_U, U \sin \phi_U\}$. Then the spherical harmonic components of $T(\nu, \hat{\mathbf{n}})$ [defined in equation (2.10)] can be written as

$$a_{lm}(\nu) \approx \int d\theta Y_{lm}^*(\theta, \phi) T(\nu, \hat{\mathbf{n}}) \tag{B1}$$

5 Appendix

where we have replaced $\int d\Omega \rightarrow \int d\theta$. Now use the expansion

$$e^{-2\pi i \mathbf{U} \cdot \theta} = \sum_m (-i)^m J_m(2\pi U \theta) e^{im(\phi_U - \phi)} \quad (\text{B2})$$

where $J_m(x)$ is the ordinary Bessel function. Further, we use the approximation for spherical harmonics

$$Y_{lm}(\theta, \phi) \underset{\theta \rightarrow 0}{\approx} J_m(l\theta) \sqrt{\frac{l}{2\pi}} e^{im\phi} \quad (\text{B3})$$

to write

$$e^{-2\pi i \mathbf{U} \cdot \theta} \approx \sqrt{\frac{1}{U}} \sum_m (-i)^m Y_{2\pi U, m}^*(\theta, \phi) e^{-im\phi_U} \quad (\text{B4})$$

Then the two-dimensional Fourier transform of the brightness temperature [defined in equation (2.16)] will be

$$\begin{aligned} \tilde{T}(\nu, \mathbf{U}) &= \int d\theta e^{-2\pi i \mathbf{U} \cdot \theta} T(\nu, \hat{\mathbf{n}}) \\ &\approx \sqrt{\frac{1}{U}} \sum_m (-i)^m e^{-im\phi_U} \int d\theta Y_{2\pi U, m}^*(\theta, \phi) T(\nu, \hat{\mathbf{n}}) \\ &= \sqrt{\frac{1}{U}} \sum_m (-i)^m e^{-im\phi_U} a_{2\pi U, m}(\nu) \end{aligned} \quad (\text{B5})$$

where we have used the expression (B1) for a_{lm} in the last part. This gives a relation between the flat-sky Fourier transform $\tilde{T}(\nu, \mathbf{U})$ and its the full-sky equivalent $a_{lm}(\nu)$.

Using the above relation, we can calculate the power spectrum

$$\begin{aligned} \langle \tilde{T}(\nu_1, \mathbf{U}) \tilde{T}^*(\nu_2, \mathbf{U}') \rangle &\approx \sqrt{\frac{1}{UU'}} \sum_{mm'} (-i)^{m-m'} e^{-im\phi_U} e^{im'\phi_{U'}} \\ &\quad \times \langle a_{2\pi U, m}(\nu_1) a_{2\pi U', m'}^*(\nu_2) \rangle \end{aligned} \quad (\text{B6})$$

Use the definition $\langle a_{lm}(\nu_1) a_{l'm'}^*(\nu_2) \rangle = C_l \delta_{ll'} \delta_{mm'}$ and the property

$$\sum_m e^{-im(\phi_U - \phi_{U'})} = 2\pi \delta_D^{(1)}(\phi_U - \phi_{U'}) \quad (\text{B7})$$

to obtain

$$\langle \tilde{T}(\nu_1, \mathbf{U}) \tilde{T}^*(\nu_2, \mathbf{U}') \rangle = 2\pi C_{2\pi U}(\nu_1, \nu_2) \frac{\delta_{UU'}}{U} \delta_D^{(1)}(\phi_U - \phi_{U'}) \quad (\text{B8})$$

The last step involves writing the right hand side of the above equation in terms of the two-dimensional Dirac delta function, which follows from the expansion

$$\delta_D^{(2)}(\mathbf{U} - \mathbf{U}') = \int d\theta e^{-2\pi i(\mathbf{U} - \mathbf{U}') \cdot \theta} \quad (\text{B9})$$

The exponentials can be written in terms of the spherical harmonics using equation (B4):

$$\begin{aligned} \delta_D^{(2)}(\mathbf{U} - \mathbf{U}') \approx & \int d\theta \sqrt{\frac{1}{UU'}} \sum_{mm'} (-i)^{m-m'} \\ & \times Y_{2\pi U, m}^*(\theta, \phi) Y_{2\pi U', m'}(\theta, \phi) e^{-im\phi_U} e^{im'\phi_{U'}} \end{aligned} \quad (\text{B10})$$

Finally use the orthonormality property of spherical harmonics $\int d\theta Y_{lm}^*(\theta, \phi) Y_{l'm'}(\theta, \phi) = \delta_{ll'} \delta_{mm'}$ and the relation (B7) to obtain

$$\delta_D^{(2)}(\mathbf{U} - \mathbf{U}') = 2\pi \frac{\delta_{UU'}}{U} \delta_D(\phi_U - \phi_{U'}) \quad (\text{B11})$$

Putting the above relation into (B8), we obtain equation (2.20) used in the final text.

C Relation between visibility-visibility correlation and MAPS

In this appendix we give the calculations for expressing the two visibility correlation in terms of the Multi-frequency angular power spectrum (MAPS). We can write the visibility $V(\vec{U}, \nu)$ as a two-dimensional Fourier transform of the brightness temperature $T(\vec{\theta}, \nu)$ [see equation (3.1)]

$$V(\vec{U}, \nu) = \left(\frac{\partial B}{\partial T} \right)_{\nu} \int d^2\theta A(\vec{\theta}, \nu) T(\vec{\theta}, \nu) e^{2\pi i \vec{\theta} \cdot \vec{U}} \quad (\text{C1})$$

where $(\partial B/\partial T)_{\nu}$ is the conversion factor from temperature to specific intensity and $A(\vec{\theta}, \nu)$ is the beam pattern of the individual antenna. The visibility-visibility correlation is then given by

$$\begin{aligned} \langle V(\vec{U}_1, \nu_1) V(\vec{U}_2, \nu_2) \rangle &= \left(\frac{\partial B}{\partial T} \right)_{\nu_1} \left(\frac{\partial B}{\partial T} \right)_{\nu_2} \\ &\times \int d^2\theta \int d^2\theta' A(\vec{\theta}, \nu_1) A(\vec{\theta}', \nu_2) \\ &\times \langle T(\vec{\theta}, \nu_1) T(\vec{\theta}', \nu_2) \rangle e^{2\pi i (\vec{\theta} \cdot \vec{U}_1 + \vec{\theta}' \cdot \vec{U}_2)} \end{aligned} \quad (\text{C2})$$

The correlation function for the temperature fluctuations on the sky would simply be the two-dimensional Fourier transform of the MAPS $C_{2\pi U}(\nu_1, \nu_2)$

$$\langle T(\vec{\theta}, \nu_1) T(\vec{\theta}', \nu_2) \rangle = \int d^2U C_{2\pi U}(\nu_1, \nu_2) e^{-2\pi i (\vec{\theta} - \vec{\theta}') \cdot \vec{U}} \quad (\text{C3})$$

Using the above equation in equation in (C2), we obtain

$$\begin{aligned} \langle V(\vec{U}_1, \nu_1) V(\vec{U}_2, \nu_2) \rangle &= \left(\frac{\partial B}{\partial T} \right)_{\nu_1} \left(\frac{\partial B}{\partial T} \right)_{\nu_2} \\ &\times \int d^2 U C_{2\pi U}(\nu_1, \nu_2) \\ &\times \tilde{A}(\vec{U}_1 - \vec{U}, \nu_1) \tilde{A}(\vec{U}_2 + \vec{U}, \nu_2) \end{aligned} \quad (C4)$$

where $\tilde{A}(\vec{U}, \nu)$ is the Fourier transform of the beam pattern $A(\vec{\theta}, \nu)$. If the beam pattern is assumed to be Gaussian $A(\vec{\theta}, \nu) = e^{-\theta^2/\theta_0^2}$, the Fourier transform too is given by a Gaussian function

$$\tilde{A}(\vec{U}, \nu) = \pi \theta_0^2 e^{-\pi^2 U^2 \theta_0^2} \quad (C5)$$

Hence, the visibility correlation becomes

$$\begin{aligned} \langle V(\vec{U}_1, \nu_1) V(\vec{U}_2, \nu_2) \rangle &= \left(\frac{\partial B}{\partial T} \right)_{\nu_1} \left(\frac{\partial B}{\partial T} \right)_{\nu_2} \pi^2 \theta_1^2 \theta_2^2 \\ &\times \int d^2 U C_{2\pi U}(\nu_1, \nu_2) \\ &\times e^{-\pi^2 [(\vec{U}_1 - \vec{U})^2 \theta_1^2 + (\vec{U}_2 + \vec{U})^2 \theta_2^2]} \end{aligned} \quad (C6)$$

where θ_1 and θ_2 are the values of θ_0 at ν_1 and ν_2 respectively. Now, since the two Gaussian functions in the above equation is peaked around different values of \vec{U} , the integrand will have a non-zero contribution only when $|\vec{U}_1 + \vec{U}_2| < (\pi \max[\theta_1, \theta_2])^{-1}$. In case the typical baselines are much larger than the quantity $(\pi \max[\theta_1, \theta_2])^{-1}$, the integral above can be well approximated as being non-zero only when $\vec{U}_1 = -\vec{U}_2$. Then

$$\begin{aligned} \langle V(\vec{U}_1, \nu_1) V(\vec{U}_2, \nu_2) \rangle &\approx \delta_{\vec{U}_1, -\vec{U}_2} \left(\frac{\partial B}{\partial T} \right)_{\nu_1} \left(\frac{\partial B}{\partial T} \right)_{\nu_2} \\ &\times \pi^2 \theta_1^2 \theta_2^2 C_{2\pi U_1}(\nu_1, \nu_2) \\ &\times \int d^2 U e^{-\pi^2 [(\vec{U}_1 - \vec{U})^2 (\theta_1^2 + \theta_2^2)]} \end{aligned}$$

5 Appendix

$$\begin{aligned}
&= \delta_{\vec{U}_1, -\vec{U}_2} \pi \left(\frac{\theta_1^2 \theta_2^2}{\theta_1^2 + \theta_2^2} \right) \left(\frac{\partial B}{\partial T} \right)_{\nu_1} \left(\frac{\partial B}{\partial T} \right)_{\nu_2} \\
&\times C_{2\pi U_1}(\nu_1, \nu_2)
\end{aligned} \tag{C7}$$

which is what has been used in equation (3.9).

In the continuum limit, the Gaussian $\tilde{A}(\vec{U}, \nu)$ can be approximated by a delta function, i.e., $\tilde{A}(\vec{U}, \nu) \approx \delta_D^{(2)}(\vec{U})$ (which corresponds to the limit $\theta_0 \rightarrow \infty$); the visibility-visibility correlation is then given as

$$\begin{aligned}
\langle V(\vec{U}_1, \nu_1) V(\vec{U}_2, \nu_2) \rangle &= \delta_D^{(2)}(\vec{U}_1 + \vec{U}_2) \left(\frac{\partial B}{\partial T} \right)_{\nu_1} \left(\frac{\partial B}{\partial T} \right)_{\nu_2} \\
&\times C_{2\pi U_1}(\nu_1, \nu_2)
\end{aligned} \tag{C8}$$

which corresponds to equation (3.21) in the main text.

List of Publications

(a) **Research Papers in Refereed Journals:**

- (i) Datta, K. K., Majumdar, S., Bharadwaj, S., & Choudhury, T., R., (2008), Simulating the impact of HI fluctuations on matched filter search for ionized bubbles in redshifted 21-cm maps, Monthly Notices of Royal Astronomical Society, Vol. 391, Issue 4, pp. 1900-1912
- (ii) Datta, K. K., Bharadwaj, S., & Choudhury, T., R. (2007), Detecting ionized bubbles in redshifted 21-cm maps, Monthly Notices of Royal Astronomical Society, Vol. 382, Issue 2, pp. 809-818
- (iii) Datta, K. K., Choudhury, T., R., & Bharadwaj, S. (2007), The multifrequency angular power spectrum of the epoch of reionization 21-cm signal, Monthly Notices of Royal Astronomical Society, Vol. 378, Issue 1, pp. 119-128

(b) **Submitted manuscripts:**

- (i) Guha Sarkar, T., Datta, K. K., & Bharadwaj, S. (2008), The CMBR ISW and HI 21-cm Cross-correlation Angular Power Spectrum, arXiv:0810.3649
- (ii) Datta, K. K., Bharadwaj, S., & Choudhury, T., R., The optimum redshift for detecting ionized bubbles in hi 21-cm maps, arxiv:0906.0360

(c) **Research Paper in Conference Proceedings:**

- (i) Datta K. K. (2006), Frequency decorrelation properties of the epoch of reionization 21 cm signal, Proceedings of XVII DAE- BRNS High Energy Physics Symposium, December 11- 15, 2006, IIT Kharagpur, pp. 217-220

5 Publications

- (ii) Datta, K. K., Majumdar, S., Bharadwaj, S., & Choudhury, T., R., (2009), Searching for Ionized bubbles in 21-cm maps, To appear in ASP Conference Series, Vol. 407, The Low-Frequency Radio Universe, eds D. J. Saikia, D. A. Green, Y. Gupta and T. Venturi (Conference held at NCRA, Pune, India from 8th to 12th December 2008)